Detection of in-plane stress waves with Polyvinylidene Fluoride (PVDF) sensors

A Thesis

Presented in Partial Fulfillment of the Requirements for the Degree Master of Science in the Graduate School of The Ohio State University

By

Kunal Kotian, B.E.

Graduate Program in Mechanical Engineering

The Ohio State University

2013

Master's Examination Committee:

Dr. Marcelo Dapino, Advisor

Dr. Daniel Mendelsohn

Abstract

Polyvinylidene Fluoride (PVDF), a piezoelectric polymer, is an excellent stress sensor. The objective of this research is to investigate the application of the PVDF sensors for detection of in-plane stress waves in 31 and 32 modes. This was achieved by focusing on aspects of PVDF sensing related to determination of impact force, detection of stress wave propagation, and the stress averaging effect of PVDF sensors.

An experimental method was developed for calculating a proportionality constant between a PVDF sensor's voltage and the impact force, on a solid bar and a hollow beam. This was used to demonstrate that impact force on a structure can be determined using PVDF sensors. Finite element models were also created using the software LS-DYNA to simulate the impact tests. The speed of sound for longitudinal wave propagation in a slender rod was determined experimentally, using two PVDF sensors. The results demonstrate that PVDF sensors can detect high speed stress wave propagation in a structure. Finally, the stress averaging effect of the PVDF sensor was analyzed to investigate its influence on the generated voltage during stress wave detection. Equations modeling the stress averaging effect were derived for periodic applied stress waves and impact-induced stress waves. Numerical simulations were conducted to study the influence of sensor length, applied wave frequency, and structure's material on the stress averaged PVDF response.

This thesis is dedicated to Aai and Pappa.

Acknowledgments

I would like to express my sincere gratitude to my advisor, Dr. Marcelo Dapino, for providing invaluable guidance and encouragement for the past two years, and for giving me the opportunity to work on this research project. I have learnt a lot from him during the course of this research work.

I would like to thank Dr. Leon Headings for providing feedback that has been instrumental in shaping this thesis. He has been a great resource and I thoroughly enjoyed working with him.

I am thankful to Allen Sheldon of Honda R&D Americas for providing funding and support, without which this project would not have been possible, and also for helping me learn LS-DYNA.

I am grateful to Dr. Daniel Mendelsohn for serving on the examination committee. I am thankful to Joseph West for letting me borrow equipment from the electronics lab. I would also like to thank my colleagues in the Smart Materials and Structures Lab for their support along the way.

Finally, I would like to express my heartfelt appreciation to my parents. It is only because of their unwavering faith in me, that I had the opportunity to join the Master's program at OSU.

Vita

May 14, 1988 ....Born - Thane, Maharashtra, India

May, 2010 ...............................B.E., Mechanical Engineering,
University of Pune, India

January 2011-present ....Graduate Research Associate,
The Ohio State University,
Columbus, OH.

Fields of Study

Major Field: Mechanical Engineering

Studies in Smart Materials and Structures: Dr. Marcelo Dapino

Table of Contents

List of Tables

List of Figures

Chapter 1: INTRODUCTION

This chapter introduces the polymer polyvinylidene fluoride. This is the piezo-electric material present in the sensors which are the focus of this research project. A brief literature review has been presented to give an insight into the variety of research being conducted in this field. The objectives of this research have also been explained, followed by the organization of this thesis.

1.1 Introduction to polyvinylidene fluoride (PVDF)

Polyvinylidene fluoride, abbreviated as PVDF, is a mechanically tough, flexible, low density ferroelectric polymer available in the form of films. When it is crystallized into its beta phase, it can be polarized and can act as a piezoelectric transducer, converting mechanical energy into electrical energy and vice versa. This implies that it can be used both as a sensor as well as an actuator.

PVDF film is an excellent sensor because it has a very high sensitivity to stress and strain and is capable of generating high voltages, on the order of hundreds of Volts. PVDF has high dielectric strength, making it capable of withstanding high voltages. As a sensor, PVDF film requires neither external power nor sophisticated circuitry to be able to use its voltage output. Being highly compliant (almost ten times as compliant as piezoceramics), it can adhere to a wide variety of surfaces with

the help of simple bonding techniques. It is also a very stable material, resisting moisture and most chemicals [1].

When a PVDF sensor is bonded to a structure, it generates charge proportional to the stress transferred to it by the structure. If the structure is stiff, the transfer of strain may be low but the PVDF sensor still generates a response since PVDF is inherently sensitive to stress. Thus, even low strain in the structure can lead to the generation of high amplitude signals, making the PVDF film a better sensor compared to strain gauges.

While PVDF film is very useful for sensing applications, it is a poor actuator, especially for applications requiring transmission of high magnitudes of force. The polarized PVDF film also exhibits the pyroelectric effect, generating voltage when it is heated. Typically, PVDF film generates 1.5 V open circuit voltage when heated by 1° Celsius.

A PVDF sensor typically consists of a PVDF film sandwiched between thin films of electrodes. Leads are connected to the electrodes to enable measurement of the voltage generated by PVDF film.

1.2   Literature review

Obara et al. [2] used PVDF film to design an inexpensive stress sensor to measure the stress behind a shock wave. The PVDF sensor consisted of a PVDF disc of 25 μm thickness and 1.5 mm diameter. It was punched from a PVDF sheet and placed into a hole in a sheet of Mylar 24 μm thick. The two surfaces of the PVDF film were connected with brass foils 25 μm in thickness using conducting double-sided tape. For calibration of the PVDF sensor, an impact experiment was set up. The PVDF
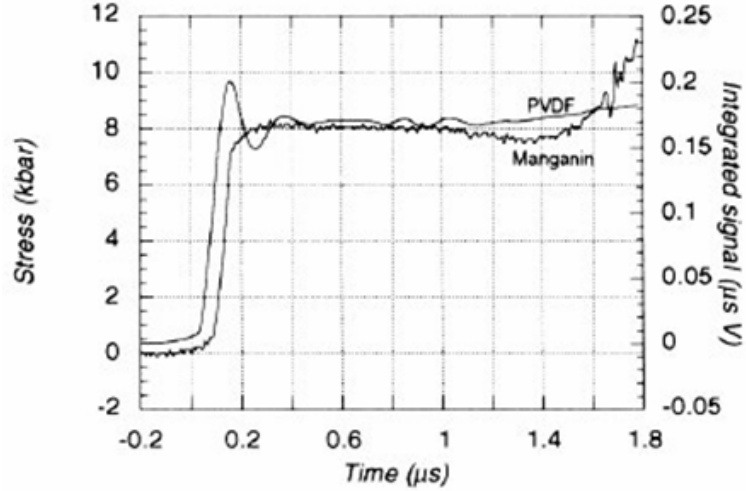
Figure 1.1: Comparison of the output of the PVDF stress sensor and the manganin piezoresistive sensor [2].

sensor's output was compared with that of pre-calibrated manganin piezoresistive sensors. The sensors were placed between two PMMA blocks and were separated from each other by a 25 µm Mylar sheet. They were aligned such that they were impacted axially. Projectile velocity of up to 600 m/s was used. A current viewing resistor (51 Ω) was placed across the PVDF sensor and the voltage across it was measured. The charge produced by the sensor is proportional to the stress acting on the sensor. The charge generated by the sensor flows through the current viewing resistor and causes a voltage to appear across the resistor. This voltage is measured by the oscilloscope and is proportional to the time derivative of the charge generated by the sensor. Hence, the voltage measured by the oscilloscope is proportional to the time derivative of the stress. Time integration was carried out over the measured voltage and the stress history is proportional to the curve obtained. This integrated voltage-time PVDF output was compared with the stress history obtained from the

3

manganin sensor as shown in Figure 1.1. It can be seen that both sensors have similar rise times for the shock pulse. The PVDF signal shows an overshoot not shown by the manganin sensor. This might be attributed to the response of the sensor material itself. From Figure 1.1 it can be seen that the response of the PVDF sensor is close to that of the pre-calibrated manganin sensor. Thus, the authors showed that the PVDF sensor shows a very fast response time (approximately 100 ns) and can be used to record the stress history of an impacted specimen.

Zhu et al. [3] experimentally demonstrated that PVDF sensors can measure shock waves (on the order of nanoseconds). The PVDF film was used in 33 mode in this study. Dutta and Kalafut [4] fabricated PVDF shock gauges for soil shock sensing. They reported a very large signal-to-noise ratio and used a charge divider to attenuate the PVDF sensor's output. Mori et al. [5] used a PVDF stress gauge to determine the stress profile in a polytetrafluoroethylene (PTFE) specimen after impacting it with a PTFE flyer plate with an impact velocity of 295 m/s.

Gaul and Hurlebaus [6] developed an experimental method for detection of impact using PVDF film sensors. PVDF sensors were bonded intimately to the surface of the specimen using adhesive tapes. Flexural waves were created in a square plate specimen by impacting it with a pendulum. The PVDF sensors were loaded in the in-plane directions because of the flexural waves caused by impact. Using the PVDF sensor signals and the equations that the authors developed for the case of point impact on a plate, the force-time history was obtained.

Kuhr and Blackshire [7] conducted a study on the use of PVDF films to detect and quantify impact damage in a ceramic matrix composite (CMC) wrapped structure. The results showed that it is possible to determine the intensity of the impact based

on the increase in the frequency content of the generated voltage signal. A quadratic relationship was observed between the impact damage and the peak-to-peak PVDF voltage, indicating that it is possible to characterize impact damage based on the PVDF sensor's signals.

Bauer [8] studied the response of the PVDF at very high applied pressure. He showed that the PVDF sensor's response was independent of the loading path (up to 35 GPa) and that the results were reproducible even when the materials of the impactor and target were interchanged. The PVDF film used in this study was processed using the Bauer cyclic poling method [9].

Ren et al. [10] fabricated a curved PVDF sensor for human pulse measurement and showed that increasing the curvature of the sensor lead to an increase in sensitivity. Chen and Wang [11] experimentally demonstrated that arrays of PVDF sensors bonded to a cantilever beam and to a simply supported plate can be used to identify natural frequencies, damping ratios, and mode shapes of the structures.

Anuphap-udom et al. [12] fabricated an acoustic emission sensor using PVDF film. They demonstrated experimentally that it can be used to detect acoustic emissions signals generated by the bearings in a rotodynamic test rig and to identify different operating conditions of the bearings.

Muñoz [13] discusses an interfacing circuit for PVDF sensors based on differential signals, which improve the signal-to-noise ratio. The first stage of the circuit consists of a differential charge amplifier and the the second stage is an instrumentation amplifier. This circuit is used to demonstrate experimentally that the nature of impact can be determined based on the frequency content of a PVDF sensor's signal. It is also shown that the ability of a PVDF sensor to identify impact depends upon its resonant

frequency. While the author presents a complicated circuit for recording clean PVDF sensor signals, this thesis demonstrates that simpler voltage measurement methods are available. In fact, Chapter 5 describes an experiment in which very low amplitude signals, with low noise, were recorded using simply an oscilloscope and 10x probes.

1.3   Research objectives

Most of the literature reviewed focuses on detection of out-of-plane stress using PVDF sensors, whereas this thesis will focus on in-plane stress. The underlying motivation for this research is the fact that PVDF film, being an excellent sensor as evident from the previous sections, is well suited for applications requiring detection and monitoring of highly dynamic and transient events like impacts on structures. The overall objective of this research is to understand the key aspects of PVDF sensors for the detection of transient stress waves in a structure. This can be broken down into the following goals:

1. Develop and validate an experimental method to demonstrate that PVDF sensors can be used to determine the impact force acting on a structure.

2. Create a model in LS-DYNA to simulate the impact experiments and enable the calculation of the PVDF sensor's expected output voltage.

3. Demonstrate that PVDF sensors can be used to detect stress waves propagating at a high speed.

4. Analyze the effect of stress averaging on the PVDF sensor's output.

1.4 Thesis organization

This thesis is divided into seven chapters. Chapter 2 explains the modes of operation of the PVDF sensor and provides details of the voltage measurement technique that was used for most of this research.

Chapter 3 and Chapter 4 focus on the first research goal listed in the previous section. Chapter 3 describes the impact experiments performed on a solid stainless steel bar and the associated LS-DYNA simulation model. It presents a method for calculating a proportionality constant between the PVDF sensor's voltage output and the impact force. Chapter 4 describes the impact experiments performed on a more complex structure, namely, a hollow steel beam, using the impact test methodology developed in Chapter 3. The LS-DYNA model of impact on the hollow steel beam is also explained and evaluated in this chapter.

Chapter 5 focuses on the second research goal. It describes an experiment in which the PVDF sensors were used to measure the speed of sound for longitudinal waves in a slender rod.

Chapter 6 focuses on the third research goal. It details the derivation of relations that describe the stress averaging effect of a PVDF sensor for two types of inputs, namely, periodic applied stress and impact-induced stress. In addition, the results of a parametric study of sensor and structure's parameters, based on these relations are presented.

Finally, the conclusions of this research are presented in Chapter 7.

Chapter 2: PVDF MODES OF OPERATION AND VOLTAGE MEASUREMENT

This chapter describes how a PVDF sensor operates, the voltage measurement techniques used, and the effect of interfacing circuits on the voltage measured by the data acquisition system. Figure 2.1 defines the 1, 2, and 3 axes/directions for a PVDF sensor.

2.1 Description of the PVDF sensor

The commercially available PVDF sensor LDT1-028K, manufactured by Measurement Specialties Inc. (MSI) was used in most of the experiments performed in this research. Figure 2.2 [14] shows a diagram of the LDT1-028K sensor. The sensor consists of a 28 µm thick PVDF film sandwiched between two 6 µm thick silver ink electrodes. This assembly is sandwiched between two 55 µm thick Mylar sheets. Two leads are attached to the sensor. The capacitance of the LDT1-028K PVDF sensor was measured as 1.57 nF.
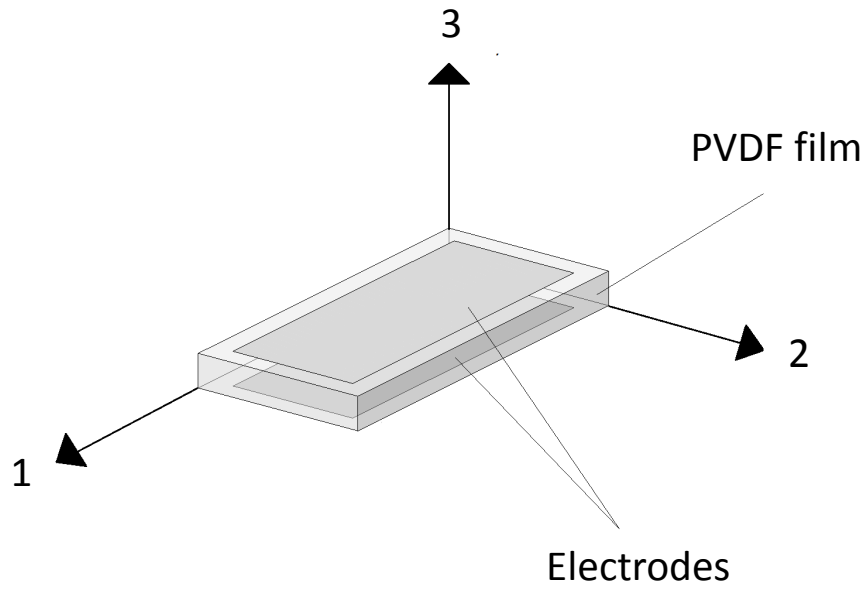
Figure 2.1: Diagram showing the PVDF sensor's axes.
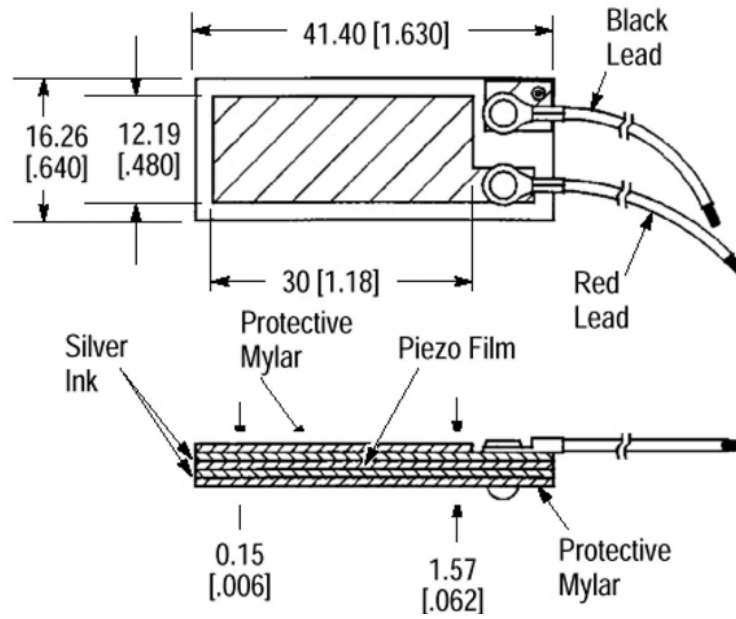
Figure 2.2: PVDF sensor LDT1-028K (dimensions outside brackets are in mm; dimensions inside brackets are in inches) [14].

9

2.2 Linear piezoelectric equations

Constitutive equations and relevant material and electrical properties are essential to understand the behavior of the PVDF sensor. This section starts with the general constitutive equations describing the linear behavior of piezoelectric materials like the PVDF sensor and derive the relation that will be most useful for the type of analysis done in this research. Table 2.1 shows a list of most of the symbols used in this section.

Symbol	Meaning	SI unit
D	Electric displacement	C/m^2
E	Electric field	V/m
g	Piezoelectric stress constant	$V/m/N/m^2$
S	Strain	
T	Stress	N/m^2
s	Elastic compliance	m^2/N
h	Thickness	m
β	Dielectric impermittivity	m/F

Table 2.1: List of symbols.

The electric field generated by the PVDF sensor and the stress acting on the PVDF sensor are the two parameters that will be required for analysis of the experimental and simulation based data in this research. The sensing formulation or strain-field formulation of the linear piezoelectric equations is [15]

$$S_p = s_{pq}^D \cdot T_q + g_{kp} \cdot D_k. \tag{2.1}$$

$$E_i = g_{iq} \cdot T_q + \beta_{ik}^T \cdot D_k. \tag{2.2}$$

Here the tensor notations i and k take the values 1, 2, and 3; while the compressed matrix notations p and q take the values 1 through 6. The superscripts D and T indicate that the values of the corresponding parameters are measured at zero electric displacement and zero stress, respectively. The compressed matrix notations and the tensor notations can be related to each other using Table 2.2. The inverse effect,

Tensor notation	Matrix notation
11	1
22	2
33	3
23 or 32	4
31 or 13	5
12 or 21	6

Table 2.2: Tensor and matrix notations.

described by (2.1), pertains to the development of strain in the PVDF film when a voltage is applied across its electrodes, while (2.2) describes the direct effect which is the generation of an electric field when the PVDF film is subjected to stress. Since this thesis is concerned with the use of PVDF film as a stress sensor, (2.2) is the main equation of interest.

In the experiments that were conducted as a part of this research, a high value resistance was always connected across the PVDF sensor while recording its response. This can be approximated to be an open circuit condition. This implies that there is zero current across the electrodes of the PVDF sensor and thus, the electric displacement is zero ($D = 0$).

Substituting $D = 0$ in (2.2) one obtains

$$E_i = g_{iq} \cdot T_q, \qquad (2.3)$$

which (2.3) can be expanded as

$$\begin{bmatrix} E_1 \\ E_2 \\ E_3 \end{bmatrix} = \begin{bmatrix} 0 & 0 & 0 & 0 & g_{15} & 0 \\ 0 & 0 & 0 & g_{24} & 0 & 0 \\ g_{31} & g_{32} & g_{33} & 0 & 0 & 0 \end{bmatrix} \cdot \begin{bmatrix} T_1 \\ T_2 \\ T_3 \\ T_4 \\ T_5 \\ T_6 \end{bmatrix}, \qquad (2.4)$$

where g_{31}, g_{32}, and g_{33} define the relation between the normal stress in the 1, 2, and 3 directions (T_1, T_2, and T_3 respectively) and the electric field in the poling direction, namely E_3. The constant g_{24} gives the relation between the shear stress in the 2-3 plane and the electric field E_2, while g_{15} gives the relation between the shear stress in the 1-3 plane and the electric field E_1 [16].

When the PVDF film is used as a sensor, E_1 and E_2 are zero since no external field is applied to the sensor. The only field that is generated will be in the poling direction, namely E_3. Thus, substituting $E_1 = 0$ and $E_2 = 0$ in (2.4), one obtains

$$E_3 = g_{31} \cdot T_1 + g_{32} \cdot T_2 + g_{33} \cdot T_3. \qquad (2.5)$$

Here, T_1 is the longitudinal stress, T_2 is the lateral stress and T_3 is the compressive stress. Electric field E_3 can be expressed as V/h, where V is the voltage generated by the PVDF sensor and h is the thickness of the PVDF film. This leads to

$$V = g_{31} \cdot T_1 \cdot h + g_{32} \cdot T_2 \cdot h + g_{33} \cdot T_3 \cdot h. \qquad (2.6)$$

Some typical properties of the PVDF film, provided by MSI, are shown in Table 2.3. Substituting the values of g_{31}, g_{32}, g_{33} and h in 2.6, one obtains

$$V = (6.048 \times 10^{-6}) \cdot T_1 + (0.528 \times 10^{-6}) \cdot T_2 - (9.24 \times 10^{-6}) \cdot T_3. \qquad (2.7)$$

12

Symbol	Parameter	Value	Units
d_{31}	Piezoelectric strain constant in the 1 direction	23×10^{-12}	$\dfrac{\text{m/m}}{\text{V/m}}$
d_{33}	Piezoelectric strain constant in the 3 direction	-33×10^{-12}	$\dfrac{\text{m/m}}{\text{V/m}}$
g_{31}	Piezoelectric stress constant in the 1 direction	216×10^{-3}	$\dfrac{\text{V/m}}{\text{N/m}^2}$
g_{33}	Piezoelectric stress constant in the 3 direction	-330×10^{-3}	$\dfrac{\text{V/m}}{\text{N/m}^2}$
ϵ/ϵ_0	Relative permittivity	12-13	
E_s	Elastic modulus	2-4	GPa
ρ_s	Mass density	1780	kg/m^3
h	Film thickness	28	µm

Table 2.3: Properties of the LDT1-028K sensor [1].

2.3   Modes of operation of the PVDF sensor

The PVDF sensor can be used in two distinct modes to measure stress, the 31 mode and the 33 mode. For piezoelectric films, the poling direction is usually along the thickness, i.e. the 3 direction. The first digit in both 31 and 33 modes refers to the direction of polarization of the PVDF film. The second digit refers to the direction of the applied stress. Figure 2.3 shows examples of 31 mode and 33 mode of operation.

2.3.1   33 mode of operation

In the 33 mode of operation, the stress is applied in the 3 direction (or compression direction). To effectively use the PVDF sensor in 33 mode, the sensor must be positioned on the structure in such a way that it falls directly in the path of the applied load. In other words, this means that the PVDF sensor is compressed in the thickness direction in 33 mode. Thus, the PVDF sensor acts as a pressure sensor
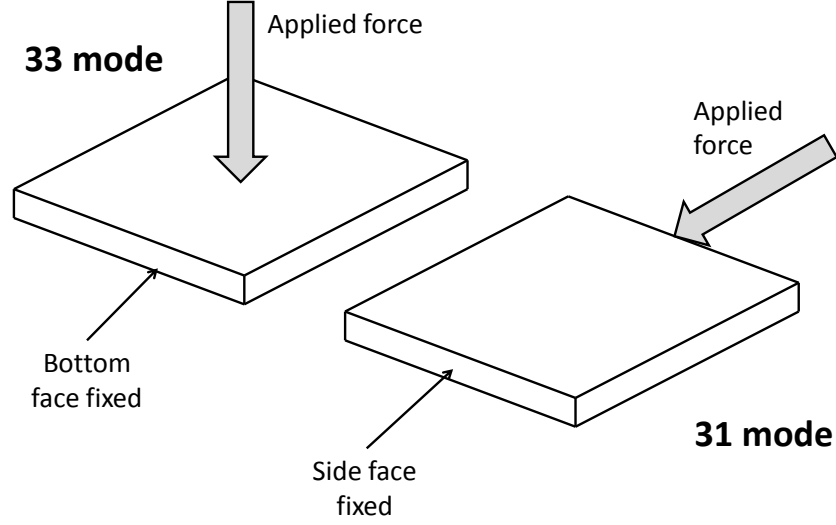
Figure 2.3: Left: 33 mode of operation; right: 31 mode of operation.

in 33 mode. The piezoelectric stress constant of relevance in this mode is g_{33}. The structure must be rigid in order to use the PVDF sensor in 33 mode.

2.3.2 31 mode of operation

From the definition of the 31 mode of operation, it is evident that the applied stress in this mode is in the longitudinal direction, or the 1 direction. This can be achieved in multiple ways. As an example, consider a PVDF sensor that is bonded to a flexible substrate. Upon bending of the structure, the PVDF sensor experiences significant stress along the 1 direction because the neutral axis no longer passes through the center of the PVDF. Another example of 31 mode is bonding the PVDF sensor to the sides of a bar and impacting it at the top. This is the method that was used in the impact tests on the solid bar and the hollow beams, which have been explained in Chapter 3 and Chapter 4 respectively.

In the experiment using the solid bar, PVDF sensors were bonded to the sides of the solid bar. During each impact event, the impactor hits the top of the solid bar. The force exerted by the impactor on the top of the solid bar leads to the development of longitudinal strain in the bar. The PVDF sensors bonded to the side of the bar are also subjected to the impact-induced longitudinal strain. In an ideal case, the amount of strain on the surface of the bar at the location where the PVDF sensor was bonded would be the same as the amount of strain in the PVDF sensor. However, the PVDF film in the sensor is separated from the solid bar's surface by layers of Mylar (55 μm), silver ink electrode (6 μm), and cyanoacrylate glue. Hence there is a small difference in the amount of strain developed in the PVDF film and the amount of strain developed in the solid bar at the PVDF sensor's location. Thus, the strain acting along the 1 direction leads to the development of stress in the 1 direction, thereby causing the generation of voltage by the PVDF sensor. The piezoelectric stress constant of relevance in this mode is g_{31}.

2.4 Measurement of the PVDF sensor's voltage

2.4.1 Circuit models of the PVDF sensor

A PVDF sensor is capacitive in nature. A model for the equivalent circuit of a PVDF sensor is required in order to analyze the interfacing circuit between the PVDF sensor and the measurement system. There are two equivalent circuit models that can be used for the PVDF sensor. The PVDF sensor can be modeled either as a voltage source in series with the PVDF film capacitance or as a charge source shunted by the internal resistance in parallel with PVDF film capacitance.
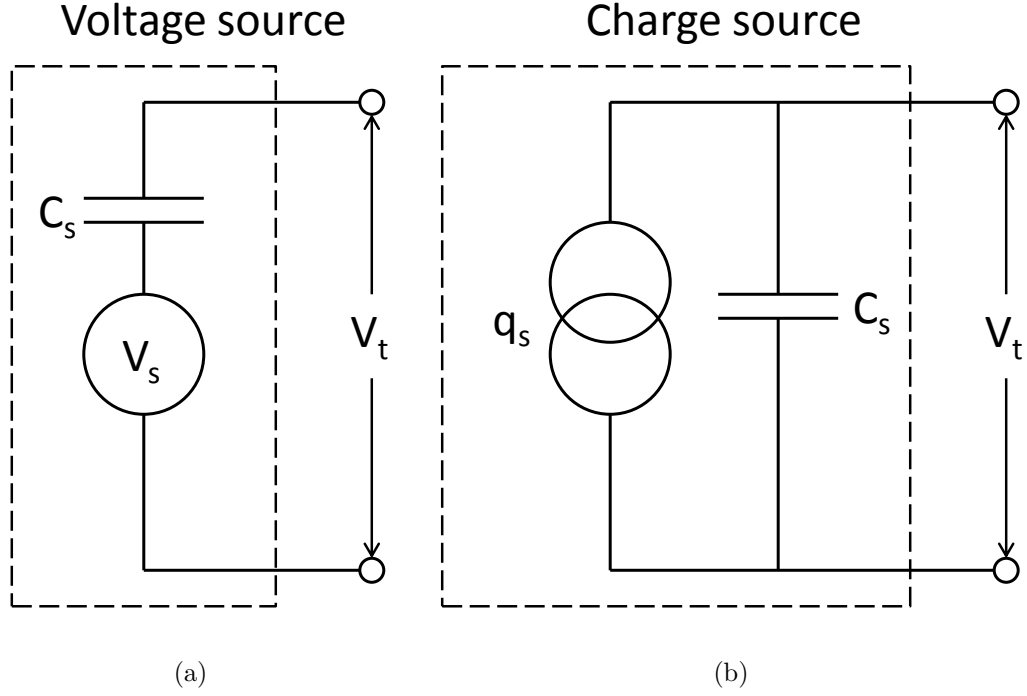
Figure 2.4: Diagram showing (a) the voltage source and (b) the charge source equivalent circuit models of a PVDF sensor.

The voltage source model is shown in Figure 2.4(a), in which V_s denotes the voltage generated by the sensor (which is directly proportional to the applied stress), C_s denotes the internal capacitance of the PVDF film, and V_t is the voltage available across the terminals of the PVDF sensor. The charge source model is shown in Figure 2.4(b). In both cases, the part of the circuit inside the dotted rectangle comprises the PVDF sensor.

The voltage source equivalent circuit model of the PVDF sensor is most commonly used for analysis of interfacing circuits. Hence, this is the model that will be used for all circuit analyses in this chapter.

2.4.2 Recording the PVDF sensor's voltage

Most other sensors require an amplification of their generated voltage signals before they can be used. The PVDF sensor, on the other hand, generates very high voltages in both 31 mode and 33 mode. During the impact experiment, the LDT1-028K sensors often generated voltages exceeding 10 V in magnitude. Most data acquisition systems have signal conditioning units that cannot accept voltages in excess of $\pm$ 10 V. Hence, in order to record the PVDF sensor's signal safely, either a voltage reduction interfacing circuit must be used or a data acquisition system that has a high maximum input voltage rating must be used. Furthermore, the duration of an impact is usually less than 5 ms. Since the time window of interest is very small, a high sampling speed is required to obtain good data resolution.

An oscilloscope (Agilent 54622A) was used to record the voltage generated by the PVDF sensor because it satisfies both criteria mentioned above. The oscilloscope has a maximum input voltage rating of 400 V and a sampling rate of 100 MHz. The PVDF sensor's terminals were connected to 10x probes (Agilent 10074C), which were connected to the input terminals of the oscilloscope. The 10x probes have a resistance of $9\,\text{M}\Omega$ and the oscilloscope has an input resistance of $1\,\text{M}\Omega$. When a 10x probe is connected to the oscilloscope's input terminal, a voltage divider is formed with a reduction ratio of 10. Thus, the total resistance connected across the PVDF sensor's terminals was $10\,\text{M}\Omega$ and the voltage measured by the oscilloscope was one tenth of the voltage between the terminals of the PVDF sensor.

2.4.3 Triggering data acquisition systems

In addition to the PVDF sensors, the test setup for each impact experiment also included a load cell which was attached to the impactor. The load cell was connected to the Instron Impulse data acquisition (DAQ) system. The Impulse DAQ consisted of a signal conditioning unit and data recording software. The Impulse DAQ was set up so that it triggered acquisition of the load cell's signal based on its own voltage level. To ensure that the entire signal was captured, a pre-trigger time was defined in the Impulse DAQ system. This helped record the useful part of the signal just before the trigger level was met as well. The voltage level of the load cell was used as a trigger for the oscilloscope by using a BNC cable to connect the output terminal of the Impulse signal conditioning unit to the external trigger input terminal at the oscilloscope. The oscilloscope was also configured to have a fixed pre-trigger time to ensure that the entire useful part of the PVDF sensor's signal was captured.

2.5 Determination of the PVDF sensor's generated voltage

Almost all the experiments in this thesis had the PVDF sensor directly connected to the oscilloscope, through the 10x probes. The circuit for this configuration is shown in Figure 2.5. The circuit uses the voltage source equivalent circuit model of the PVDF sensor. The PVDF sensor, being capacitive in nature, forms an RC circuit with the input resistance of any measuring instrument that is connected across it. In the case of the circuit shown in Figure 2.5, a high pass filter is formed by the internal capacitance of the sensor, and the probe and oscilloscope resistances. The time constant (RC) of this circuit is 15.7 ms.
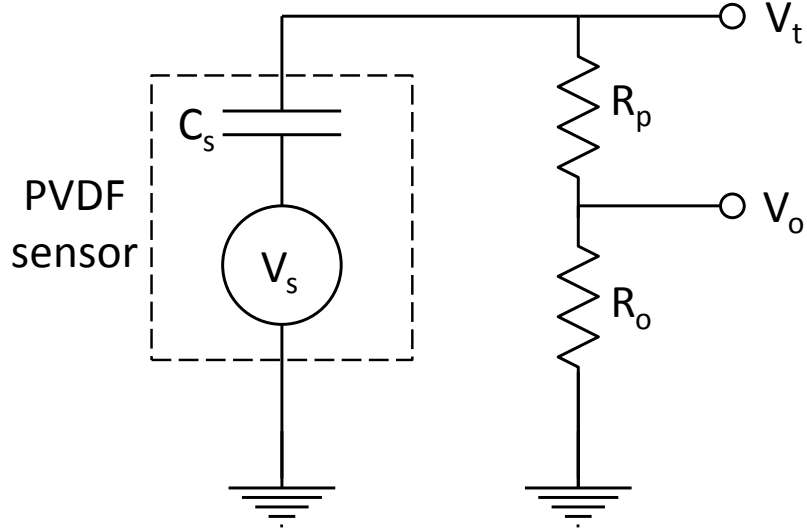
Figure 2.5: PVDF sensor directly connected to the oscilloscope via a 10x probe.

The resistance of the probes, $R_p = 9\,\text{M}\Omega$ and the input resistance of the oscilloscope, $R_o = 1\,\text{M}\Omega$. The input capacitance of the oscilloscope is about 14 pF. It has been neglected in the circuit since it is very small compared to the internal capacitance C_s. V_o is the voltage measured by the oscilloscope, V_s is the voltage generated by the PVDF sensor, and V_t is the voltage across the terminals of the PVDF sensor. The series combination of $(R_p + R_o)$ and the capacitor C_s form a potential divider. Hence, in Laplace notation, one can write

$$V_t(s) = \left(\frac{R_p + R_o}{R_p + R_o + \frac{1}{sC_s}} \right) \cdot V_s(s), \tag{2.8}$$

or,

$$V_t(s) = \left[\frac{sC_s(R_p + R_o)}{sC_s(R_p + R_o) + 1} \right] \cdot V_s(s). \tag{2.9}$$

The resistances R_p and R_o also form a potential divider. Hence, one can write

$$V_o(s) = \left(\frac{R_o}{R_p + R_o} \right) \cdot V_t(s). \tag{2.10}$$

19

From (2.9) and (2.10), one obtains

$$V_o(s) = \left[\frac{sC_s(R_p + R_o)}{sC_s(R_p + R_o) + 1}\right] \cdot \left[\frac{R_o}{R_p + R_o}\right] \cdot V_s(s). \tag{2.11}$$

Thus, one obtains the transfer function $H(s)$ between V_o and V_s as

$$H(s) = \frac{V_o(s)}{V_s(s)} = \left[\frac{sC_s(R_p + R_o)}{sC_s(R_p + R_o) + 1}\right] \cdot \left[\frac{R_o}{R_p + R_o}\right], \tag{2.12}$$

which can be referred to as the measurement transfer function as it relates the voltage measured by the oscilloscope (V_o) to the physical voltage generated by the sensor (V_s). Thus, it can be seen that the RC circuit formed by the sensor and the measurement system is modeled by the measurement function $H(s)$. Substituting known values in (2.12), one obtains

$$H(s) = \frac{V_o(s)}{V_s(s)} = \frac{1}{10}\left(\frac{0.0157s}{0.0157s + 1}\right) = \frac{1}{10}\left(\frac{s}{s + 63.69}\right). \tag{2.13}$$

The cutoff frequency of the first-order high-pass RC filter seen here is

$$f_c = \left[\frac{1}{2\pi(R_p + R_o)C_s}\right] = 10.14\,\text{Hz}. \tag{2.14}$$

Thus, all frequencies lower than 10.14 Hz will be attenuated by the filter and the voltage V_o measured by the oscilloscope will not be the same as the true generated voltage V_s. The inverse measurement function can be written as

$$H^{-1}(s) = \frac{V_s(s)}{V_o(s)} = 10\left(\frac{s + 63.69}{s}\right). \tag{2.15}$$

Therefore

$$V_s(s) = H^{-1}(s) \cdot V_o(s) = 10\left(\frac{s + 63.69}{s}\right) \cdot V_o(s). \tag{2.16}$$

Thus, V_s can be determined by using the inverse measurement function $H^{-1}(s)$ and the measured voltage V_o. This was achieved by creating a simple model in Simulink

20

to apply the inverse transfer function to the voltage signal recorded using the oscillo-scope. The block diagram shown in Figure 2.6 summarizes the process of determining the voltage generated by the sensor. Assuming that $H(s)$ correctly models the RC circuit formed by the sensor and the measurement system, the generated voltage cal-culated using $H^{-1}(s)$ and V_o will be equal to the physical voltage generated by the sensor. This means that the first and last blocks shown in Figure 2.6 are the same. Throughout the rest of this thesis, this calculated voltage has been referred to as generated voltage.

Physical voltage generated by the sensor
V_s

RC circuit formed by the sensor &
measurement system, modeled by H(s)

Voltage measured by the oscilloscope
V_o

Inverse measurement function
$H^{-1}(s)$

Generated voltage
$H^{-1}(s) \cdot V_o$
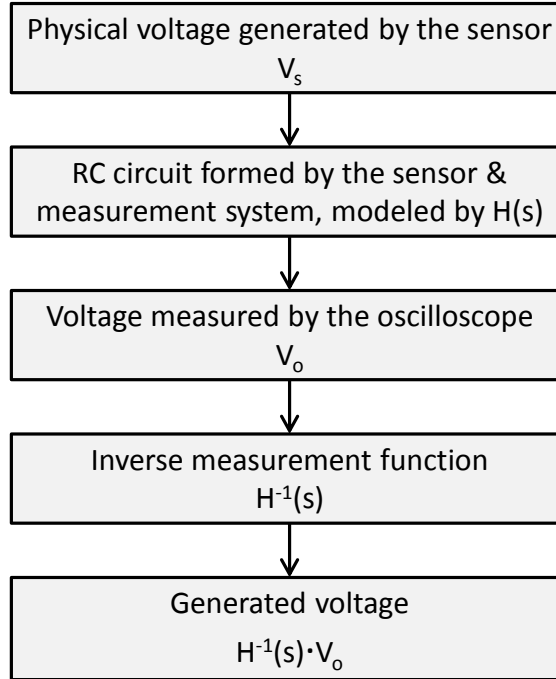
Figure 2.6: Block diagram showing the process of determining the voltage generated by a PVDF sensor.

Figure 2.7 shows the measured voltage and the generated voltage. The blue curve was obtained after applying the inverse measurement function $H^{-1}(s)$ to the measured voltage data, using Simulink. The measured voltage V_o is proportional to terminal voltage V_t, which is equal to the difference between the generated voltage and the voltage drop across the internal capacitance C_s. Charging of the internal capacitance over time increases the voltage drop across it. Thus, over time, the difference between V_s and V_o increases because of the increasing voltage drop across the internal capacitance. Hence, the two signals shown in Figure 2.7 appear to be the same initially (when the capacitor has not had enough time to charge) and increasingly differ as time passes. Eventually, the signals appear to move close to each other again. This is because the sensor stops generating voltage at about 4 ms and the generated and measured signals both drop to zero eventually.
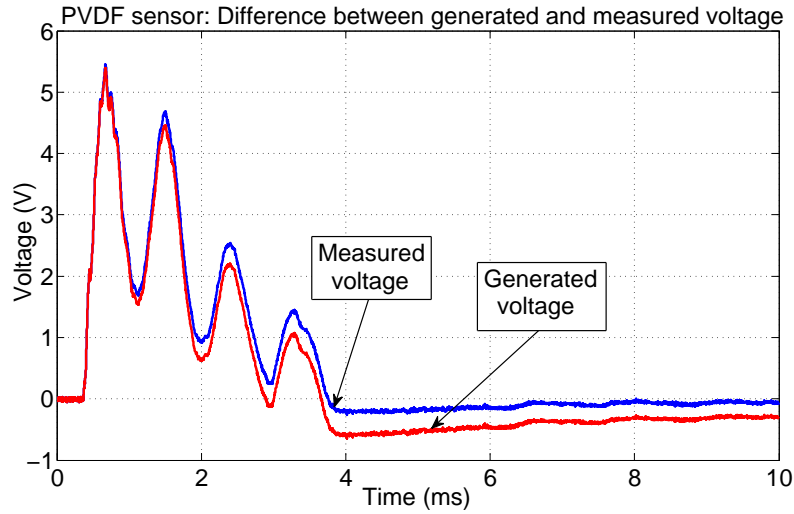
Figure 2.7: Difference between the voltage measured by the oscilloscope and the voltage generated by the PVDF sensor.

2.6 Interfacing circuits

In situations where it is not possible to use an oscilloscope for the PVDF sensor's voltage measurement, it is important to have a stable interfacing circuit between the sensor and the DAQ system. The purpose of such a circuit is to isolate the PVDF sensor from the DAQ system. Since most DAQ systems have a maximum input voltage rating of 10 V, the interfacing circuit must also attenuate the voltage across the PVDF sensor's terminals before it is supplied to the DAQ system. In this section, some interfacing circuits and their corresponding measurement functions are discussed that satisfy the above criteria. These circuits were used to measure PVDF voltages and the results were then compared against each other.

2.6.1 Circuit 1
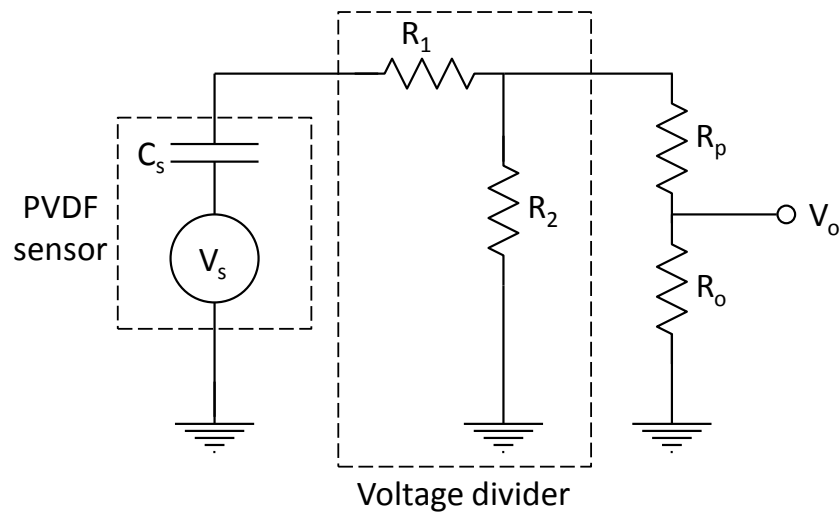
Figure 2.8: Circuit 1 - Voltage divider connected between the PVDF sensor and the 10x probes.

Circuit 1 consists of a voltage divider connected between the PVDF sensor and the oscilloscope, as shown in Figure 2.8, where $R_1 = 1\,\text{M}\Omega$ and $R_2 = 0.1\,\text{M}\Omega$. Thus, the voltage divider reduces the voltage across the PVDF sensor's terminals by a factor of 11 before it reaches the 10x probes. In this case, the net resistance connected across the sensor $1.099\,\text{M}\Omega$. Hence, the measurement function is

$$H^{-1}(s) = \frac{V_o(s)}{V_s(s)} = \frac{1}{110}\left(\frac{s}{s + \frac{1}{RC}}\right) = \frac{1}{110}\left(\frac{s}{s + 579.56}\right). \tag{2.17}$$

2.6.2 Circuit 2
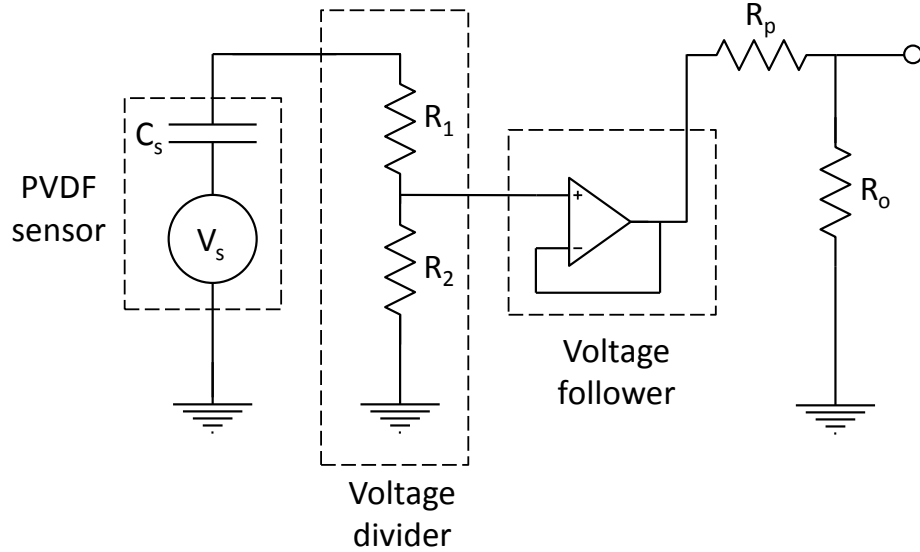
Figure 2.9: Circuit 2 - Voltage divider and voltage follower connected between the PVDF sensor and the 10x probes.

Circuit 2 consists of a voltage divider and a voltage follower connected between the PVDF sensor and the oscilloscope, as shown in Figure 2.9, where $R_1 = 1\,\text{M}\Omega$ and $R_2 = 0.1\,\text{M}\Omega$ respectively. In this case, the net resistance connected across the sensor

24

R = 1.1 MΩ. Hence, the measurement function is

$$H^{-1}(s) = \frac{V_o(s)}{V_s(s)} = \frac{1}{110}\left(\frac{s}{s + \frac{1}{RC}}\right) = \frac{1}{110}\left(\frac{s}{s + 579.04}\right). \qquad (2.18)$$

2.6.3 Comparison of interfacing circuits
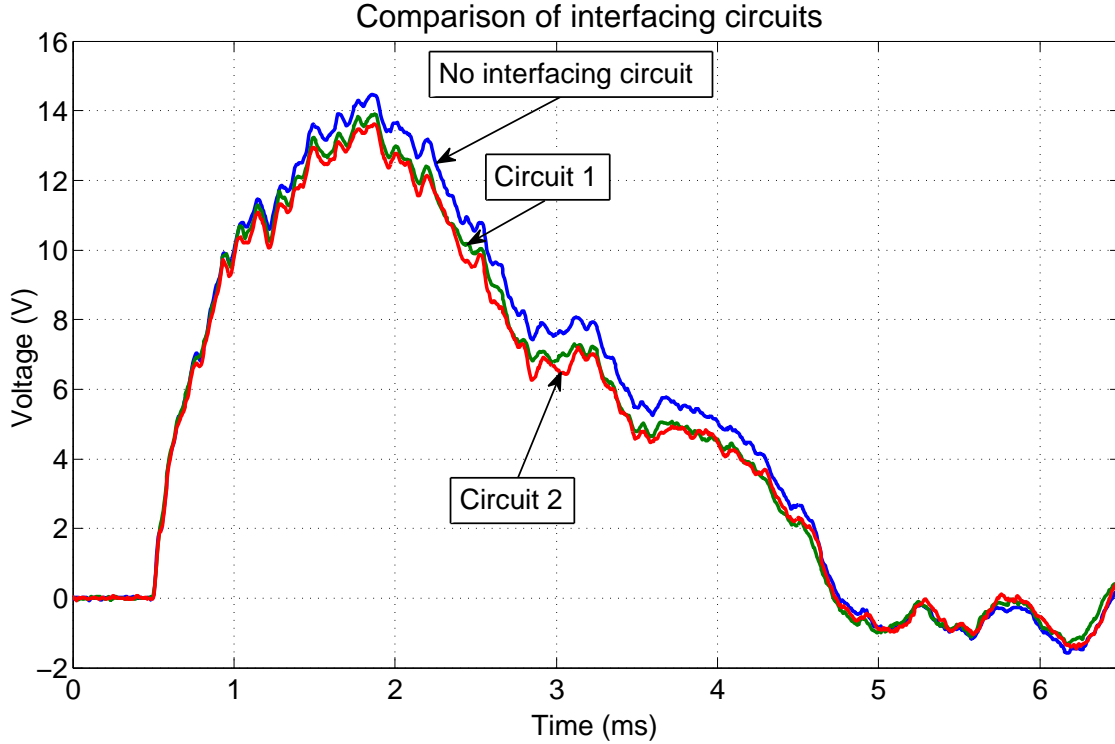
Figure 2.10: Generated (V_s) signals measured without a circuit, with a voltage divider, and with a voltage divider and a follower.

Three drop tests were conducted from the same drop height. For the first drop test, no interfacing circuit was used; the PVDF sensor was directly connected to the 10x probes. For the second and third drop tests, interfacing circuits 1 and 2 respectively, were used. The generated sensor voltages were determined using the

relevant measurement functions. The impact forces in all three drop tests are almost identical. Hence, the generated voltage responses of the drop tests can be compared to evaluate the performance of the two interfacing circuits. Figure 2.10 shows the comparison of generated voltage signals. Since the signals shown in Figure 2.10 are very close to each other, one can conclude that both of the interfacing circuits provide an undistorted voltage to the oscilloscope. Using appropriate measurement functions, either of the two circuits can be used for determining the voltage generated by the PVDF sensor.

It is noted that the op-amp selected for the voltage follower should have a slew rate that is fast enough to capture important features in the voltage signal caused by impact. The op-amp used here (LF411CN) has a slew rate of 10 V/µs, which is fast enough for the recorded signals.

2.7   Conclusions

- The voltage generated by the PVDF sensor differs from the voltage recorded by the measurement system. The generated voltage can be determined using the measured voltage and a measurement function, as described in detail in this chapter.

- Some measurement systems may have a lower input voltage range compared to the voltage generated by the PVDF sensors. In addition, it may be recommendable to isolate the sensors from the measurement system, both as a safety mechanism to prevent damage to the DAQ due to high voltages as well as to provide a single, known measurement function independent of the input impedance of the DAQ. In such cases, simple interfacing circuits consisting of a voltage divider and follower can be used for determining the voltage generated by the PVDF sensor if the correct measurement function is applied to the measured signals.

Chapter 3: PVDF SENSORS ATTACHED TO A SOLID BAR

This chapter introduces the impact experiments and explains in detail the set of drop tests performed on a solid bar. The associated LS-DYNA simulation model has been described in detail as well. Finally, the results of the simulation have been analyzed and the conclusions drawn have been explained.

3.1 Solid stainless steel bar

The simple structure chosen for the impact test was a solid stainless steel bar. The solid bar had a cross-section of 50.5 mm x 31 mm, and a height of 131.5 mm. A base plate was welded to the bottom of the solid bar to help fix the bar to the base of the impact tester. The dimensions of the solid stainless steel bar are shown in Figure 3.1. The material used for both the bar and the base plate was 316 L stainless steel.

Figure 3.2 shows the solid bar with the PVDF sensors attached. Each of the two PVDF sensors is bonded to the solid bar at a distance of 14 mm from the top, in the center of the bar's face. This means that 14 mm is the distance between the top edge of the Mylar layer on the PVDF sensor and the top of the solid bar. Commercially available cyanoacrylate glue (Krazy glue) is used for bonding the PVDF sensors to the surface of the solid bar. The glue is applied uniformly to the surface of the PVDF
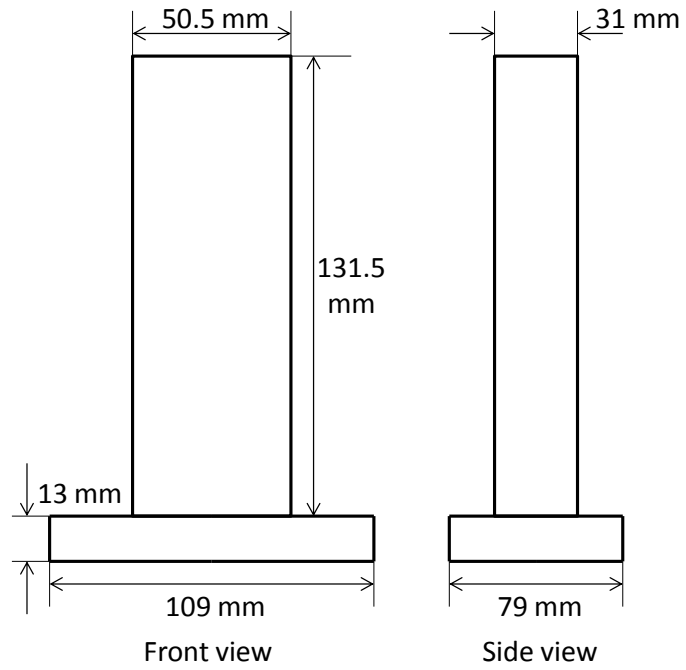
Figure 3.1: Dimensions of the solid stainless steel bar.
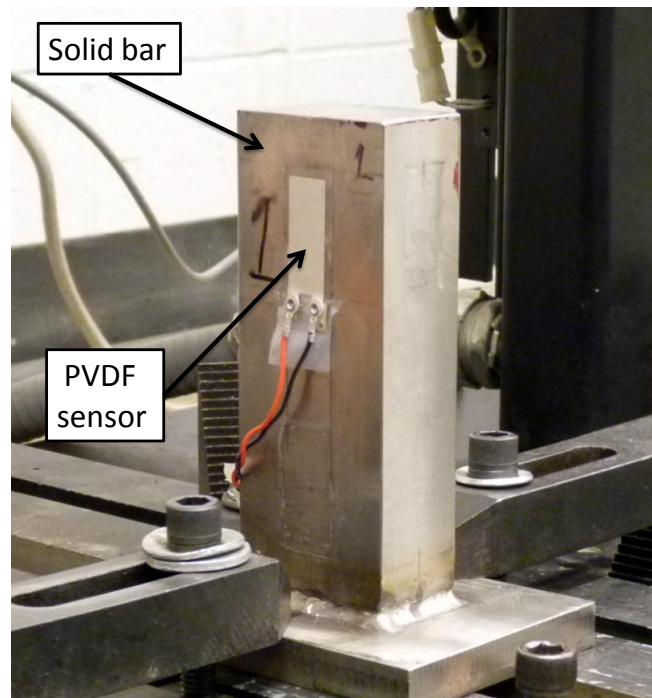
Figure 3.2: Solid bar with the PVDF sensors attached.

sensor using a brush applicator. The PVDF sensor is then pressed against the surface of the solid bar using a flat headed piece of steel block. This causes the excess glue to squeeze out from under the PVDF sensor and results in more uniform adhesion.

3.2 General experimental setup

The Instron Dynatup drop weight impact tester was used to impact the solid stainless steel bar. The bar was fixed to the base of the impact tester using four tie-down fixtures. The impact tester has an instrumented ram, or tup, attached to the bottom of the movable head weight. The tup consists of a load cell, which is bolted to the bottom of the head weight. The impactor (a flat stainless steel plate) is bolted to the bottom of the load cell. Figure 3.3 shows the impact tester and a close up of the tup resting on the top of the solid bar.

The following steps were followed for each impact test:

1. The height limit switch on the impact tester was set to a preselected drop height.
2. The movable head weight was hoisted to the drop height set by the height limit switch.
3. The head weight was then released and fell freely under gravity, onto the top of the solid bar.

The load cell measures the variation of the impact force between the flat plate impactor and the top of the solid bar, throughout the duration of impact. The Instron Impulse data acquisition system records the voltage signal from the load cell and converts it into impact force, based on the load cell's calibration factor which has to be provided to the Impulse software. The load cell's signal level itself was used as a trigger for the data acquisition, as described in detail in Chapter 2.
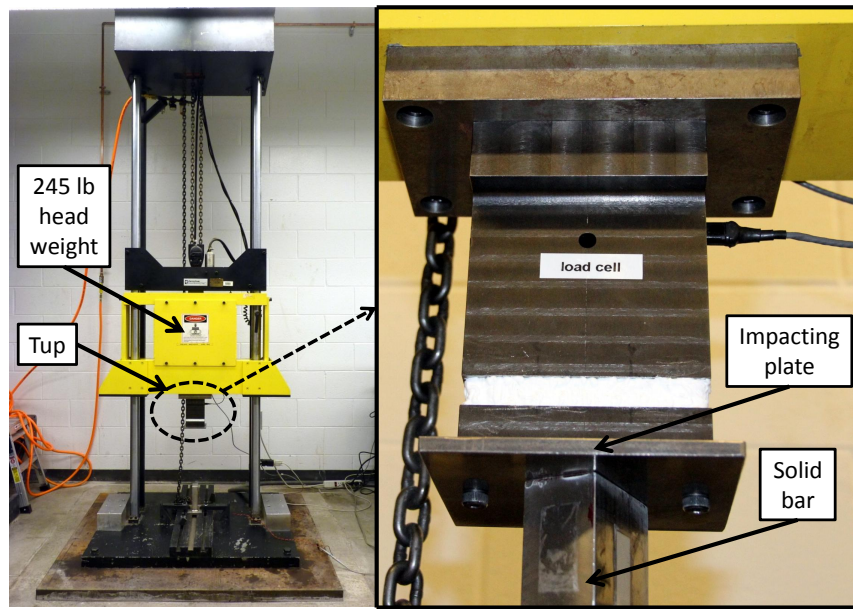
Figure 3.3: Impact tester and the instrumented ram (or tup).

The PVDF sensors are connected to the oscilloscope via 10x probes, as mentioned in the previous chapter. Thus, three sensor signals were recorded for every impact test, namely, the load cell's signal (variation of impact force with time) and the signals from the two PVDF sensors (variation of generated voltage with time). Figure 3.4 shows the complete experimental setup for the impact tests.
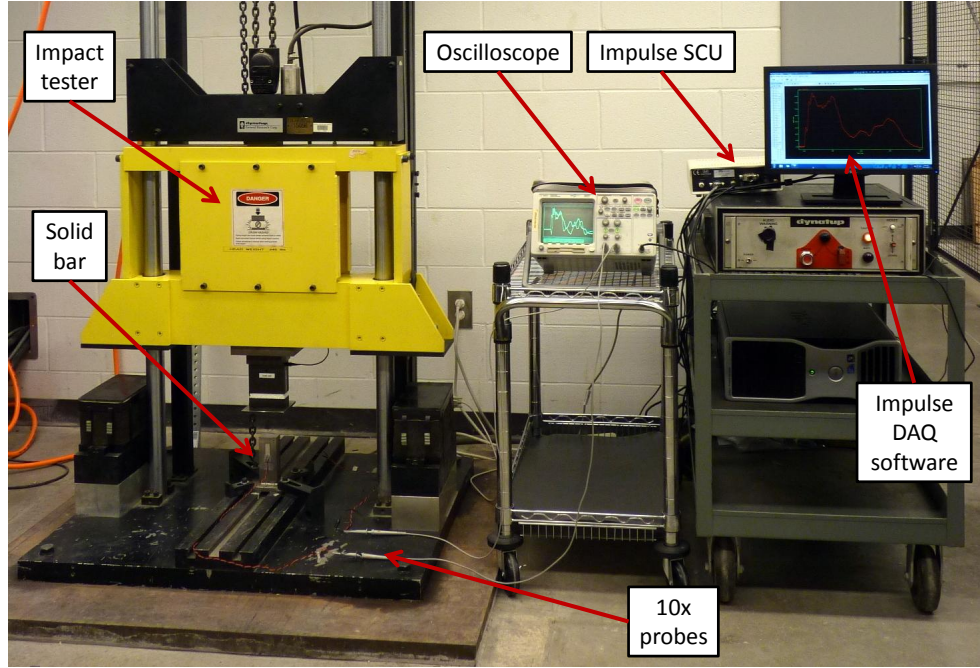
Figure 3.4: Complete experimental setup for the impact tests.

3.3 Relation between the voltage generated by the PVDF sensor and applied stress

The relationship between the voltage generated by the PVDF sensor and the stress applied to the PVDF sensor was described by (2.7) in Chapter 2. In the case of the solid bar, the magnitudes of lateral stress (T_2) and compressive stress (T_3) are small compared to the longitudinal stress (T_1). Hence (2.7) can be approximated as

$$V \approx (6.048 \times 10^{-6}) \cdot T_1. \tag{3.1}$$

Assuming that the strain acting on the solid bar gets transferred completely to the PVDF film and that at any time instant, all cross-sections across the length of the

bar experience the same longitudinal impact force, one obtains

$$T_1 \approx \sigma_b \frac{E_s}{E_b} \approx \frac{FE_s}{AE_b} \tag{3.2}$$

where σ_b is the longitudinal stress acting on the bar at the location of the PVDF sensor, F is the impact force acting on the top of the bar at any particular instant (which is recorded by the load cell), and A is the cross-sectional area of the solid bar. E_s and E_b are the Young's moduli of the PVDF film and the solid bar respectively. Using (3.2) and (3.1), one can write

$$V \approx (6.048 \times 10^{-6}) \frac{FE_s}{AE_b}. \tag{3.3}$$

Since V and F are quantities that vary with time, one can write

$$V(t) \approx \left[\frac{(6.048 \times 10^{-6})E_s}{AE_b} \right] F(t). \tag{3.4}$$

Thus, (3.4) shows that the impact force acting on the top of the solid bar is proportional to the voltage generated by the PVDF sensor.

3.4 Orientation of the bar and its influence on PVDF sensor signals

This section shows the importance of using two PVDF sensors on opposite sides instead of just one, to record the voltage response after impact.

3.4.1 Ideal impact scenario

The purpose of recording the voltage generated by a PVDF sensor attached to the solid bar is to be able to determine the longitudinal stress and impact force acting on the solid bar during impact. Consider an ideal impact experiment in which the flat impactor attached to the load cell is perfectly parallel to the flat top surface of the

solid bar. This would lead to a uniform impact force acting on the top of the solid bar, which in turn would generate longitudinal stress waves in the solid bar. Assuming that there are no non-uniformities in the material of the solid bar, the same amount of longitudinal strain would develop on each face of the solid bar at any cross-section along its length. This would lead to the generation of the same voltage signals by two PVDF sensors attached on opposite faces of the bar, at the same distance along its length.

Also, in the case of an ideal impact experiment, the impact force acting on the top of the solid bar is proportional to the voltage generated by the PVDF sensor as shown by (3.4). However, in the case of the actual experiment performed, it was seen that the voltage signals generated by PVDF sensors attached to opposite faces of the solid bar were not the same. To determine the cause of the difference in voltage signals and to investigate the influence of the orientation of the solid bar on the voltages generated by the PVDF sensors, the following experiment was conducted.

3.4.2 Varying the orientation of the solid bar

The experiment was set up using the procedure described in Section 3.2. The important features of this experiment are as follows:

- All the drop tests run under this experiment had a drop height of 3 cm.
- Two PVDF sensors are bonded to opposite sides (on the broad faces) of the solid bar. They are located at a distance of 14 mm from the top of the bar, in the center of the bar's face.
- PVDF sensors are used in 31 mode in all the tests discussed in this section.
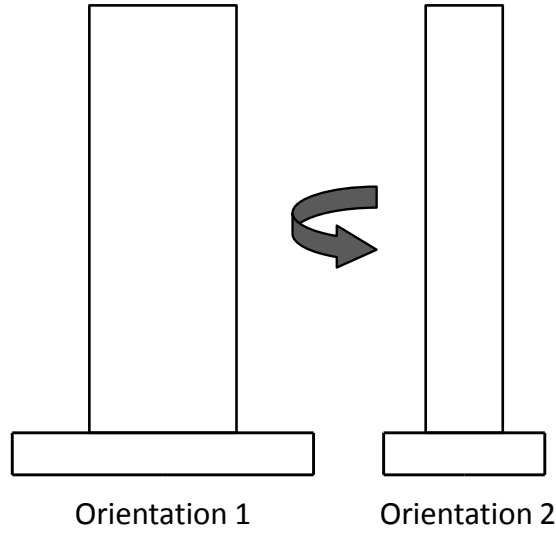
Figure 3.5: The two orientations of the solid bar used in the experiment, as seen from the front of the impact tester.

- Tests were conducted by changing the orientation of the bar (by rotating it about its vertical axis by 90 degrees) for each impact.

The two orientations of the solid bar used in this experiment are shown in Figure 3.5. In orientation 1, the broad face of the solid bar faces the front of the impact tester and in orientation 2, the narrow face of the solid bar faces the front of the impact tester.

All PVDF voltages shown in the plots in this section are generated voltages determined using the Simulink model described in Chapter 2 and have been inverted (for better comparison with load cell data). Figure 3.6 and Figure 3.7 show the generated voltage signals from the two PVDF sensors in the drop tests run using orientation 1 and orientation 2 of the solid bar respectively. It can be seen that the two PVDF sensors did not generate the same voltage signals after impact in either of the two
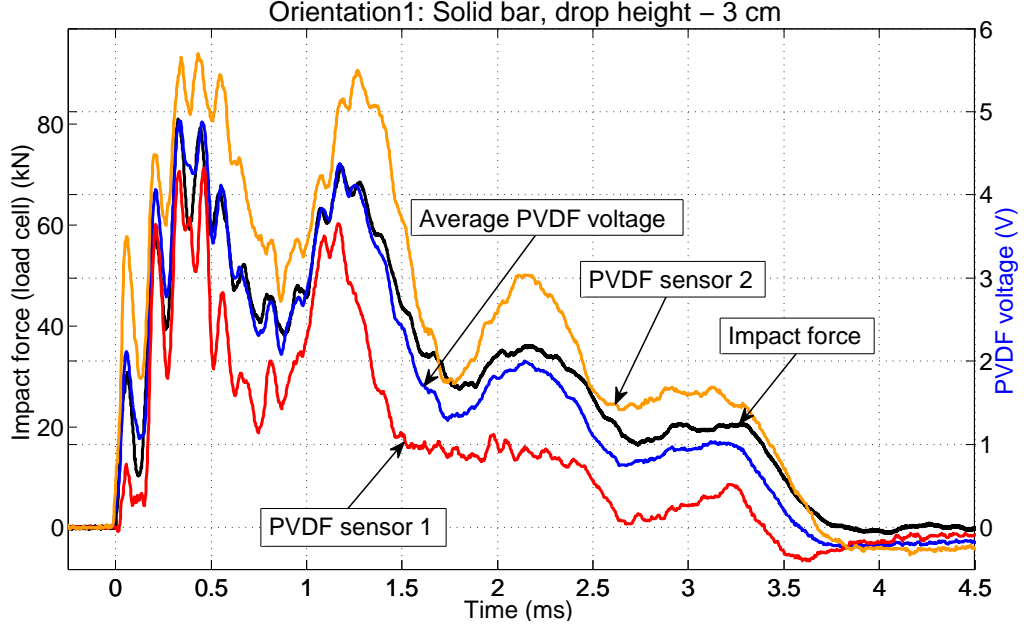
Figure 3.6: Results from orientation 1 (broad face of the solid bar facing the front).

tests. Thus, unlike in the case of an ideal impact experiment, unequal longitudinal strains were generated on opposite faces of the solid bar.

Furthermore, it can be seen from Figure 3.6 and Figure 3.7 that for both the drop tests, neither of the PVDF sensor signals appears to be proportional to the impact force recorded by the load cell (shown by the black curve). However, it can be seen that the average of the two PVDF sensor signals in both the tests can be aligned quite closely with impact force. This implies that the average of the two PVDF signals is proportional to the impact force acting on the solid bar.

Based on the above observations, it can be concluded that the impact force acting on the top of the solid bar was not distributed uniformly. This can happen if either the top of the solid bar or the impactor is not parallel to the base of the impact tester. This means that all the edges of the top of the solid bar did not hit the impactor at
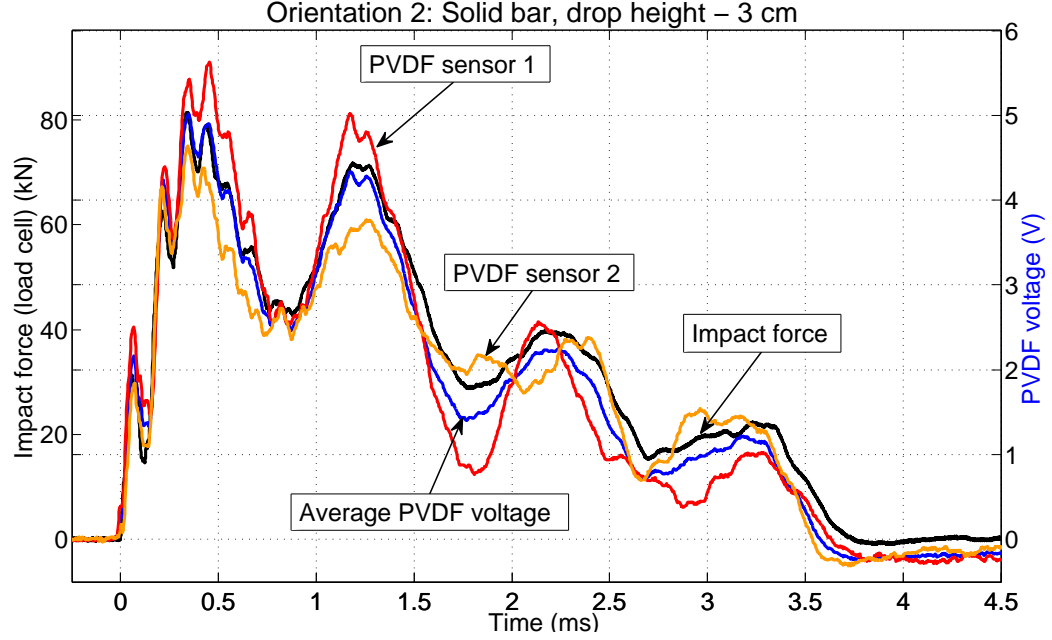
Figure 3.7: Results from orientation 2 (solid bar rotated by 90° after orientation 1).

the same time. Comparing the PVDF sensor signals in Figure 3.6 and Figure 3.7, it can be seen that the same PVDF sensor does not produce a higher voltage in both the tests.

Thus, the same edge of the solid bar did not hit the impactor first in both the tests. This implies that the impactor/drop weight is not parallel to the base of the impact tester. This is a problem that cannot be rectified easily. Hence, the solution is to use the average of both PVDF signals for comparing against the impact force and the stress predicted by the simulation.

From Figure 3.8, it can be seen that even when the orientation of the solid bar is changed, the average voltage response of the PVDF sensors does not vary significantly. The maximum voltage amplitude is almost the same in both the orientations. The most of the small amount of difference that can be seen between the two signals can
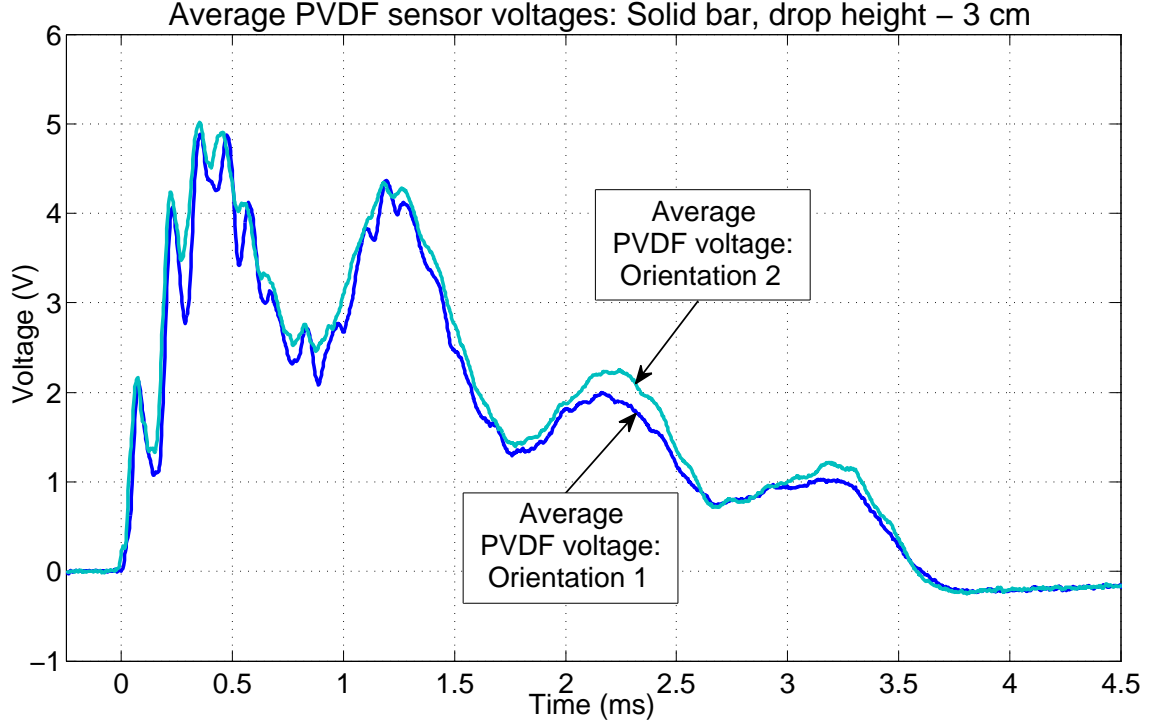
Figure 3.8: Comparison of average PVDF sensor voltages generated in the two orientations of the solid bar.

be attributed to the difference in the impact force acting on the solid bar in both the cases. This can be seen from the comparison of impact forces shown in Figure 3.9. However, it is important to note that the sensors are measuring the average stress only on two sides of the solid bar. Thus, any asymmetric stress variation along the other two sides would not be captured by the sensors. However, since the use of two sensors on opposite sides of the solid bar gives satisfactory results, this is the method that has been followed in the subsequent tests on the solid bar. Thus, based on the tests described in this section, the following conclusions can be drawn:
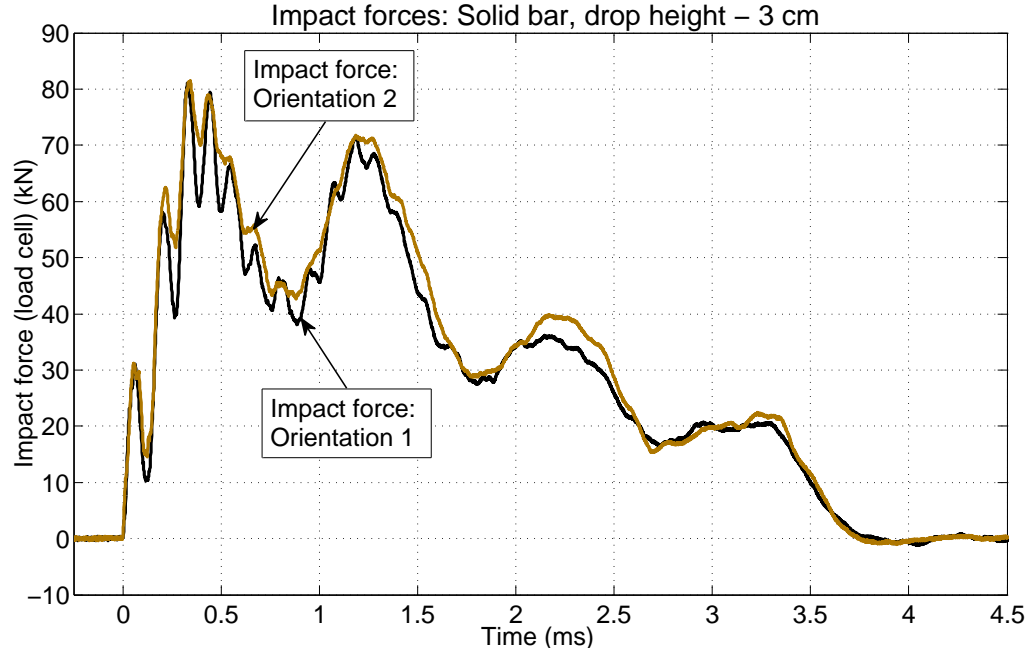
Figure 3.9: Comparison of impact forces acting on the solid bar in the two orientations.

- The orientation of the solid bar affects the voltage response of the individual PVDF sensors, but the average voltage response of the PVDF sensors is proportional to the impact force, irrespective of the orientation of the solid bar.

- The impactor/drop weight is not parallel to the base of the impact tester.

The non-parallel impact between the impacting plate and the top of the solid bar is the cause of the atypical shape of the impact force versus time curve. In the case of an ideal impact (or impact between a hemispherical impactor and the solid bar), the impact force history would show a single peak, with a smaller duration of impact.

3.5 LS-DYNA model of the impact event

Figure 3.10 shows the LS-DYNA model created to simulate the impact tests. The model was created using the preprocessing software LS-PrePost 3.2.
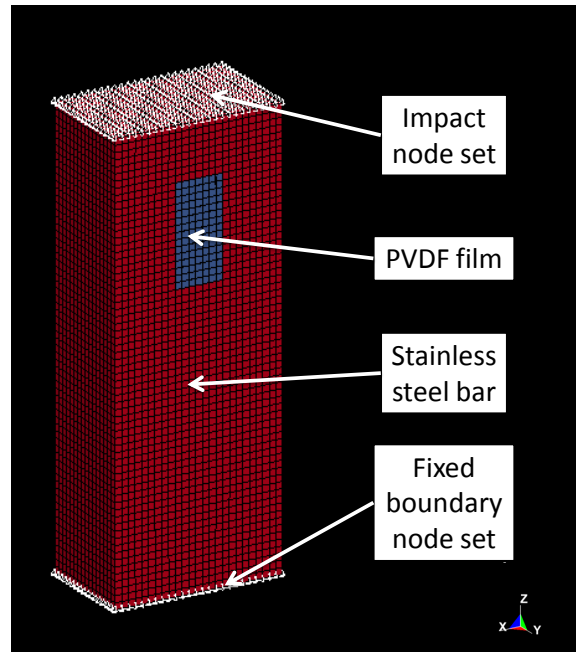
Figure 3.10: LS-DYNA model of the solid bar and the PVDF sensor.

3.5.1 General description of the model

The solid bar is modeled using the same dimensions as the actual solid bar used in the experiments. The rectangular plate welded to the actual solid bar was not modeled for the LS-DYNA simulations. The solid bar's model is made up of 26,400 elements. The elements are cubic, with sides 2 mm long. The PVDF sensor's model created for the LS-DYNA simulation, as shown in Figure 10, is 14 mm wide and 30 mm long. Its thickness is 28 μm. It is made up of 105 cubic elements, with sides 2

mm long. The models for the solid bar as well as the PVDF sensor are made up of 8-noded constant-stress solid elements (ELFORM set to Type 1). This element type is efficient and accurate [17].

The actual PVDF sensor used in the experiments had a 28 µm thick PVDF film sandwiched between two 6 µm thick silver ink electrodes. This assembly is sandwiched between two 55 µm thick Mylar sheets. The sensor is glued to the face of the solid bar. Therefore, a layer of glue exists between the Mylar sheet and the face of the solid bar. Thus, strain from the solid bar gets transferred first to the layer of glue, then to the Mylar layer, then to the silver ink layer, and finally to the PVDF film.

However, in the LS-DYNA simulations, only the 28 µm thick PVDF film has been modeled. In the experiment, the sensor is attached to the side of the solid bar at a distance of 14 mm from the top. Thus, the distance of the PVDF film from the top is 16 mm. Hence, in the LS-DYNA model, the top of the PVDF film is located at a distance of 16 mm from the top of the solid bar. Further, the PVDF sensor's model was created by generating elements on the surface of the solid bar's model. Hence, the nodes present on the interface between the PVDF sensor and the solid bar are shared by both the solid bar and the PVDF sensor. Thus, all the strain from the solid bar is transferred completely to the side of the PVDF film in contact with the solid bar.

Accurate material properties for the Mylar, silver ink, and glue layers were not available. Initially, the Mylar and silver ink layers were modeled using some typical values of their material properties. However, it was observed that the presence of the additional layers did not have a significant effect on the stress induced in the layer of the PVDF film. Hence, in the final LS-DYNA model for the tests on the solid

bar, the layers of Mylar and silver ink were not modeled. As far as the glue layer is concerned, its thickness was not known. Since it was observed that the presence of Mylar and silver ink layers did not affect the PVDF stress response, for simplicity the glue layer is not modeled either.

3.5.2 Material properties

The material model used for both the solid bar as well as the PVDF sensor is MAT 024 (MAT PIECEWISE LINEAR PLASTIC). The material properties set for the solid bar are:

- Density = 8000 kg/m^3
- Young's modulus = 193 GPa
- Poisson's ratio = 0.3
- Yield stress = 170 MPa
- Tangent modulus = 1.93 GPa

The material properties set for the PVDF film are:

- Density = 1780 kg/m^3
- Young's modulus = 3 GPa
- Poisson's ratio = 0.35
- Yield stress = 53 MPa
- Tangent modulus = 0.03 GPa

3.5.3 Boundary conditions

In the actual experiment, the base of the solid bar was clamped to the base of the impact tester. To replicate this boundary condition, displacement constraints were

applied in X, Y, and Z directions to all the nodes on the bottom of the solid bar. This is equivalent to fixing the base of the solid bar.

3.5.4 Applied load

Creating an impactor in LS-DYNA that hits the top of the solid bar with the same velocity as the impactor in the experiment leads to the application of an ideal impact force on the solid bar. This ideal impact force rises quickly to its peak value and exponentially decays after its peak. However, the impact force measured by the load cell in the experiments differs significantly from the ideal impact force shown by LS-DYNA. This leads to a significant deviation in the voltage generated by the PVDF sensor in the LS-DYNA model and the experimentally measured voltage generated by the PVDF sensor.

In order to be able to compare the simulation results and the experimental results, the impact force acting on the solid bar in the simulation must be similar to the actual impact force measured in the experiments. Hence, the force acting on the top of the solid bar, measured by the load cell during the experiment, is saved in the LS-DYNA keyword file and applied as input force to the solid bar model in the simulation. This is achieved by selecting all 442 nodes on the top of the solid bar and creating a node set. This node set is shown in Figure 10. At each time instant, the experimentally measured value of impact force is divided by 442 (number of nodes in the node set defined on the top of the solid bar) and applied to each individual node. This results in a uniform application of the measured impact force on the top of the solid bar in the LS-DYNA simulation.
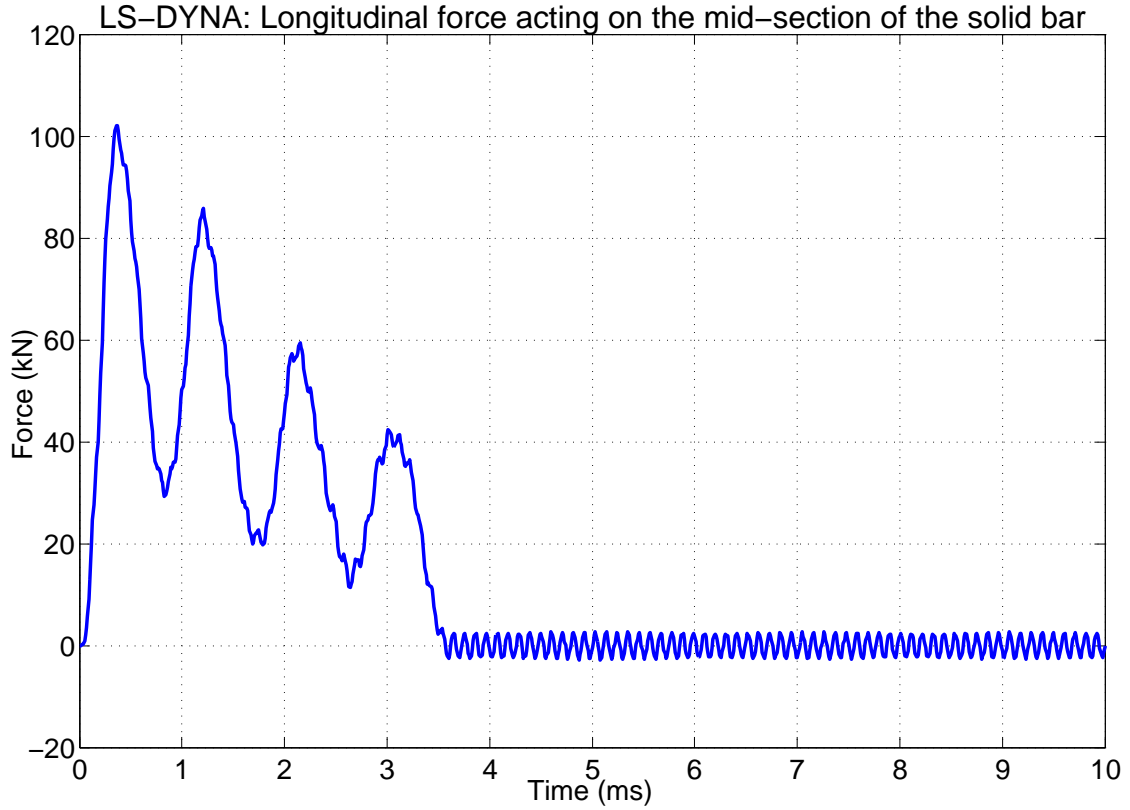
Figure 3.11: The longitudinal force acting on the mid-section of the solid bar showing undamped vibrations.

3.5.5   Damping

Initially, the LS-DYNA model was run with no damping present in the system and the longitudinal force acting on the mid-section was plotted from the simulation results as shown in Figure 3.11. The results showed cyclic changes in the magnitude of longitudinal force, without any reduction in amplitude over time. Hence, damping must be defined in the LS-DYNA model to curb these unnatural vibrations.

LS-DYNA allows the user to set a system damping constant (damping coefficient per unit mass). According to the support documentation on LSTC's website [18],

44

the value of the system damping constant must be determined by a trial and error approach. Hence, multiple trial simulations were run by varying the system damping constant and keeping all other parameters constant. The value of the system damping constant that gave the best result was 23 N-s/kg-m. At this value of the damping constant, the unnatural ringing vibrations were damped out successfully.

3.5.6 Termination time and output resolution

For studying the solid bar impact tests, the LS-DYNA model was set up to simulate the behavior of the solid bar and the PVDF sensor for a time window of 4.5 ms. This ensures that LS-DYNA predicts the behavior of the solid bar for the entire duration of impact, which was observed to be less than 4 ms. The time interval between consecutive outputs was set to 5 μs.

3.5.7 Post-processing

Figure 3.12 shows the plot of longitudinal stress (calculated by LS-DYNA) acting on the PVDF sensor from an impact simulation. To generate the plot, all the elements of the PVDF sensor were selected. Thus, each curve shown in the plot corresponds to an element of the PVDF sensor. It can be seen that there is a variation in the values of longitudinal stress acting on the PVDF sensor. For the purpose of further analysis of the impact test, the average value of longitudinal stress acting on all the elements that form the PVDF sensor was computed and used. This is also in accordance with the fact that even in the actual impact tests, the PVDF sensor's output always represents the average of the stress acting on it.
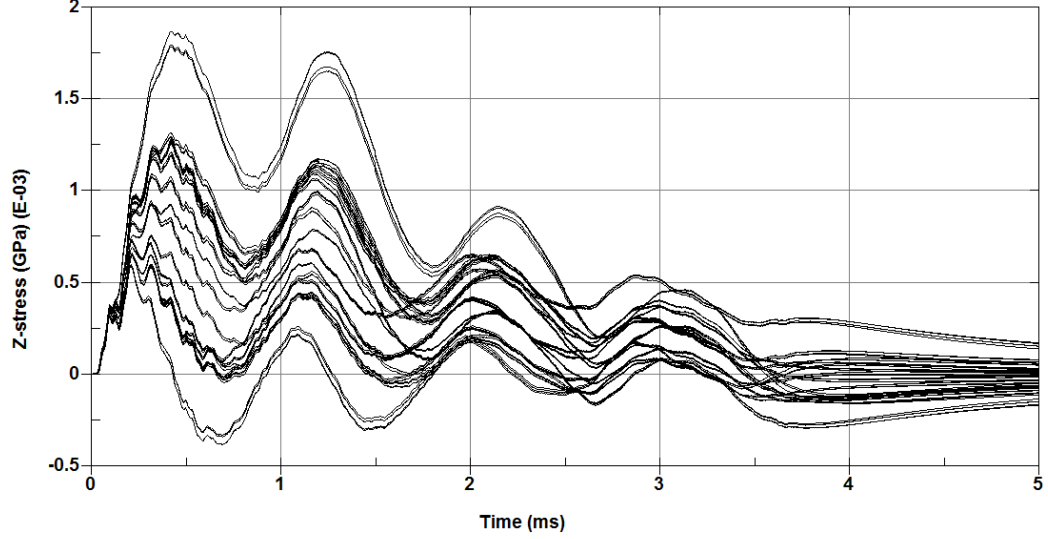
Figure 3.12: Variation of the longitudinal stress acting on the individual elements of the PVDF sensor shown by LS-DYNA.

3.6   Impact tests on the solid stainless steel bar

In this experiment, three drop tests were run on the solid bar. The head weight was dropped on the solid bar from heights of 3 cm, 5 cm, and 7 cm. The setup for this experiment was the same as the general experimental setup described earlier in this chapter. The PVDF sensors were used in the 31 mode in this experiment. As explained in the previous section, the impact force data from the load cell was fed to the LS-DYNA model as applied load for the solid bar. The frequency at which the PVDF and load cell signals were recorded was 1 MHz and 546 kHz respectively. For each of the three drop tests, the following steps were followed:

1. For each time instant, the longitudinal stress (Z stress), acting on all the elements of the PVDF sensor's model in LS-DYNA was averaged. This was done

46

for the entire duration of the impact event in order to obtain the average stress acting on the PVDF sensor during impact.

2. This was further converted into the voltage generated by the PVDF sensor, using (3.1). Thus, one obtains a time history of the expected voltage generated by the PVDF sensor based on the results of the simulation.

3. This time history of expected voltage generated by the PVDF sensor was then compared against the impact force measured by the load cell, and the average generated PVDF sensors' voltage measured experimentally.

Note that all the plots in this section show the generated average value of the PVDF sensor's voltage and not the voltage that was directly measured by the oscilloscope. This experiment had the following objectives:

1. To check the validity of the simplified linear piezoelectric equation for 31 mode, in the form of (3.1).

2. To check the accuracy of the LS-DYNA model used to simulate the impact event.

3. To investigate if a proportionality constant can be calculated for this experiment, which can be used to determine the impact force acting on the solid bar.

4. To develop and validate the experimental method for conducting impact tests using PVDF sensors bonded to structures. This includes the method of bonding the sensor to the structure, selection and setting up of data acquisition system for the PVDF sensors, setting up the Impulse DAQ software for the load cell, and determination of the generated voltage from the measured voltage.

This is why a simple geometry was chosen for the structure under impact. The simple geometry helps to focus on the objectives defined above and minimizes errors due to imperfections and geometric complexities in the structure.

3.6.1 Results and analysis

Figure 3.13 shows the comparison of the impact force measured by the load cell, the average PVDF sensor generated voltage, and expected PVDF sensor voltage calculated using the LS-DYNA simulations results, for the 3 cm drop test.
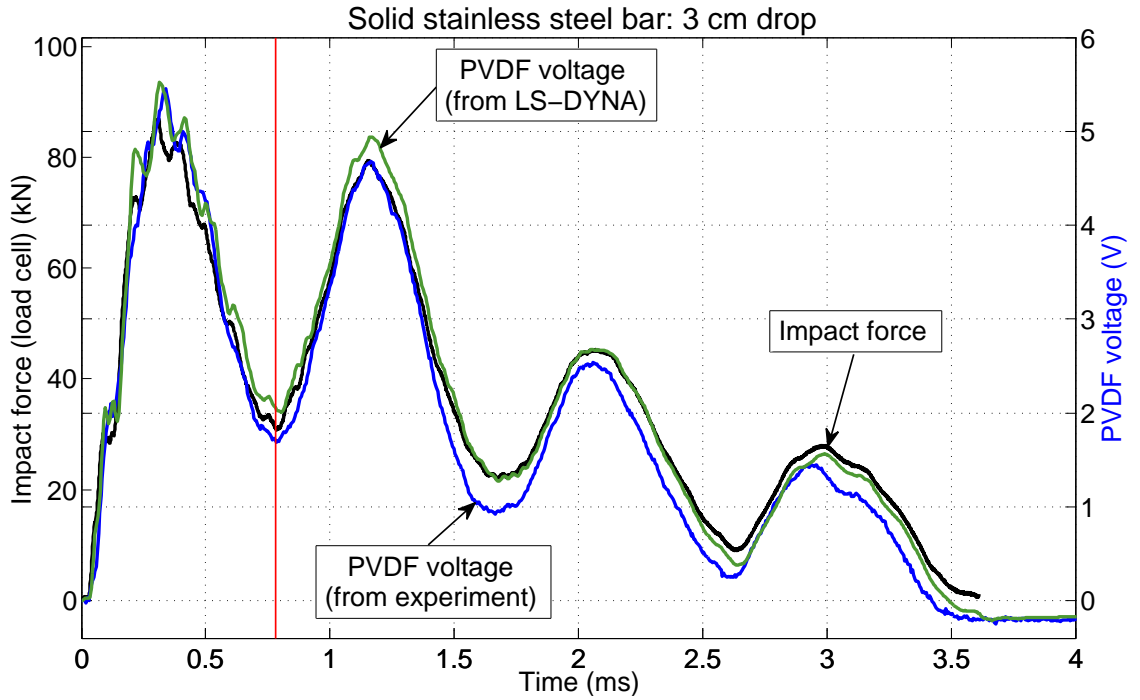
Figure 3.13: Impact force, average PVDF sensor voltage from experiments, and expected PVDF sensor voltage calculated using LS-DYNA for the 3 cm drop test on the solid bar.

Two separate Y axes have been shown in the figure. The Y axis on the left corresponds to the impact force history and the Y axis on the right corresponds to the generated PVDF sensor voltage as well as the expected PVDF sensor voltage. The proportionality constant (described later in this section) calculated using the generated PVDF sensor voltage and the impact force was used to scale the two Y axes. The average PVDF voltage signal does not have the same start time as the load cells impact force signal. For easier comparison of the impact force and PVDF voltage, the load cells signal was aligned with the average PVDF sensors signal. This was achieved by using the following method:

1. The mean signal levels of the average PVDF voltage and the impact force, before impact, were set to zero.

2. A moving average with a span of three elements was used to smooth the signals.

3. The difference between the time instant at which the force starts rising above zero and the time instant at which the average PVDF voltage starts rising above zero was found and subtracted from the impact force signal.

The following steps were followed to calculate the proportionality constant between the impact force and the PVDF voltage:

1. The signals shown in Figure 3.13 display four distinct spikes. The load cell and experimental PVDF data for the entire duration of the first spike, which starts at 0 ms and ends at 0.78 ms, was selected. This is the time window that lies before the vertical red line shown on Figure 3.13.

2. The mean values of the impact force F_{mean} and the generated PVDF voltage V_{mean}, in the time window specified above, are calculated.

3. The proportionality constant k (or impact force sensitivity) is calculated by determining the ratio of the mean PVDF voltage to the mean impact force.

Therefore, $k = V_{mean}/F_{mean}$ in the range specified. It is emphasized that the proportionality factor depends upon the structure under impact, the properties of the PVDF sensor attached to it, and the position of the sensor relative to the direction of impact. Thus, k is a property of the structure with the PVDF sensor attached to it. The maximum value of the impact force, which occurs at the peak of the first spike in the signals, is the most important for the purpose of detection of impact. When the proportionality constant was calculated using only the peak values of the generated PVDF sensor voltage and the impact force and was used to scale the two Y axes in Figure 3.13, it causes misalignment of the remaining parts of the signals. At the same time, using the entire duration of impact for calculating the proportionality constant causes significant misalignment of the signals at their peak values. Hence, the entire duration of the first spike was chosen for calculation of k. This helps avoid large misalignments at the peak values of the signals, as well as at the remaining three spikes.
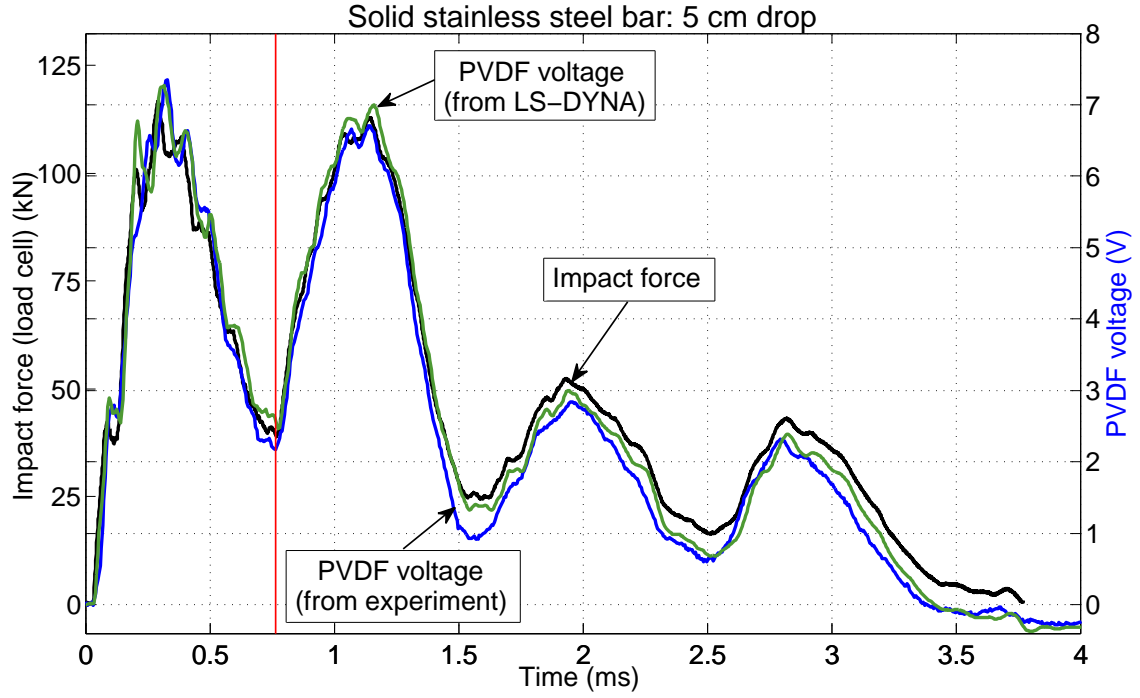
Figure 3.14: Impact force, average PVDF sensor voltage from experiments, and expected PVDF sensor voltage calculated using LS-DYNA for the 5 cm drop test on the solid bar.

The above analysis was repeated for the 5 cm drop test and the 7 cm drop test. Figure 3.14 and Figure 3.15 show the comparison of the impact force measured by the load cell, the average PVDF sensor generated voltage and expected PVDF sensor voltage calculated using the LS-DYNA simulations results for the 5 cm and 7 cm drop tests respectively.
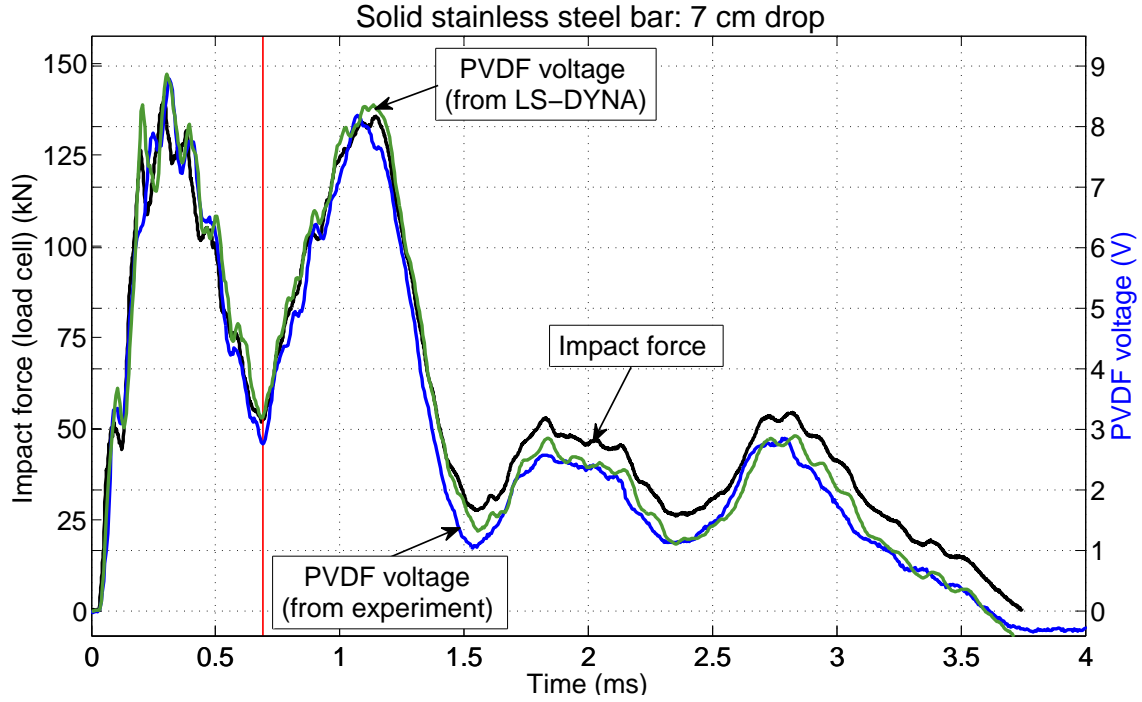
Figure 3.15: Impact force, average PVDF sensor voltage from experiments, and expected PVDF sensor voltage calculated using LS-DYNA for the 7 cm drop test on the solid bar.

Table 3.1 summarizes the results of all three impact tests. The average proportionality factor for the three drop tests is 0.059 V/kN.

Parameter	Test 1	Test 2	Test 3
Drop height (cm)	3	5	7
Peak average generated PVDF voltage (from the experiment) (V)	5.46	7.35	8.79
Peak expected PVDF voltage (from the simulation) (V)	5.52	7.27	8.86
% difference between the peak PVDF voltage from the experiment and from the simulation	1.1	1.1	0.8
Peak impact force (kN)	86.95	116.75	140.95
Proportionality constant k (V/kN)	0.059	0.060	0.059

Table 3.1: Summary of the results from the impact tests on the solid bar.

3.7 Conclusions

- The results show that there is a strong correlation between the generated PVDF voltage (from the experiment) and the expected PVDF voltage calculated using the results of the LS-DYNA simulations. Thus, it can be concluded that the LS-DYNA model created to simulate the impact is accurate to an acceptable extent and can be used as a template for creating the LS-DYNA model for simulating impact tests on more complex structures such as a hollow beam, which is the next stage of this work.

- The proportionality constants calculated for the three drop tests have closely spaced values. This implies that the average value of k (0.059 V/kN) and the voltage generated by the PVDF sensor in 31 mode, can be used to determine the impact force acting on the solid stainless steel bar used in this experiment.

- The close alignment of the generated PVDF voltage and the impact force shows that the assumption that they are proportional to each other is reasonable and

validates the use of the simplified linear piezoelectric equation for 31 mode, namely (3.1).

- The PVDF sensors did not get detached from the solid bar during the impact tests. The data acquisition systems consisting of both the Agilent 54622A oscilloscope and the Impulse DAQ system were able to capture the complete impact events at high sampling rates. This indicates that the triggering system and sampling frequency of the DAQ systems were set up correctly. In addition, the close match between the generated PVDF voltage and the simulation based PVDF voltage also indicates that the model used for the determination of the measured PVDF voltage is accurate to an acceptable extent. These observations validate the experimental method developed for conducting impact tests using PVDF sensors bonded to structures.

Chapter 4: PVDF SENSORS ATTACHED TO A HOLLOW STEEL BEAM

This chapter builds on the impact test methodology explained in the Chapter 2 by extending it to a more complex structure, namely, a hollow steel beam. Based on a discussion of the results, it is shown that the PVDF sensor can be used determine the impact force acting on a structure. In addition, the LS-DYNA model created for these tests is explained in detail and evaluated by comparing it to the experimental results.

4.1 Hollow steel beam

Hollow steel beams were used for the impact tests discussed in this chapter. Figure 4.1 shows the picture of one of the beams, with the PVDF sensors attached. Each beam was made by spot welding two parts, made of 1.42 mm thick steel (JAC270C). These two parts were spot welded along their length, on both sides. Each spot weld had a diameter of approximately 5 mm and the typical spacing between adjacent spot welds was 40 mm. A square base plate of the same material was welded to the bottom of each beam. The base plate provides a surface for the fixtures to hold the beam in its place during impact. Each beam had a height of 400 mm (measured from the top of the beam to the base plate, not including the thickness of the base plate). The
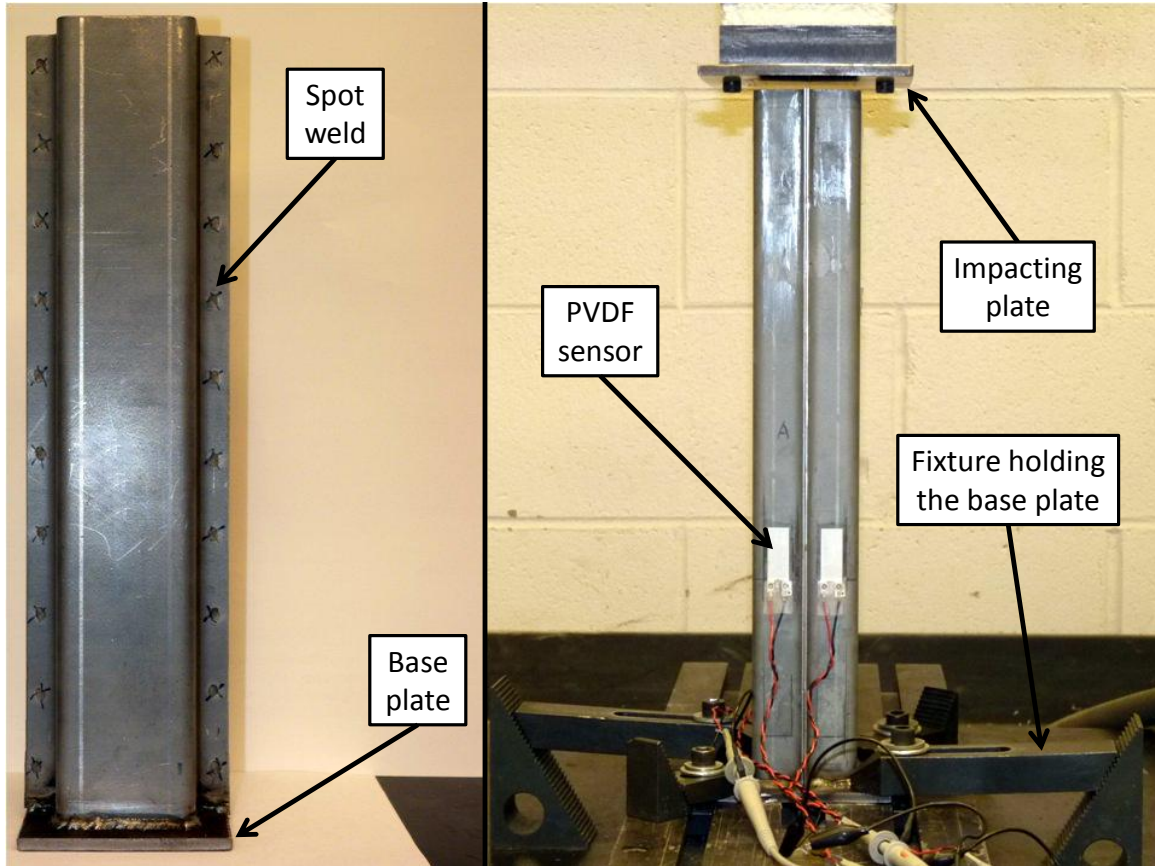
Figure 4.1: One of the hollow beams on the left and the experimental setup with the PVDF sensors attached to the beam on the right.

dimensions of the cross section of the beams have been shown in Figure 4.2. The base plate had a side length of 100 mm and was 5 mm thick. There was a small variation in dimensions between the different beams tested. In Chapter 2 it was shown that the impactor/drop weight is not perfectly parallel to the base of the impact tester. Hence, the average voltage from four PVDF sensors bonded to the sides was used for comparing against the impact force. Four PVDF sensors were attached, lengthwise (and thus, in 31 mode), to the middle of the sides of each beam used in the impact tests. The positions of the sensors have been shown in the top view of the beam in

56

Cross section of a hollow steel beam
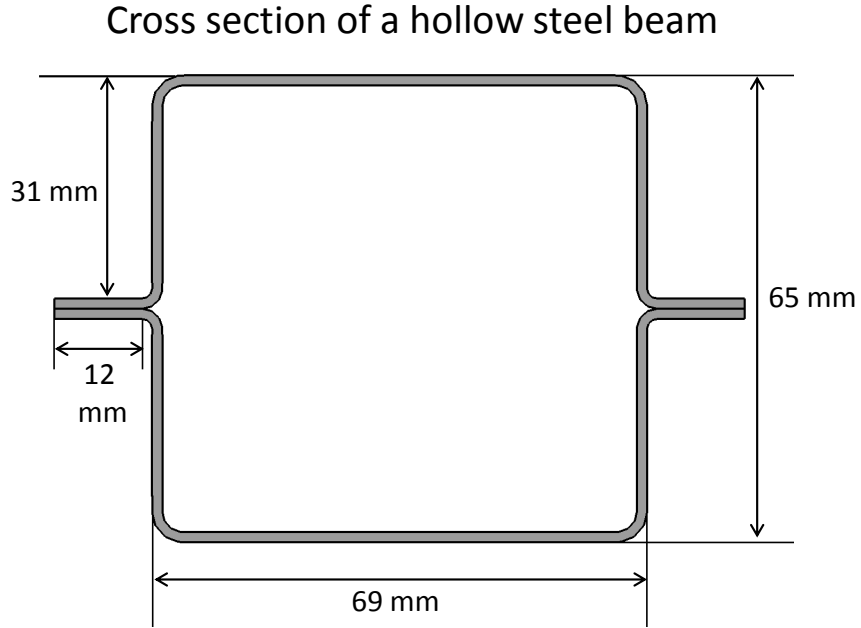
Figure 4.2: Dimensions of the cross section of the hollow steel beam.

Figure 4.3. Note that the thickness of the sensors has been highly exaggerated in the figure. The sides bearing the ridges were chosen for attaching the sensors because they are relatively stiff compared to the other two sides of the beam without the ridges. This helps avoid the measurement of bulging modes of the beam and ensures that the stress detected by the sensors is predominantly longitudinal. The lower end of the PVDF film in each sensor is at a distance of 120 mm from the base plate. This distance ensures that the PVDF sensors are away from the heat affected zone close to the bottom of the beam, where the base plate was welded. It also ensures that the PVDF sensors will not be in the zone of deformation in destructive tests on the beam. Figure 4.4 shows the variation of longitudinal stress along the length of the beam after impact, at four different time instants. The data shown in the
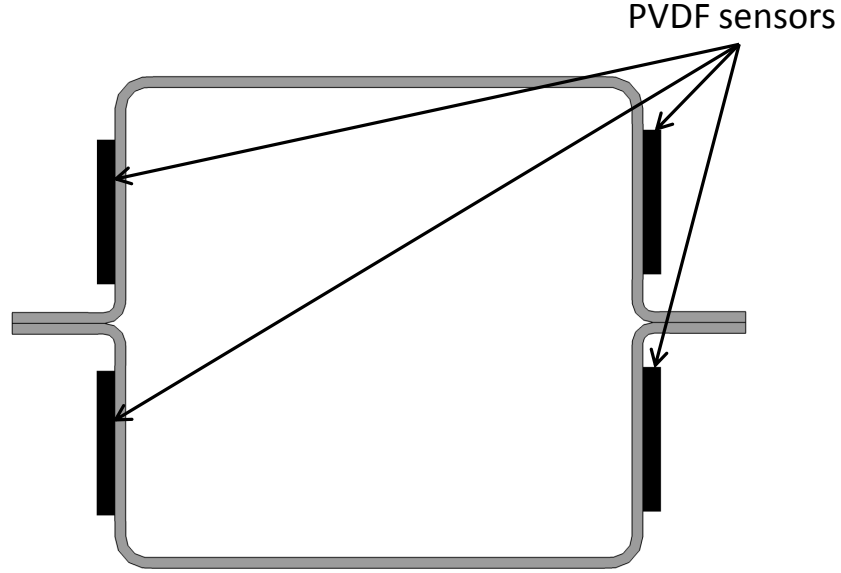
Figure 4.3: Top view of the beam showing the positions of the four PVDF sensors.

figure was taken from the results of an LS-DYNA simulation of an impact test. The impact force on the top of the beam reaches its peak between 1.26 ms and 1.5 ms in this simulation. The details of the LS-DYNA model used have been provided later in this chapter. From Figure 4.4, it can be seen that the longitudinal stress does not vary significantly along the zone from 120 mm to 150 mm from the bottom of the beam, which is where the PVDF films in the sensors are located. Thus, based on the LS-DYNA simulation, it appears that the stress acting along the length of the PVDF films does not vary significantly at specific time instants during impact. Commercially available cyanoacrylate glue (Krazy glue) was used for bonding the PVDF sensors to the surface of the beams. The procedure for attaching the PVDF sensors to the beam is the same as the one described in Chapter 3.
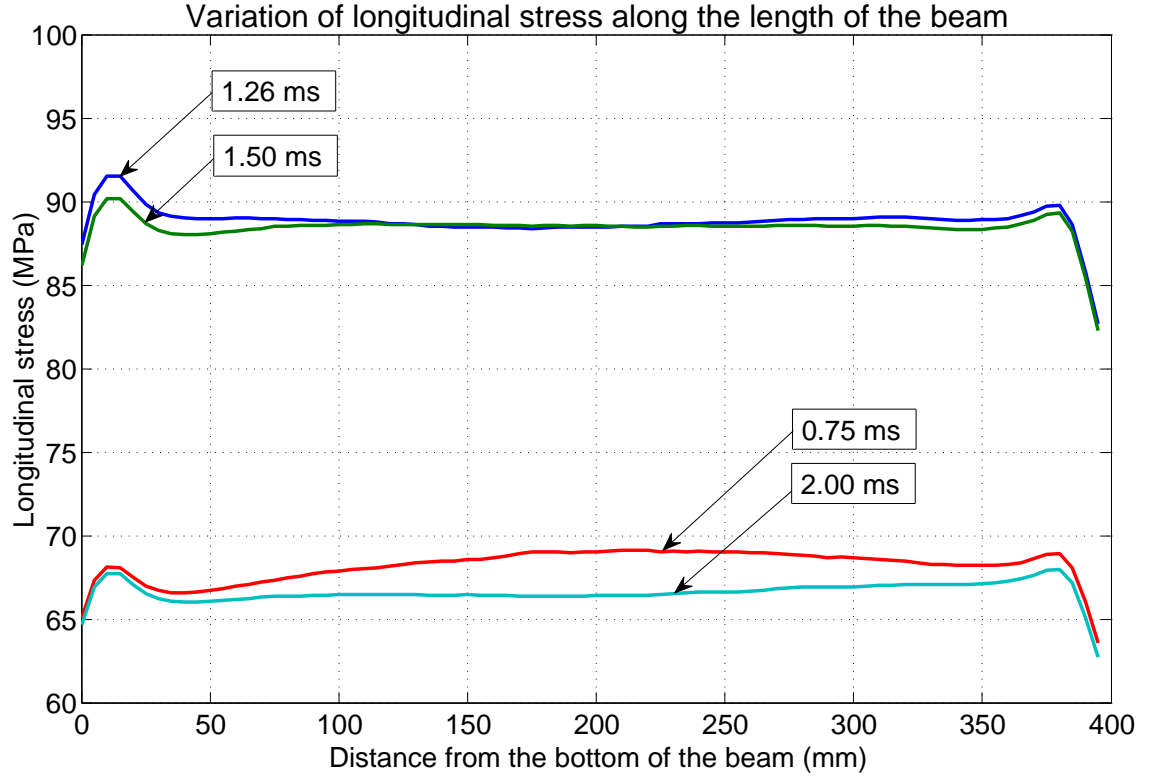
Figure 4.4: Variation of longitudinal stress along the length of the beam after impact, at four different time instants.

In the case of the hollow steel beams, the out-of-plane stress acting on the PVDF sensor (compressive stress T_3), caused by impact, has a very small magnitude compared to the longitudinal stress (T_1) and lateral stress (T_2) acting on the sensor. Hence, using (2.7) and neglecting T_3, one can write

$$V = (6.048 \times 10^{-6}) \cdot T_1 + (0.528 \times 10^{-6}) \cdot T_2. \tag{4.1}$$

4.2   Experimental setup

Each hollow steel beam used for impact was fixed to the base of the impact tester using four tie-down fixtures. As in the case of the solid bar, a flat stainless steel plate attached to the load cell was used as the impactor. The method followed for the impact tests is the same as mentioned in Section 3.3 in Chapter 3. Since data from four sensors was required, two oscilloscopes (Agilent 54622A) were used, each having two channels. Each PVDF sensor was connected to an oscilloscope using a 10x probe. Thus, five sensor signals were recorded for every impact test, namely, the load cell's signal (variation of impact force with time) and the signals from the four PVDF sensors (variation of generated voltage with time). The load cell's signal level was used as a trigger for the data acquisition, as described in detail in Chapter 2.

Two types of impact tests were performed using the hollow steel beams; the non-destructive tests and the destructive tests. The non-destructive tests involved impact from low drop heights, to ensure that the beam being impacted does not permanently deform significantly. In contrast, the destructive tests involved the use of high drop heights and additional drop weights so as to cause significant permanent deformation of the beam. The frequency at which the PVDF signals were recorded was 4 MHz for the non-destructive tests and 10 MHz for the destructive tests. The load cell's signal was recorded at 546 kHz for the non-destructive tests and at 164 kHz for the destructive tests.

4.3   LS-DYNA model of the impact event

Figure 4.5 shows the LS-DYNA model created to simulate the impact tests on the hollow steel beams.
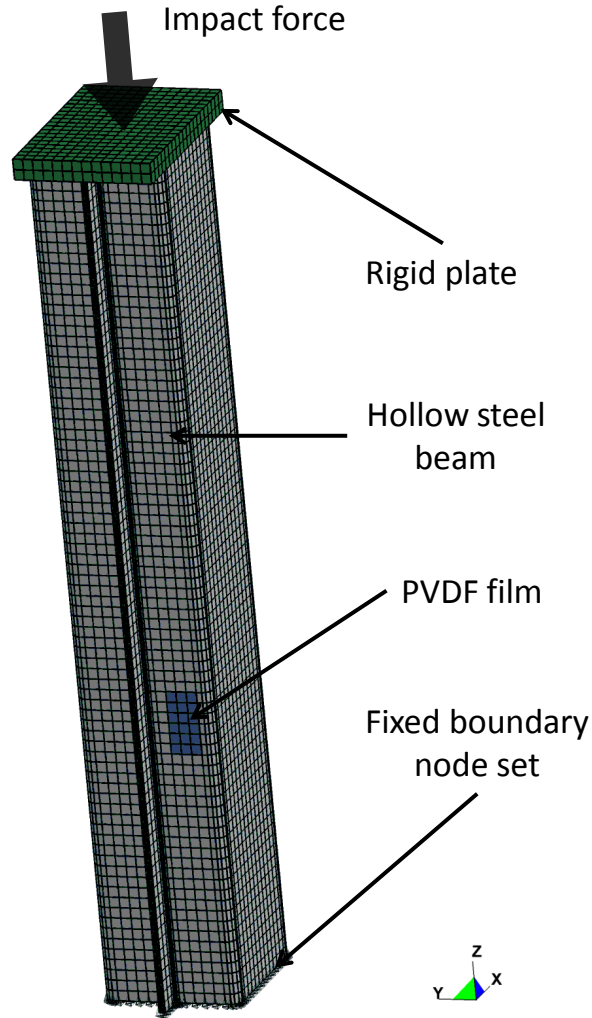
Figure 4.5: LS-DYNA model of the hollow beam, PVDF film, and rigid plate.

4.3.1 General description of the model

The hollow beam is modeled using the same dimensions as the actual beams used in the experiments. The base plate welded to the actual beams was not modeled for the LS-DYNA simulations. The LS-DYNA model consists of four separate parts, namely, a rigid plate that exerts a prescribed impact force on the beam, the two halves

of the beam's body that are spot welded to each other, and the PVDF film. All the parts have been modeled using 8-noded constant-stress solid elements (ELFORM set to Type 1) since this element type is efficient and accurate [17]. The elements are cubic, with sides 5 mm long.

The purpose of the rectangular rigid plate is to transfer a prescribed impact force to the top of the hollow beam. The dimensions of the plate are 98 mm x 66 mm, corresponding to the dimensions of the flat rectangular impactor attached to the load cell. The rigid plate is in contact with the top of the hollow beam, but is not fixed to the beam.

Each of the beam's two halves is made up of 7520 elements. The PVDF film is made up of 18 elements and the rigid plate consists of 560 elements. The PVDF film's model was created in the same way as described in Section 3.5.1 in the previous chapter, on the surface of the beam's model. Hence, all the strain acting on the elements of the beam under the PVDF film gets transferred completely to the PVDF film.

Figure 4.6 shows one of the two halves of the hollow beam's model. These two parts were placed in contact with each other and were then joined to each other by defining spot welds along their sides. These spot welds can be seen as a series of twenty small white circles in Figure 4.6. Each spot weld shown corresponds to a spot weld present on the actual hollow beams. There is a small amount of variation in the exact locations of the spot welds on the actual beams and in the model. This is because the spot welds present on the actual beams do not have a constant separation between them and their locations also differ slightly from one beam to another. In
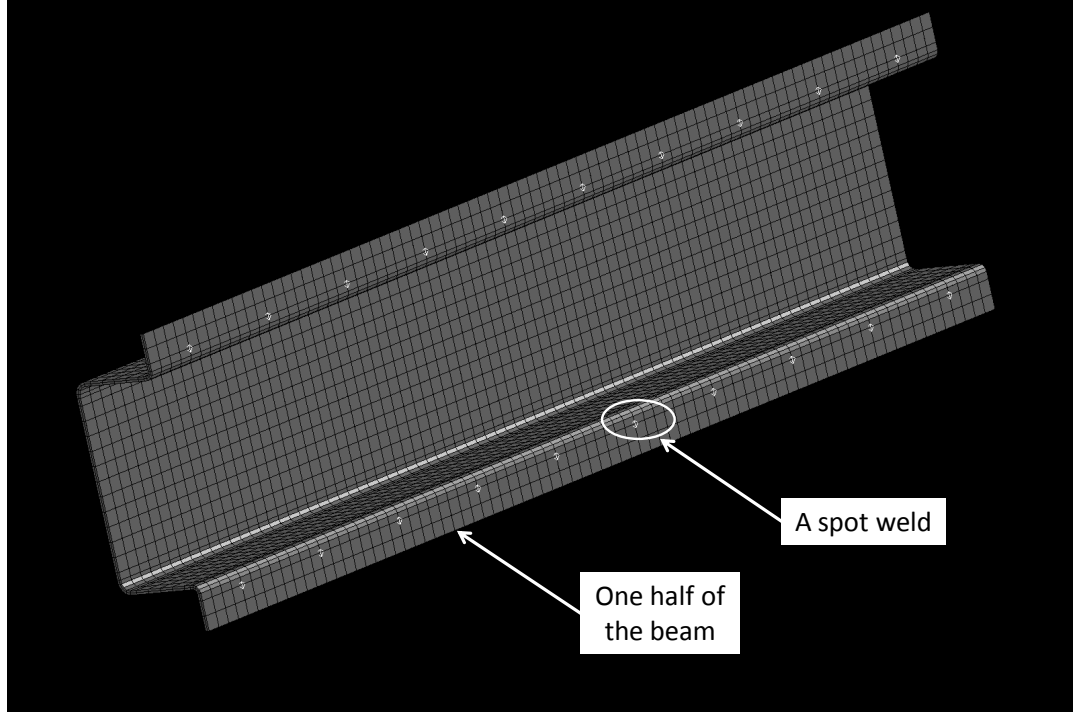
Figure 4.6: Picture showing one of the two halves that form the hollow beam in the LS-DYNA model. One of the spot welds has been highlighted.

the LS-DYNA model, at the location of each spot weld, the nodes belonging to the two halves of the beam are tied to each other.

4.3.2 Material properties

The material model used for the hollow beam and the PVDF sensor is MAT 024 (MAT PIECEWISE LINEAR PLASTIC). The material model used for the rigid plate is MAT 020 (MAT RIGID). The material properties set for the hollow steel beam are:

- Density = 7800 kg/m^3

- Young's modulus = 190 GPa

- Poisson's ratio = 0.3

- Yield stress = 260 MPa

- Tangent modulus = 425 MPa

The material properties set for the PVDF film are:

- Density = 1780 kg/m^3

- Young's modulus = 3 GPa

- Poisson's ratio = 0.35

- Yield stress = 53 MPa

- Tangent modulus = 0.03 GPa

The material properties set for the 316 L stainless steel rigid plate are:

- Density = 8000 kg/m^3

- Young's modulus = 193 GPa

- Poisson's ratio = 0.3

4.3.3 Boundary conditions

In the actual experiment, the base of the hollow beams was clamped to the base of the impact tester. To replicate this boundary condition, displacement constraints were applied in X, Y, and Z directions to all the nodes at the bottom of the two halves of the hollow beam in the LS-DYNA model. This is equivalent to fixing the base of the hollow beam.

4.3.4 Applied load

The force acting on the top of the hollow beam, measured by the load cell during the experiment, is saved in the LS-DYNA keyword file and applied as the input force to the hollow beam's model in the simulation. As shown in Figure 4.5, the measured

impact force is applied at the center of the rigid plate. This results in a uniform application of the impact force on the top of the hollow beam.

4.3.5   Damping

A trial and error approach was used for determining the most suitable system damping constant. The reasons for this have been discussed in Section 3.5.5. The value of the system damping constant that gave the best result was 5 N-s/kg-m.

4.3.6   Termination time and output resolution

The termination time was set to 5.5 ms for the non-destructive tests and 23 ms for the destructive tests. This ensures that the behavior of the hollow beam and the PVDF film is simulated for the entire duration of impact. The time interval between consecutive outputs was set to $15\,\mu s$.

4.3.7   Post-processing

The method followed for determining the average longitudinal and lateral stress acting on the PVDF film is the same as the one described in Section 3.5.7. From the LS-DYNA simulations of the impact tests, it was observed that the average Y stress acting on the PVDF sensor was about 19 times lower than the average Z stress on the PVDF sensor. This makes the average Y stress small, but not insignificant, compared to the average Z stress. However, from (4.1) it can be seen that the contribution of average Z stress to the total voltage generated by the PVDF sensor (which is given by $(6.048 \times 10^{-6}) \cdot T_1$) is more than 217 times higher than the contribution of average Y stress (which is given by $(0.528 \times 10^{-6}) \cdot T_2$). This can be seen clearly in Figure
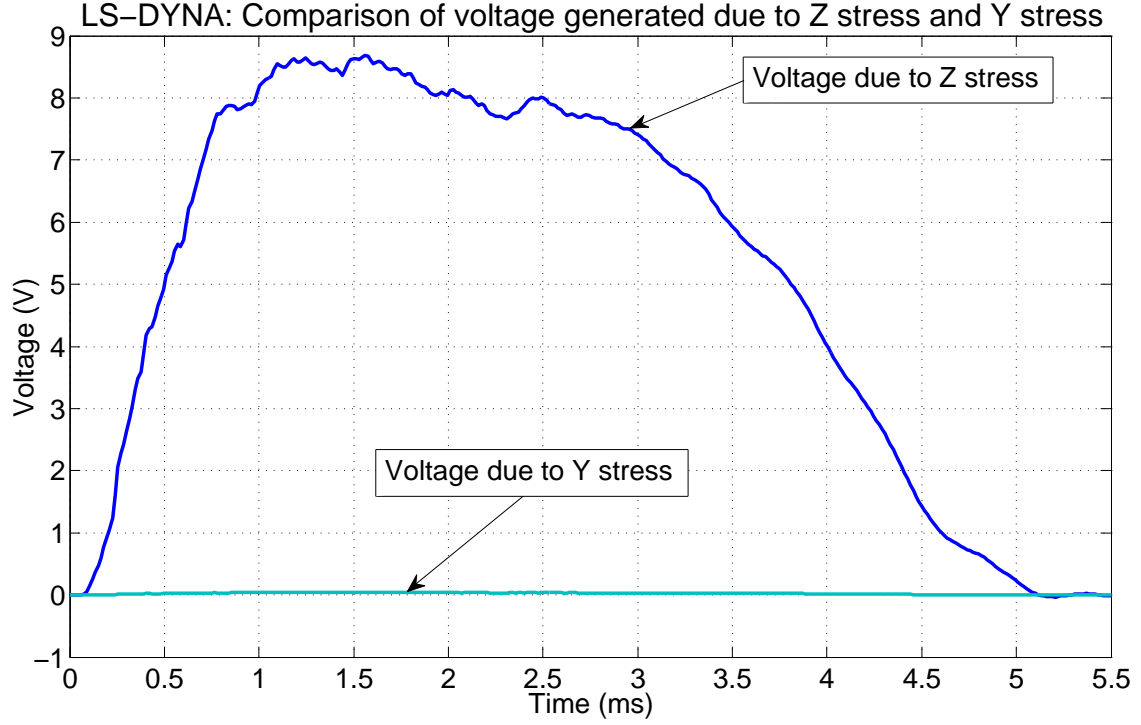
Figure 4.7: Comparison of voltages generated by Z stress and Y stress acting on the PVDF sensor.

4.7, which shows the results from the LS-DYNA simulation corresponding to a non-destructive impact test using a drop height of 3 cm. Hence, the average Y stress acting on the PVDF sensor can be ignored for the purpose of calculating the voltage generated by the PVDF sensor using the results of the LS-DYNA simulations. Thus, (4.1) can be rewritten as

$$V = (6.048 \times 10^{-6}) \cdot T_1. \tag{4.2}$$

4.4 Non-destructive impact tests on a hollow steel beam

The purpose of the non-destructive impact tests was to determine a proportionality constant or sensitivity factor which would later be used for converting the voltage generated by the PVDF sensors during the destructive impact tests into impact force acting on the beam.
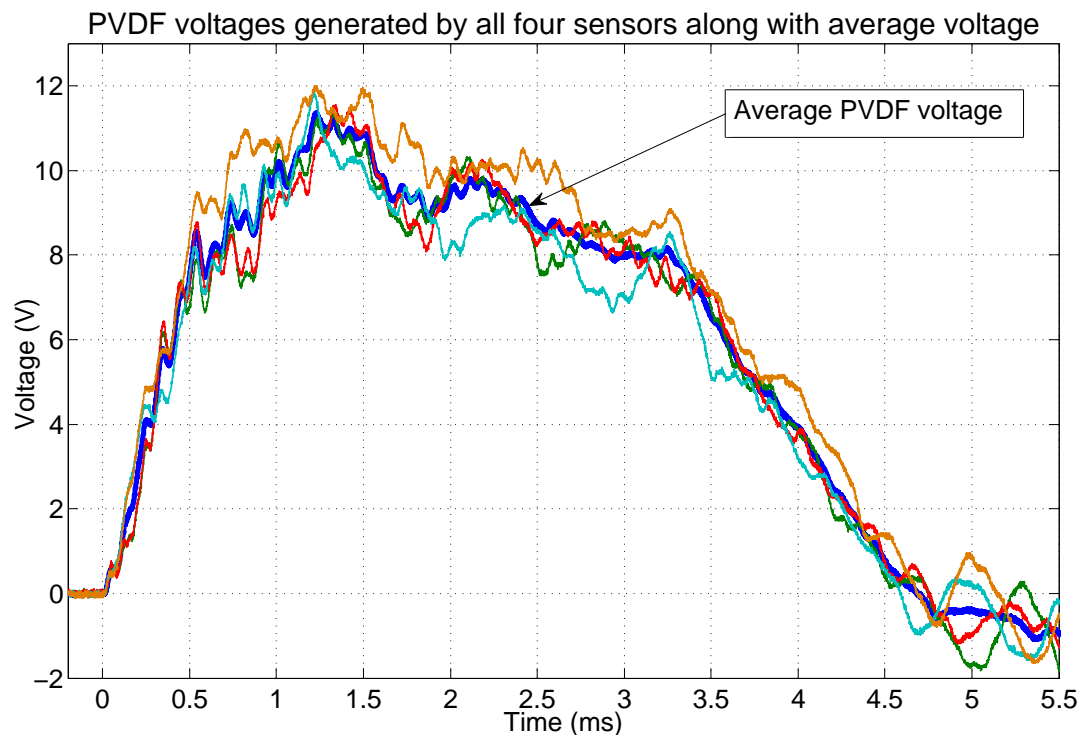
Figure 4.8: All four PVDF sensor generated voltages (shown by thin curves) and the average generated voltage (shown by the thick curve) from the non-destructive test on beam N (3 cm drop height).

In this experiment, four drop tests were performed on a hollow steel beam. This beam used for non-destructive tests has been referred to as beam N in the rest of the chapter. The head weight was dropped on beam N from heights of 0.5 cm, 1

cm, 1.5 cm, and 3 cm, in that order. The first three impact tests did not produce any deformation in the beam. Beam N was deformed by a small amount near its top during the drop test from 3 cm. The impact force data from the load cell was provided as the input force to the rigid plate in the LS-DYNA model as described in the previous section.

As mentioned earlier in this chapter, voltages from four PVDF sensors were recorded and their average was used for comparison with impact force. Figure 4.8 shows the typical variation of all four PVDF sensor generated voltages and the average generated voltage. The signals shown in Figure 4.8 are from the non-destructive test on beam N using a drop height of 3 cm

The average PVDF voltage signal does not have the same start time as the load cell's impact force signal. In order to facilitate better comparison of the impact force and PVDF voltage, the load cell's signal was aligned with the average PVDF sensors' signal. This was achieved by using the following method:

1. The mean signal levels of the average PVDF voltage and the impact force, before impact, were set to zero.

2. A moving average with a span of ten elements was used to smooth the raw average PVDF signal, while a moving average with a span of three elements was used to smooth the load cell's signal. This filters out some of the noise in the signals and makes it easier to detect the time instant at which the signal levels cross zero. A greater span was used for the PVDF signal because it was recorded at a higher frequency compared to the load cell.

3. The difference between the time instant at which the force starts rising above zero and the time instant at which the average PVDF voltage starts rising above

zero was found.This time difference was subtracted from the raw impact force signal. This aligns the raw impact force with the raw average PVDF voltage.

Before analyzing and plotting the signals from the load cell and the PVDF sensors, a moving average with a span of 3 elements was used to smooth the aligned raw data. This ensures that the peak values of the impact force and the average PVDF voltage are not reduced as much as they would be with a moving average of 10 elements.

For each of the four drop tests, the following steps were followed:

1. For each time instant, the longitudinal stress (Z stress) acting on all the elements of the PVDF sensor's model in LS-DYNA was averaged. This was done for the entire duration of the impact event in order to obtain the average Z stress acting on the PVDF sensor during impact.

2. This was further converted into the voltage generated by the PVDF sensor, using (4.2). Thus, one obtains a time history of the expected voltage generated by the PVDF sensor based on the results of the simulation.

3. This time history of expected voltage generated by the PVDF sensor was then compared against the impact force measured by the load cell and the average PVDF sensors' generated voltage measured experimentally.

4. The proportionality constant k (or impact force sensitivity) is calculated by determining the ratio of the maximum PVDF voltage to the maximum impact force.

Thus

$$k = V_{peak}/F_{peak}, \qquad (4.3)$$

where V_{peak} and F_{peak} are the peak magnitudes of the average PVDF sensor voltage and the impact force respectively.

4.5   Results from the non-destructive impact tests

Note that all the plots in this chapter show the average value of the PVDF sensor's generated voltage and not the actual voltage measured experimentally. All the voltage signals have been inverted to make it easier to compare them against the impact force signal.
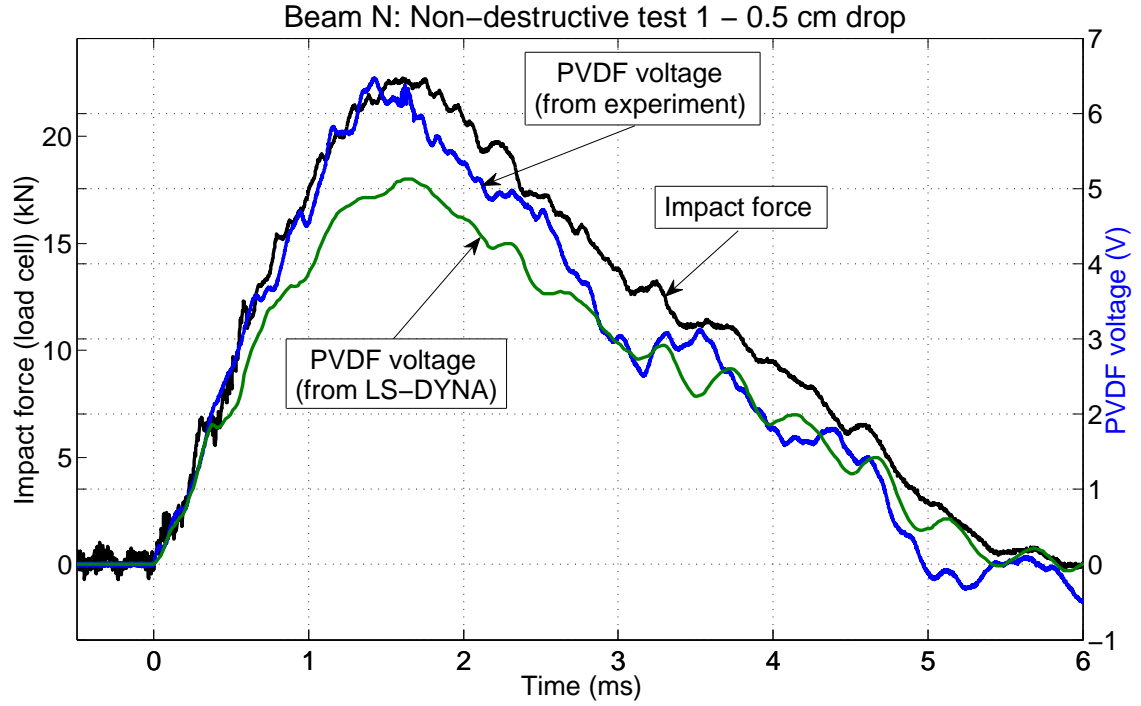
Figure 4.9: Impact force, average PVDF sensor voltage from experiments, and expected PVDF sensor voltage calculated using LS-DYNA for the 0.5 cm drop test.
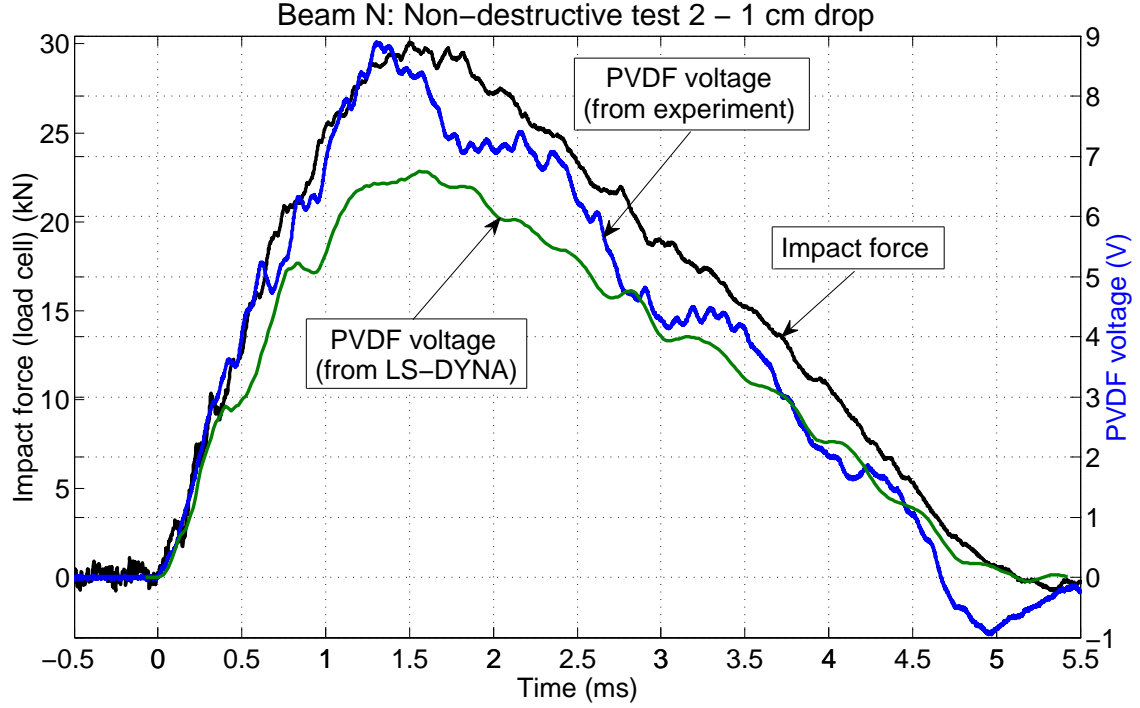
Figure 4.10: Impact force, average PVDF sensor voltage from experiments, and expected PVDF sensor voltage calculated using LS-DYNA for the 1 cm drop test.

Figures 4.9 to 4.12 show the comparison of the impact force measured by the load cell, the average PVDF sensor generated voltage and expected PVDF sensor voltage calculated using the LS-DYNA simulations results, for the 0.5 cm, 1 cm, 1.5 cm, and 3 cm drop tests respectively. Each figure shows two Y axes corresponding to the PVDF voltage and the impact force. The proportionality constant k defined by (4.3) has been used to scale the two Y axes in all of the four figures mentioned above.
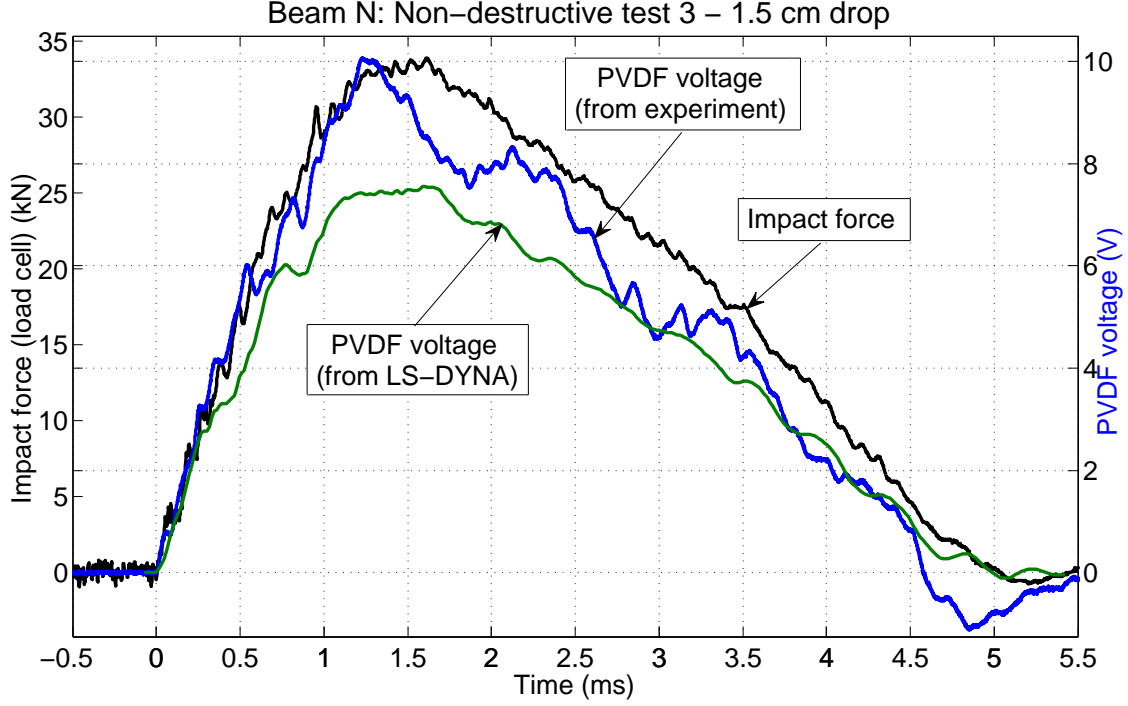
Figure 4.11: Impact force, average PVDF sensor voltage from experiments, and expected PVDF sensor voltage calculated using LS-DYNA for the 1.5 cm drop test.

The average proportionality factor k based on the four non-destructive impact tests is 0.29 V/kN. Based on the results of the four non-destructive impact tests, it can be seen that the experimental PVDF voltage and the impact force align closely with each other in the time range in which both signals are rising. This time range is the most important, from the viewpoint of impact detection. Hence, the close alignment of the two signals in this time range validates the choice of the proportionality constant k defined using (4.3). Hence, for the destructive impact tests, it can be assumed that the average proportionality constant k (0.29 V/kN) is valid for the duration from the start of impact to the time instant at which the both the impact force as well as

Figure 4.12: Impact force, average PVDF sensor voltage from experiments, and expected PVDF sensor voltage calculated using LS-DYNA for the 3 cm drop test.

the experimental PVDF voltage reach their peaks (note that these two signals may not reach their peak at the same time). Beyond the time interval mentioned here, although the two signals start showing misalignment, they still follow the same general profile. At the maximum extent of misalignment, if k is used calculate the impact force from the PVDF voltage, the error is less than 20 %. From the results shown, it is clear that the maximum misalignment between the two signals only occurs at a few time instants after the peak of impact. Taking these observations into consideration, for the destructive tests, the proportionality factor k has been assumed to be valid

73

Parameter	Beam N			
	Test 1	Test 2	Test 3	Test 4
Drop height (cm)	0.5	1	1.5	3
Peak average generated PVDF voltage (from the experiment) (V)	6.47	8.90	10.10	11.36
Peak expected PVDF voltage (from the simulation) (V)	5.13	6.75	7.56	8.69
% difference between the peak PVDF voltage from the experiment and from the simulation	21	24	25	24
Peak impact force (kN)	22.73	30.11	33.87	39.42
Proportionality constant k (V/kN)	0.28	0.30	0.30	0.29

Table 4.1: Summary of the results from the non-destructive impact tests on beam N.

for the entire duration of impact. Thus, for the destructive tests

$$F(t) = V(t)/k = V(t)/0.29, \qquad (4.4)$$

where $F(t)$ is in kN and $V(t)$ is in V.

Table 4.1 summarizes the results of all four non-destructive impact tests on beam N. The results also show that the voltage predicted by the LS-DYNA model is less than the actual voltage measured for each test by an average of 24% of the value of the measured voltage. This implies that the beam modeled in LS-DYNA is stiffer than the actual beam used for the tests. Some possible reasons for the deviation of the simulation results from the experimental results have been discussed as follows:

- The simulation may differ from the experiment because of the complex structure of the hollow beam. The hollow beam used for the tests is not exactly symmetric, unlike the beam modeled in LS-DYNA. The symmetry of the beam modeled in LS-DYNA could be the reason for its higher stiffness.

- If the impacting plate in the experiment did not hit the top of the beam in a perfectly parallel manner, it could cause non-uniform distribution of the impact force on the beam. In contrast, the impact force in the simulation is applied uniformly over the top of the beam.

- It is likely that because of the complexity of the beam's geometry, the non-parallel impact, and the fact that the beam is made of thin sheet metal, the stress at the sensor locations in the experiment is not predominantly longitudinal. This non-longitudinal stress may be causing an increase in the generated voltage in the experiment.

It would be very tedious to exactly model all the imperfections in the actual beams. Also, new models would be needed for each impact test, since each destructive test used a new beam. Hence, no changes were made in the LS-DYNA model which was used for all non-destructive and destructive tests.

4.6   Destructive impact tests on hollow steel beams

The purpose of the destructive impact tests was to study the response of the PVDF sensors in a high energy impact event, in which the structure they are bonded to gets damaged. In this experiment, additional weights were added to the drop head, thereby increasing the total mass of the drop head to 227 kg. Two destructive impact tests were conducted, using a new hollow beam for each test. For the first impact test, the drop height was set to 87 cm. Given the length of the hollow beams, this is the maximum drop height that can be set using the available impact tester. For the second impact test, the drop height was set to 58 cm (two thirds of the maximum drop height). The beams used for the first and second destructive impact tests have

been referred to as beam D1 and beam D2, respectively, in the rest of this chapter. As in the case of the non-destructive tests, LS-DYNA simulations were run using the impact force recorded by the load cell in the experiment as the input force to the rigid plate in the model.

For both impact tests, the following steps were followed:

1. For each time instant, the longitudinal stress (Z stress) acting on all the elements of the PVDF sensor's model in LS-DYNA was averaged. This was done for the entire duration of the impact event in order to obtain the average Z stress acting on the PVDF sensor during impact.

2. This was further converted into the voltage generated by the PVDF sensor, using (4.2). Thus, one obtains a time history of the expected voltage generated by the PVDF sensor based on the results of the simulation.

3. This time history of expected voltage generated by the PVDF sensor was then compared against the impact force measured by the load cell and the average PVDF sensors' generated voltage measured experimentally.

4. The detected impact force was calculated using the experimental PVDF voltage, using (4.4).

4.7   Results from the destructive impact tests

For presenting the results from these tests, plots similar to the ones used for the non-destructive tests have been shown. The two Y axes corresponding to the impact force and the PVDF voltage have been scaled using k (0.29 V/kN). Thus, the blue curve is the experimental PVDF voltage, if read against the Y axis corresponding to the PVDF voltage. At the same time, it shows the detected impact force if
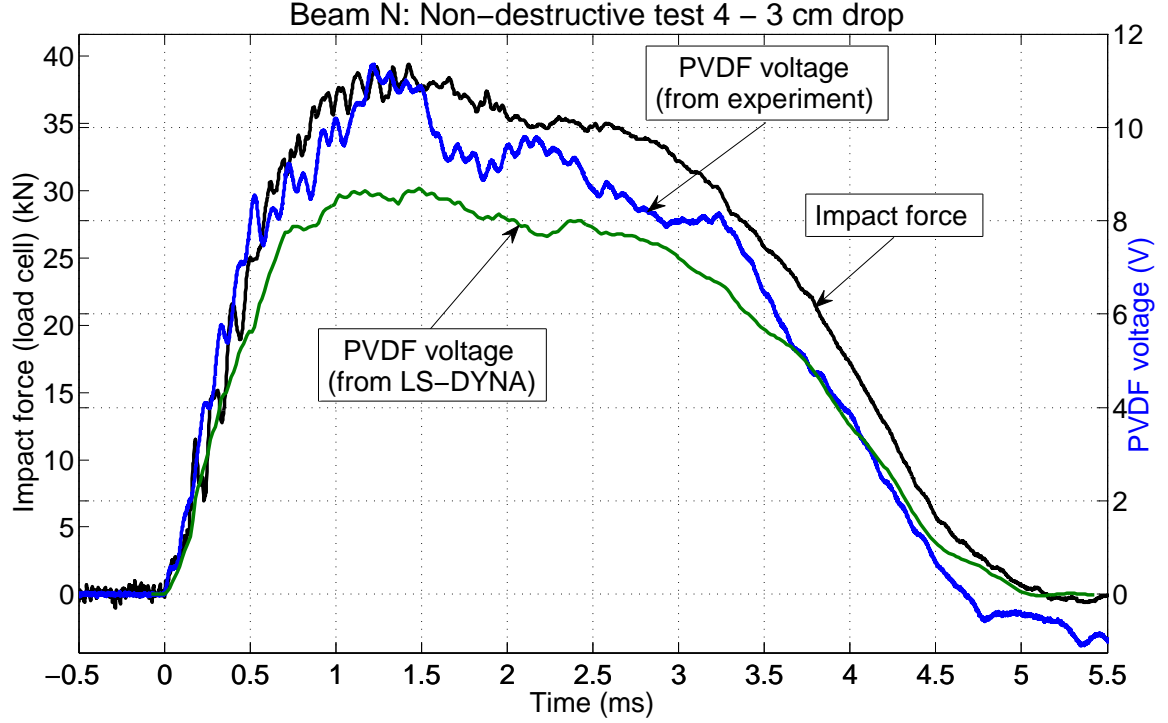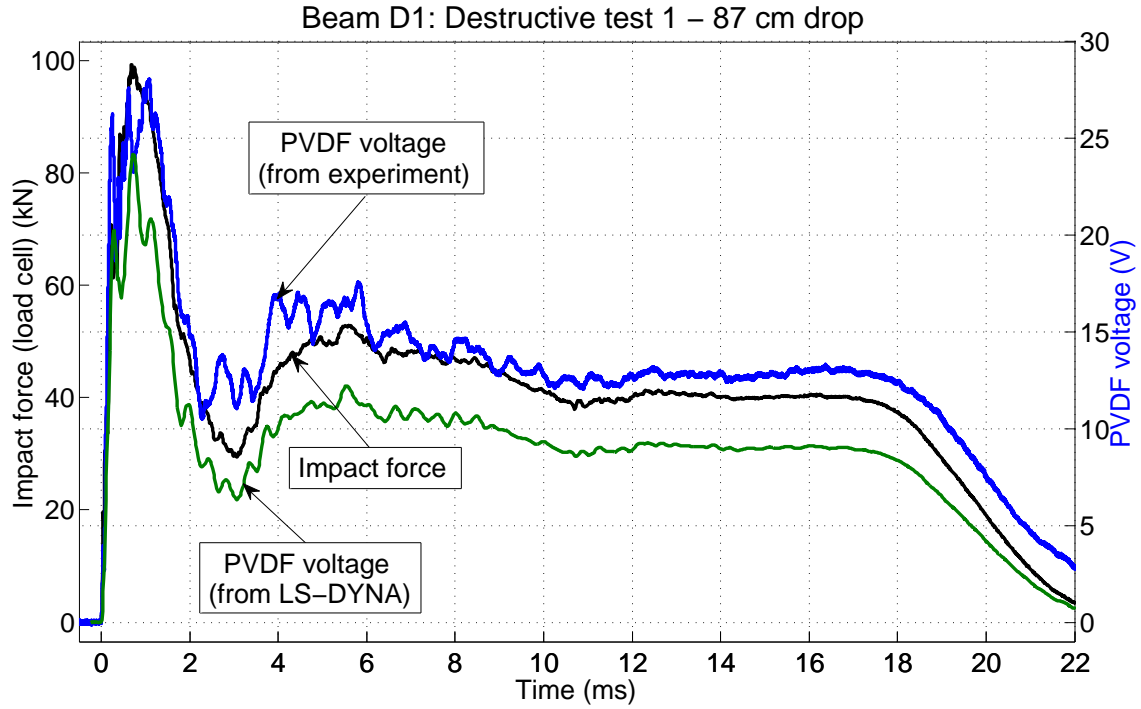
Figure 4.13: Impact force, average PVDF sensor voltage from experiments, and expected PVDF sensor voltage calculated using LS-DYNA for the 87 cm drop height destructive drop test.

read against the Y axis corresponding to the impact force. Figure 4.13 and Figure 4.14 show the results from the impact tests on beam D1 and beam D2 respectively. The plots show that applying the proportionality factor k calculated from the non-destructive tests leads to a good alignment of the experimental PVDF voltage and the impact force in the destructive tests, especially for the duration of the first peak shown by the two signals (up to ≈ 2.5 ms, for both tests).
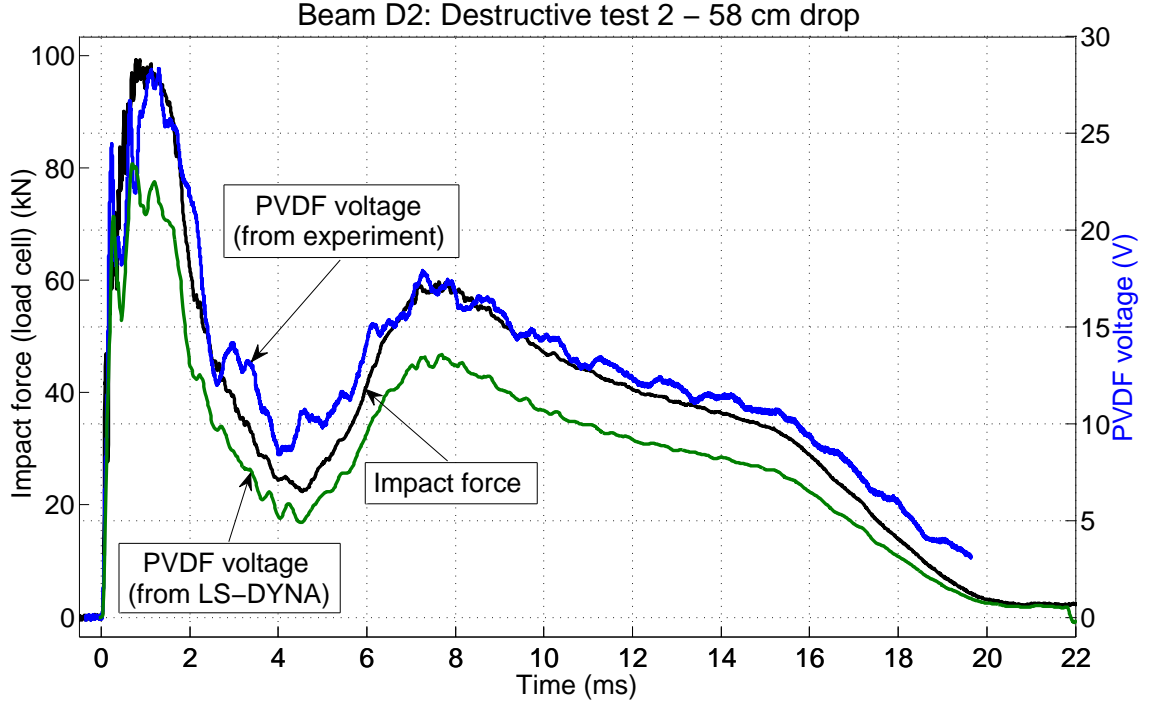
Figure 4.14: Impact force, average PVDF sensor voltage from experiments, and expected PVDF sensor voltage calculated using LS-DYNA for the 58 cm drop height destructive drop test.

Since the blue curve also represents the impact force detected by the PVDF sensor, it can be concluded that the PVDF sensors were successful in detecting the impact force acting on the hollow beams used in the destructive tests. The results summarized in Table 4.2 show that the peak impact force detected by the PVDF sensors is very close to the peak impact force detected by the load cell for both destructive tests. Thus, using PVDF sensors, a simple calibration procedure such as the one followed in the non-destructive tests can be used to closely detect the magnitude of the impact force acting on the structure, even in the case of high-energy destructive impacts with

permanent deformation. Table 4.2 summarizes the results from the two destructive tests.

Parameter	Test 1 (Beam D1)	Test 2 (Beam D2)
Drop height (cm)	87	58
Peak average generated PVDF voltage (from the experiment) (V)	28.02	28.30
Peak expected PVDF voltage (from the simulation) (V)	24.16	23.32
% difference between the peak PVDF voltage from the experiment and from the simulation	14	17
Peak impact force (kN)	99.14	99.40
Peak impact force detected by the PVDF sensor using (4.4) (kN)	99.62	97.59

Table 4.2: Summary of the results from the destructive impact tests.

Figure 4.13 and Figure 4.14 also show that the PVDF voltage calculated based on the LS-DYNA simulations is lower in magnitude compared to the experimental results. Also, the beam modeled in the LS-DYNA simulations does not show any permanent deformation under application of the impact forces from the destructive tests. The reason for this may be a higher stiffness of the beam modeled in LS-DYNA due to perfect geometry and impact conditions as discussed in the previous section.
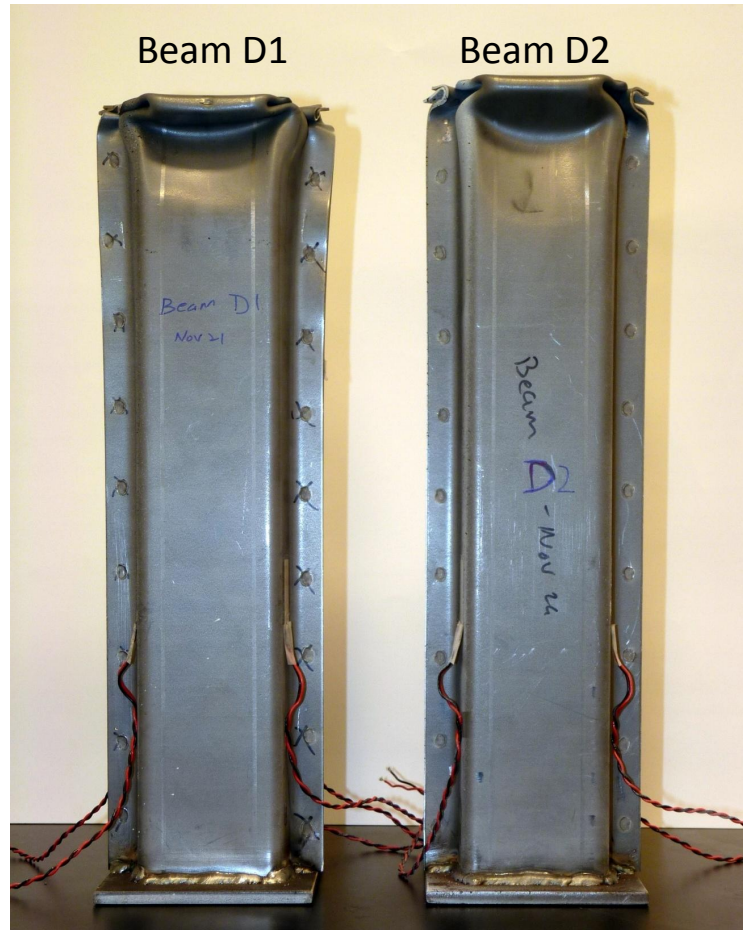
Figure 4.15: Beams D1 and D2 after the destructive tests from drop heights of 87 cm and 58 cm, respectively.

Figure 4.15 shows the pictures of beams D1 and D2 at the end of the destructive tests. Beams D1 and D2 were deformed permanently (or crushed) by about 35 mm and 25 mm respectively. Both tests show similar values of peak impact force ($\approx$ 99 kN). This indicates that 99 kN may be the maximum impact force that the hollow beams can resist; beyond this force, the beams start yielding (deforming) at the top.

4.8 Conclusions

- The average proportionality constant k between the PVDF sensors' voltage and the impact force was determined from the non-destructive impact tests (peak forces between 22-40 kN) on a hollow beam.

- Despite the geometric complexity of the hollow beams, the average proportionality constant was shown to be valid for the destructive tests (peak forces $\approx$ 99 kN) too and was used to determine the impact force detected by the PVDF sensor.

- While the shapes of the curves were similar, the LS-DYNA model predicted a lower magnitude of voltage generated by the PVDF sensor, compared to the experimental PVDF sensor voltage. The possible causes for the difference between the simulation and the experiment include the lack of a perfectly parallel impact in the experiment and the lack of an exact model with all the geometric imperfections of the hollow beams tested.

Chapter 5: PLANE STRESS WAVE PROPAGATION IN A SLENDER ROD

This chapter describes an experiment in which the speed of sound for longitudinal plane stress waves in a slender rod, made of a known material, was measured using PVDF sensors. The purpose of this experiment is to demonstrate that PVDF sensors can be reliably used to detect the propagation of impact-induced stress waves in a structure, even when the wave transit time between two PVDF sensors is very low (on the order of a few microseconds).

5.1   Experimental setup

The material of the rod was 316 L stainless steel. The diameter of the rod was 32 mm and its length was 350 mm. Two PVDF sensors were bonded to the rod at a distance of about 67 mm from each free end (measured between the PVDF film and the end of the rod). The rod was suspended horizontally using thin fishing wires, as shown in Figure 5.1.

The DT1-028K PVDF sensors, which do not have protective Mylar coatings like the LDT1-028K sensors, were used in this experiment. A thin urethane coating covers the silver ink electrodes on both sides of the PVDF film. The DT1-028K sensors are more compliant than the LDT1-028K sensors. This makes it easier to bond them to
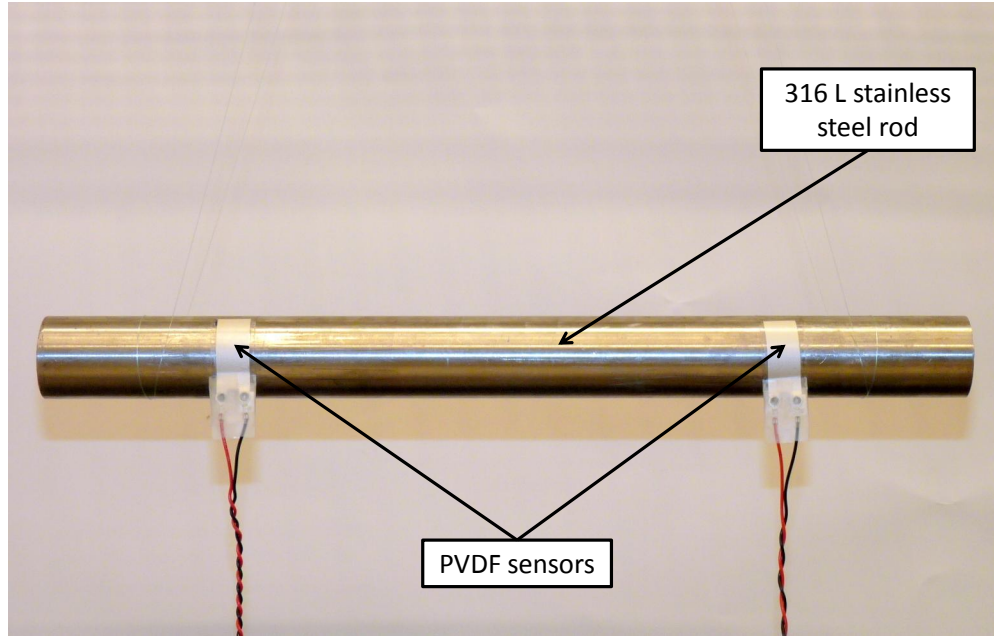
Figure 5.1: A picture of the suspended rod, used for measuring stress wave transit time, with the PVDF sensors attached.

a curved surface like that of the rod. The dimensions of these sensors are the same as the LDT1-028K sensors (which have been described in detail in Chapter 2).

The suspended rod was impacted at one of its free ends by a piezoelectric impact hammer (PCB 086C03). The voltages generated by the two PVDF sensors were recorded by an oscilloscope (Agilent 54622A) with a sampling frequency of 200 MHz. Another oscilloscope of the same type was used to record the signal generated by the impact hammer. The signal from the impact hammer triggers the data acquisition for both the oscilloscopes.

5.2 Theoretical considerations and stress wave transit time measurement

Figure 5.2 shows a diagram of the experimental setup. A horizontally suspended slender rod of circular cross section was used as the medium for the propagation of stress waves.
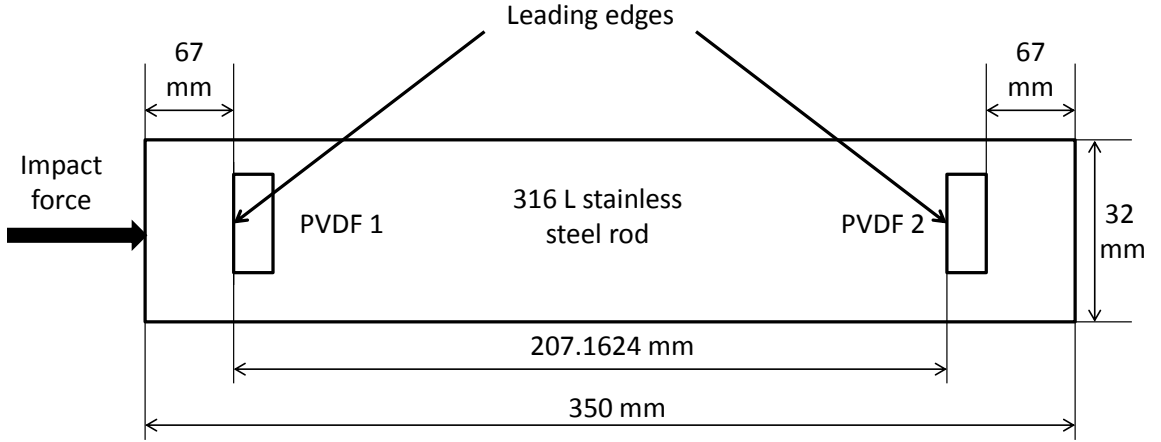
Figure 5.2: Diagram showing the dimensions of the experimental setup used for measuring stress wave transit time.

The impact force acting on one end of the rod (which is hit by an impact hammer) induces stress waves in the rod. These stress waves propagate along the length of the rod and first reach PVDF 1 (the sensor closer to the impacted end) and then PVDF 2. Both PVDF 1 and PVDF 2 start generating voltages at the time instants when the traveling stress front reaches their respective leading edges. The time interval between the rise of the voltages of the two sensors can be measured, and will be equal to the time the stress wave takes to travel from the leading edge of PVDF 1 to the leading edge of PVDF 2. This has been referred to as the stress wave transit time in

the rest of this chapter. By measuring the stress wave transit time and the distance between the two leading edges (207.1624 mm), the speed of sound in the medium can be calculated.

The above analysis employs the elementary theory of one dimensional stress wave propagation. This theory assumes a uniaxial (longitudinal) state of stress in the rod after impact. It assumes that impact consists of a uniform compressive force applied suddenly on one of the free ends of the rod. This induces compressive stress in an infinitely thin layer of the material on the impacted end of the rod. This compressive stress propagates along the length of the rod in the form of a plane wave stress front [19]. This elementary theory is valid only when the lateral inertia effects (caused by contraction and expansion in the lateral direction) are ignored. These effects are responsible for the dispersive behavior of the propagating stress wave and lead to a distortion of the shape of the stress wave. The lateral inertia effects can be ignored if the duration of the impact force is large compared to the time it takes for the stress wave to travel across the radius of the rod [20]. This condition can be verified by measuring the time of application of the force, as measured by the impact hammer. Figure 5.3 shows the impact forces from three tests. It can be seen that the shortest duration of application of load is in the case of Test 4. Here, the force is applied for a period of $120\,\mu s$. The time for the transit of stress wave (t_r) across the radius of the rod can be calculated as

$$t_r = \frac{r}{c_t} = r \cdot \sqrt{\frac{\rho}{G}}, \tag{5.1}$$

where r is the radius of the rod, c_t is the speed of propagation of the transverse (or lateral) waves, ρ is the density of the material, and G is the shear modulus of the material.
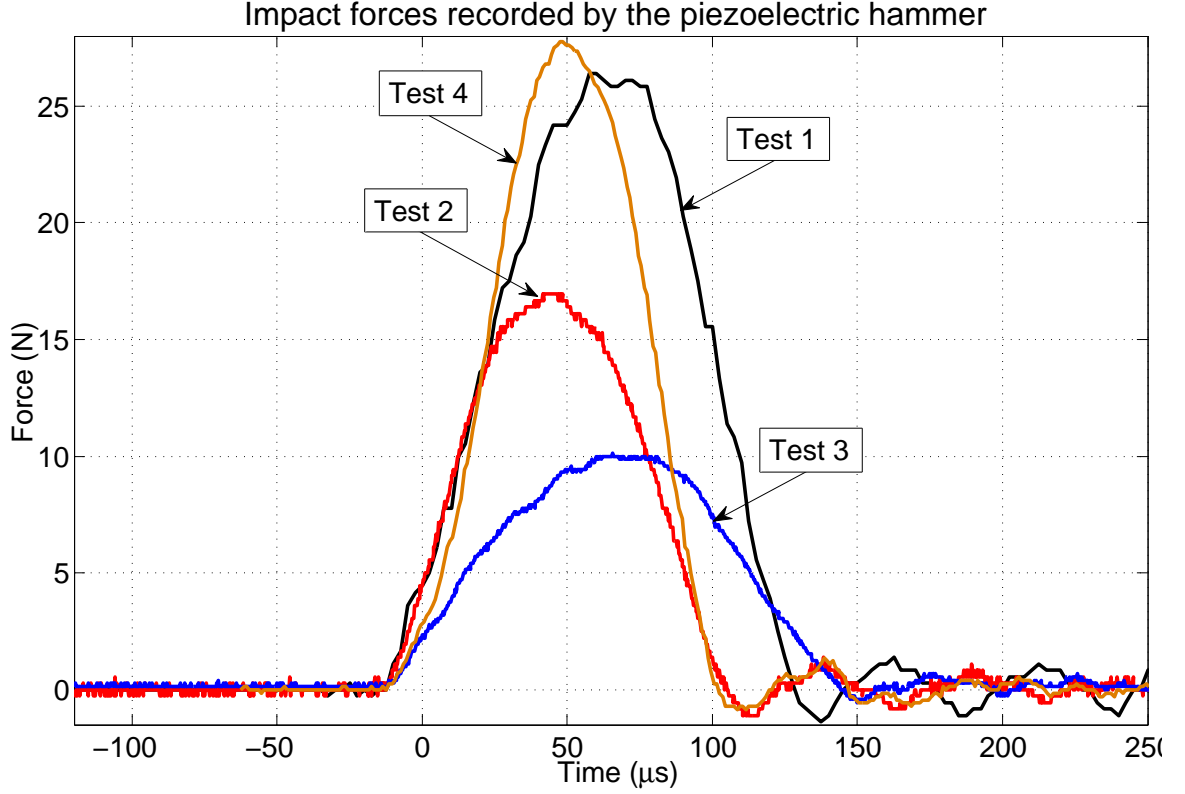
Figure 5.3: Impact forces acting on the end of the rod, recorded by the piezoelectric impact hammer as a part of the stress wave transit time experiment.

For 316 L stainless steel, $\rho = 8000$ kg/m^3 and $G = 82$ GPa. Substituting these values in (5.1), one obtains $t_r = 5$ µs. Thus, the time of application of the force (120 µs) is 24 times as large as t_r. Hence, it can be concluded that the elementary theory of one dimensional stress wave propagation is valid for this experiment. Consequently, the speed of sound for longitudinal waves that are generated in the rod due to impact, can be written as

$$c = \sqrt{\frac{E}{\rho}}, \tag{5.2}$$

where E is the elastic modulus of the material. For 316 L stainless steel, $E = 193$ GPa. Substituting the values of E and ρ in (5.2), one obtains the theoretical value of the speed of sound for longitudinal waves as $c = 4911.72$ m/s.

The stress wave propagates across the width of the PVDF sensors when they are bonded to the rod in the orientation used in this experiment. This means that the sensors are operating in 32 mode. The reason for choosing the 32 mode as opposed to 31 mode is that it is easier to bond the sensors in the 32 orientation. Bonding the sensors in 31 orientation (sensors aligned parallel to the length of the rod) causes an inconvenient fold near the leads.

5.3   Discussion of results
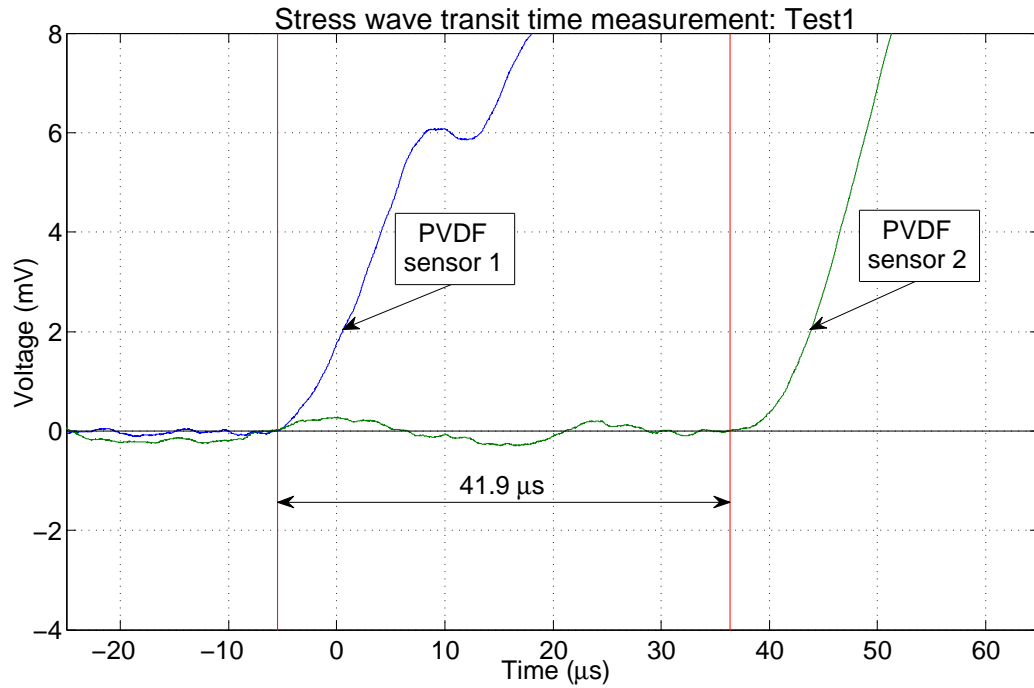
Figure 5.4: Stress wave transit time measurement for Test 1.
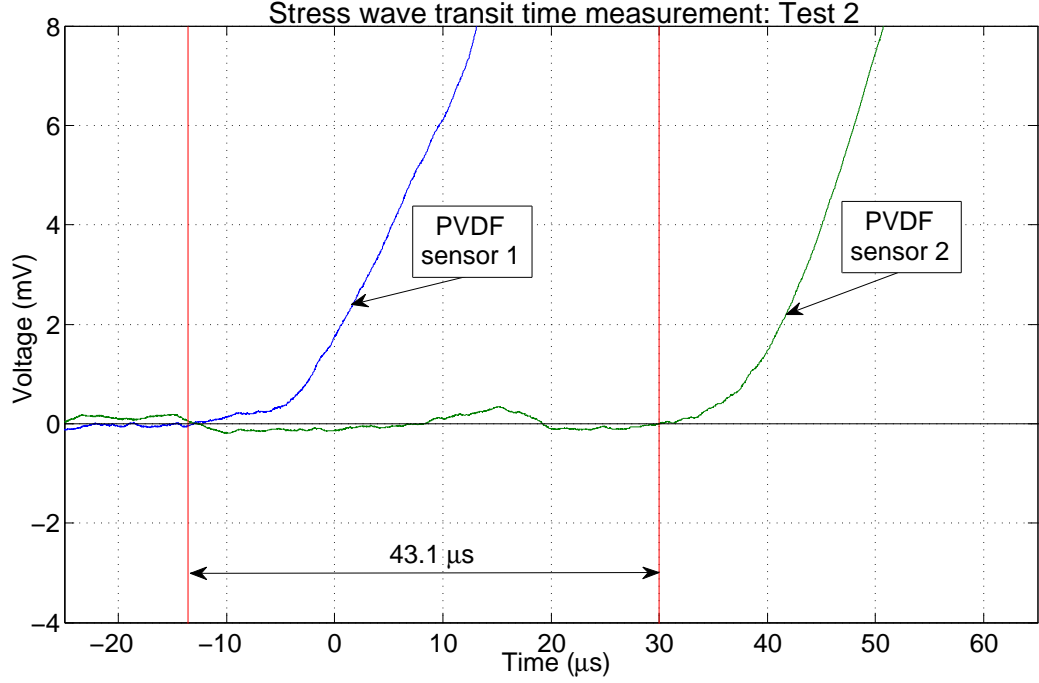
Figure 5.5: Stress wave transit time measurement for Test 2.

Figures 5.4 to 5.6 show the plots of voltages generated by the two sensors in the three tests. The voltages shown in all the plots have been inverted. A moving average with a span of 1000 elements (corresponding to 5 µs) has been applied to all the voltages before plotting. The following steps were followed for determining the stress wave transit time:

1. The mean voltage level for each PVDF sensor before impact (i.e. before its voltage starts rising) was calculated and subtracted from the respective PVDF signal. This made the mean voltage level of both PVDF sensors zero before impact.

2. For each PVDF sensor, the time instant at which the voltage rose above zero, and did not fall below zero subsequently (for at least 50 µs), was selected. These
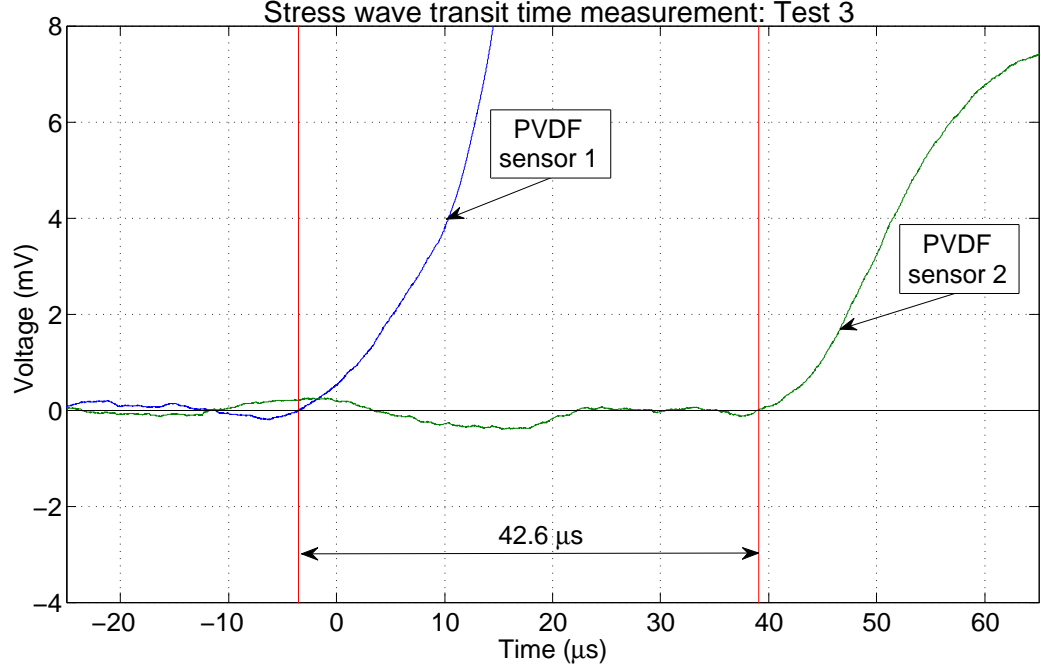
Figure 5.6: Stress wave transit time measurement for Test 3.

time instants have been shown using red vertical lines in Figure 5.4, Figure 5.5, and Figure 5.6.

3. The duration of time between the above mentioned instants was calculated for each of the three tests. This is the value of the stress wave transit time between the two sensors.

Using the value of the stress wave transit time (t) for each test, the experimentally measured speed of sound (c_{exp}) can be calculated as

$$c_{exp} = \frac{\text{distance traveled}}{\text{transit time}} = \frac{207.1624 \times 10^{-3} \text{m}}{t}, \tag{5.3}$$

where t is in seconds and c_{exp} is in m/s. Table 5.1 summarizes the results showing the experimentally calculated speed of sound using (5.3), for each test. It also shows the

percentage error between the theoretical speed of sound and the experimental value. The average value of c_{exp} is 4871 m/s and the percentage error between this value and c is 0.8 %.

Test number	c_{exp} (m/s)	Percentage error between c and c_{exp} (%)
1	4944	0.7
2	4807	2.1
3	4863	1.0

Table 5.1: Summary of the results from the stress wave transit time experiment.

5.4   Test conducted using the LDT1-028K sensor

Test 4 was conducted with an additional LDT1-028K sensor attached to the rod at the same location along its length as sensor 1. The sampling frequency for the PVDF sensor signals was 25 MHz in this test. The LDT1-028K sensor (referred to as sensor 3 hereafter) has 55 μm thick Mylar coatings on both sides. The results from this test are shown in Figure 5.7. It is observed that the sensor 3 generated a higher magnitude of voltage compared to sensor 1 and sensor 2. Figure 5.8 shows the power spectrum of the voltage signals from this test. The power spectrum of sensor 3's voltage shows two peaks which are significantly higher than the other two sensors' power spectrums.
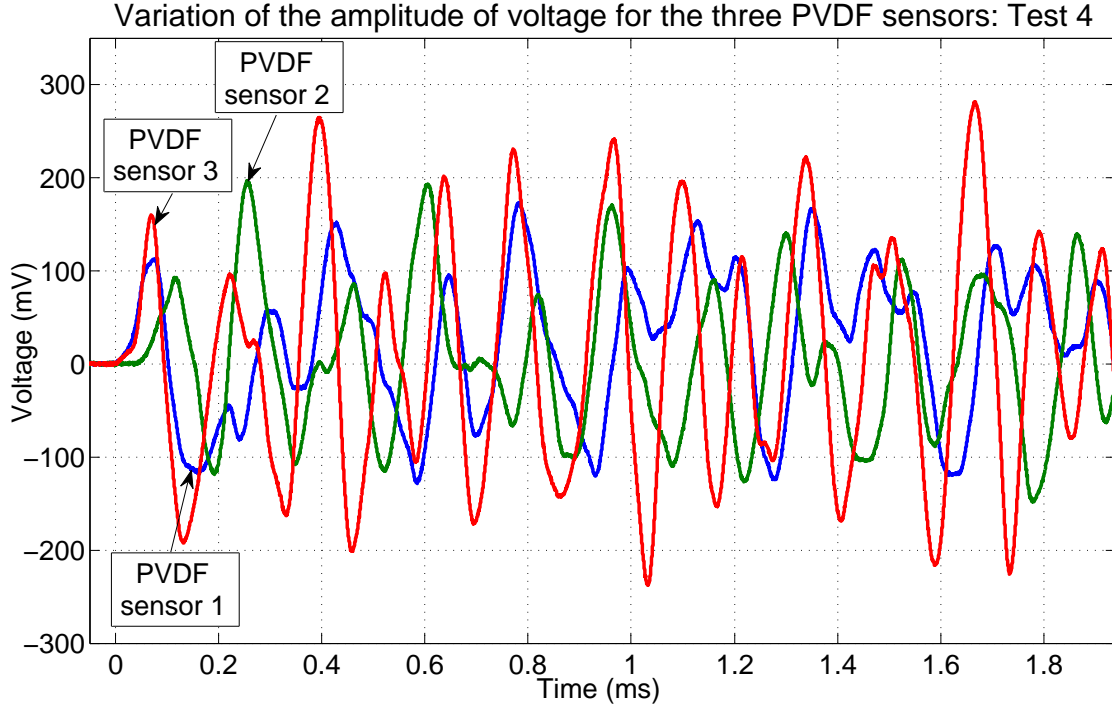
Figure 5.7: Variation of the amplitude of voltage generated by the three PVDF sensors due to impact.

These peaks occur at frequencies 6.9 kHz and 8.8 kHz. These peaks may be related to resonance occurring at those frequencies. Since sensor 1 and sensor 3 are at the same location along the length of the rod, the difference in the voltage response of the two sensors must be related to a difference in the dynamic behavior of the two types of sensors (caused by the presence or absence of the Mylar layers). Another possible cause for the difference in the voltages generated by sensor 1 and sensor 3 could be the slight variations in experimental conditions related to bonding of the two sensors, like variations in the amount of sensor area glued or variations in the thickness of the layer of glue. It is also possible that because of the additional stiffness of the

Mylar layer, some of the strain gets transferred to the unglued portion of sensor 3 and thereby causes the sensor to generate a higher magnitude of voltage.
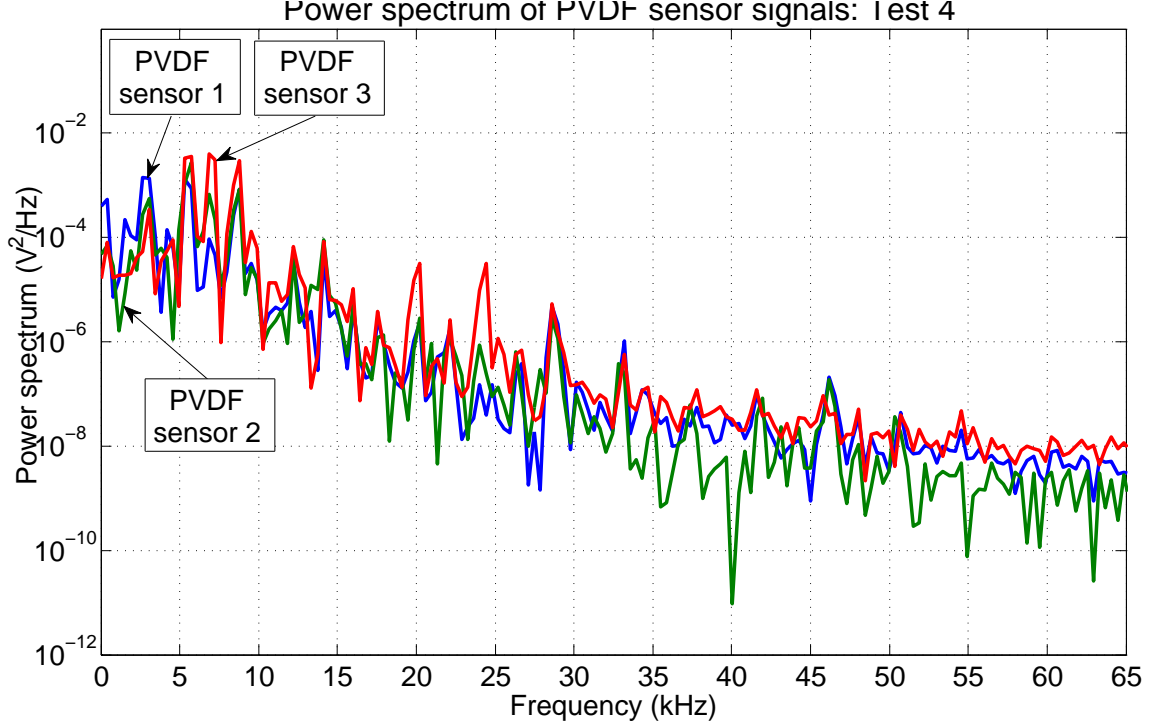
Figure 5.8: Power spectrum of the three PVDF sensor signals.

5.5 Speed of the PVDF sensor's response

Figure 5.9 shows that in Test 4, the time gap between the rise of the impact force and PVDF sensor 1 voltage was 13.1 µs. The distance between the impacted end of the rod and PVDF sensor 1 was measured as 65.6844 mm. Thus, using these values and (5.3) one obtains the experimentally measured speed of sound $(c_{exp}) = 5014$ m/s. The percentage error between this value and the theoretical value of speed of sound in 316 L stainless steel is 2.1 %. Since the percentage error is low, it can be concluded

that the speed of sound in the rod can be calculated accurately by measuring the stress wave transit time from the impacted end to PVDF sensor 1. This implies that the PVDF sensor does not introduce any time lag between the arrival of the traveling stress wave and the generation of voltage. Hence, it can be concluded that the PVDF sensor responds instantaneously to the incoming stress waves.
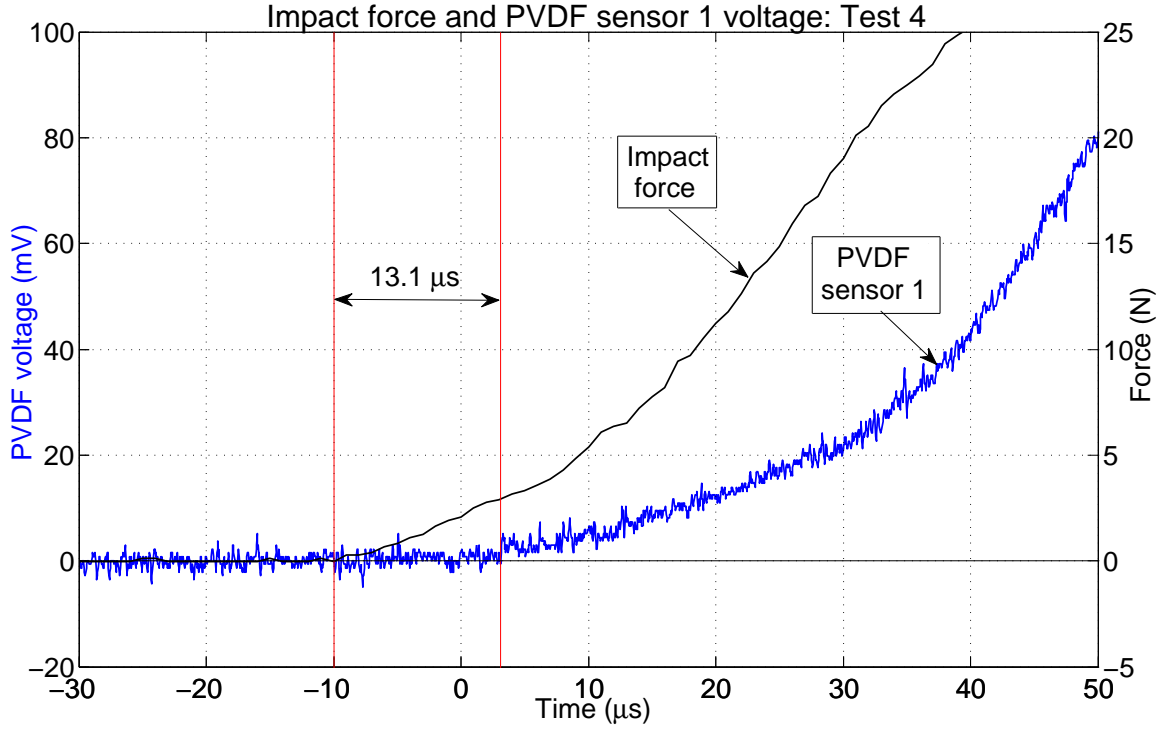
Figure 5.9: Time gap between the rise of the impact force and the voltage from sensor 1 for Test 4.

5.6   Conclusions

- The percentage error between the average experimentally measured value and the theoretical value of the speed of sound for longitudinal waves in a 316 L stainless steel rod was found to be very low (0.8%). In addition, for the wave

speeds measured, the PVDF sensors do not introduce any delay in the detection of stress waves. This demonstrates that PVDF sensors are capable of reacting fast enough to stress waves propagating through a structure, so as to be able to accurately measure wave transit times on the order of a few microseconds.

- The highest frequency that can be measured by the PVDF sensor is 1 GHz which is the upper limit for the PVDF film, published by the manufacturer [1]. Thus, the shortest measurable wave transit time is 1 ns.

- The PVDF sensors are sensitive enough to be able to measure the small amount of strain on the bar, associated with the traveling stress waves caused by low magnitude impact forces (as low as 10 N in Test 3).

- It was not necessary to place the PVDF sensors in the direct path of the applied load for detecting the traveling stress wave in the rod, since they were used in 32 mode. This would also be applicable if the sensor was used in 31 mode. However, 33 mode would have required the sensor to be placed directly in the path of the applied load, i.e. one sensor bonded to the face that gets impacted and the other one to the opposite face. This would have resulted in the sensor on the impacted face getting damaged. Further, this sensor could have interfered with the propagation of the stress wave in the rod. Thus, this experiment demonstrates the advantages of using the PVDF sensors in 32 or 31 mode as opposed to 33 mode for the purpose of detection of traveling stress waves.

Chapter 6: STRESS AVERAGING OF A PVDF FILM SENSOR

This chapter discusses the PVDF sensor's stress averaging effect, focusing on two types of stress inputs, namely, periodic applied stress waves and impact-induced stress waves. Equations have been derived to show the dependence of the voltage generated by the sensor, on parameters like length of the sensor and frequency of the applied input. In addition, the results of numerical simulations demonstrating the effect of stress averaging on the PVDF sensor's generated voltage have been presented and discussed.

A PVDF sensor generates a voltage based on the average stress acting on the sensor's area. This stress averaging effect leads to a reduction in the magnitude of generated voltage. The analysis presented in this chapter investigates whether the reduction in voltage is significant for the size of the sensor that was used in the experiments described earlier in this thesis. Further, in certain applications, it may be important to know the true value of stress acting at a location on a structure. Analyzing the stress averaging effect will provide a better understanding of how the stress averaged response deviates from the ideal or true response of the sensor.

Symbol	Meaning	SI unit
b	Breadth of the PVDF sensor	m
L	Length of the PVDF sensor	m
d	Distance between the free end of the bar and the middle of the PVDF sensor	m
E_s	Young's modulus of the PVDF sensor	Pa
E_b	Young's modulus of the bar	Pa
ρ_b	Density of the bar	$\mathrm{kg/m^3}$
A_b	Area of the cross section of the bar	$\mathrm{m^2}$
t	time	s
ω	Angular frequency of the periodic applied stress wave	rad/s
σ_b	Maximum amplitude of the periodic applied stress wave	Pa

Table 6.1: List of symbols used in Chapter 6.

Table 6.1 shows the list of most of the new symbols introduced in this chapter. The rest of the symbols have been explained in Table 2.1. Some additional symbols will be explained in the text in this chapter.

6.1 PVDF sensor's response to periodic stress waves

Consider a long slender bar, having the top end free and the bottom end fixed, as shown in Figure 6.1 with the PVDF sensor attached to it. The analysis presented in this section is based on the following assumptions:

- The PVDF sensor and the bar are perfectly elastic.

- The bonding between the PVDF sensor and the structure is perfect; thus the strain induced in the structure is transferred completely to the PVDF sensor.

- The compressive stress applied to the top of the bar is uniformly distributed.

- The time window that is considered for the analysis is small enough so as to ensure that the stress waves retuning to the PVDF sensor after being reflected at the fixed end can be ignored.

- The PVDF sensor is operating in open circuit mode.

- The force applied in the longitudinal direction creates predominantly longitudinal stress waves; the lateral and out-of-plane components of stress have been assumed to be negligible.

- The PVDF sensor does not influence the stress generated in the bar due to the applied force.

The last assumption can be understood better by considering the fact that the stiffness of the PVDF sensor (k_s), and the stiffness of the length of the bar over which the PVDF sensor is attached (k_b), can be assumed to be in parallel with one another. The equivalent stiffness (k_{eq}) of the system can be written as

$$k_{eq} = k_s + k_b = \frac{A_b E_b}{L} + \frac{A_s E_s}{L} = \frac{A_b E_b + A_s E_s}{L}, \qquad (6.1)$$

where A_s is the cross-sectional area of the sensor. In practice, the structure is made of a material that has a significantly high Young's modulus, compared to the PVDF sensor. Also, the PVDF sensor's thickness is very small (on the order of micrometers). Thus, both A_s and E_s are very small compared to A_b and E_b. Hence k_{eq} defined in (6.1) can be approximated as

$$k_{eq} \approx \frac{A_b E_b}{L} \approx k_b. \qquad (6.2)$$

Thus, from (6.2) one can see that the equivalent stiffness of the system of the PVDF sensor bonded to the bar is practically unaffected by the PVDF sensor, which in turn

implies that the PVDF sensor does not influence the stress generated in the bar due to the applied force.

Let $\sigma_b(t)$ be the longitudinal stress wave acting on the top (or free end) of the bar along the longitudinal direction, where

$$\sigma_b(t) = \sigma_b \sin \omega t, \tag{6.3}$$

and the longitudinal force $F(t)$ at the top of the bar is

$$F(t) = \sigma_b(t)A = \sigma_b A \sin \omega t. \tag{6.4}$$

The stress $\sigma_b(t)$ acting on the bar causes strain $\epsilon_b(t)$ in the bar, where

$$\epsilon_b(t) = \sigma_b(t)/E_b \tag{6.5}$$

which implies that the strain transferred to the PVDF sensor $\epsilon_s(t)$ can be written as

$$\epsilon_s(t) = \epsilon_b(t) = \sigma_b(t)/E_b. \tag{6.6}$$

However, the stress acting on the PVDF sensor can be written as

$$\sigma_s(t) = E_s \epsilon_s(t), \tag{6.7}$$

where $\sigma_s(t)$ is the stress acting on the PVDF sensor. Thus, using (6.6) and (6.7), one can write

$$\sigma_s(t) = \frac{E_s}{E_b}\sigma_b(t). \tag{6.8}$$

As shown in Figure 6.1, a force $F(t)$ is applied on the top of the bar, along the longitudinal direction. Consider a section of the bar at a distance x from the top of the bar, as shown in Figure 6.1. At the time instant when the force at the top of the bar is $F(t)$, the force acting on a cross section at a distance x from the top, is

Figure 6.1: Diagram showing the fixed bar and the PVDF sensor bonded to it.

$F(t - t_{lag})$. Here, t_{lag} is the time it takes for the stress wave to travel a distance x along the bar. Hence, the stress acting on a cross section at a distance x from the top is $\sigma_b(t - t_{lag})$. Also, the stress acting on the PVDF sensor at Section A (which is at a distance of x from the top), at that same time instant is $\sigma_s(t - t_{lag})$. The stress wave travels at a speed c through the bar, which is given by

$$c = \sqrt{\frac{E_b}{\rho_b}}. \tag{6.9}$$

Thus,

$$t_{lag} = x\sqrt{\frac{\rho_b}{E_b}}, \text{ and} \tag{6.10}$$

$$\sigma_s(t - t_{lag}) = \sigma_s\left(t - x\sqrt{\frac{\rho_b}{E_b}}\right). \tag{6.11}$$

At any time instant t, the average stress acting on the PVDF sensor can be written as

$$\sigma_{savg}(t) = \frac{1}{L}\int_{d-L/2}^{d+L/2} \sigma_s\left(t - x\sqrt{\frac{\rho_b}{E_b}}\right) \mathrm{d}x. \tag{6.12}$$

99

Substituting the expression for $\sigma_s(t)$ from (6.8) into (6.12), one obtains

$$\sigma_{savg}(t) = \frac{E_s}{LE_b} \int_{d-L/2}^{d+L/2} \sigma_b \left(t - x\sqrt{\frac{\rho_b}{E_b}}\right) dx, \qquad (6.13)$$

and expanding $\sigma_b(t)$ in (6.13) using (6.3), gives

$$\sigma_{savg}(t) = \frac{\sigma_b E_s}{LE_b} \int_{d-L/2}^{d+L/2} \sin \omega \left(t - x\sqrt{\frac{\rho_b}{E_b}}\right) dx. \qquad (6.14)$$

Using (2.6), which gives the open circuit voltage, and neglecting the terms for lateral stress and out-of-plane stress, one obtains

$$V_{31}(t) = \text{voltage generated in 31 mode} = g_{31}h\sigma_{savg}(t). \qquad (6.15)$$

Thus, substituting (6.14) into (6.15), one obtains

$$V_{31}(t) = \frac{\sigma_b E_s g_{31} h}{LE_b} \int_{d-L/2}^{d+L/2} \sin \omega \left(t - x\sqrt{\frac{\rho_b}{E_b}}\right) dx, \qquad (6.16)$$

which can be integrated to obtain

$$V_{31}(t) = \left(\frac{2\sigma_b E_s g_{31} h}{LE_b \omega} \sqrt{\frac{E_b}{\rho_b}}\right) \sin\left(\frac{\omega L}{2}\sqrt{\frac{\rho_b}{E_b}}\right) \sin \omega \left(t - d\sqrt{\frac{\rho_b}{E_b}}\right). \qquad (6.17)$$

Using (6.9), one can rewrite (6.17) as

$$V_{31}(t) = \left(\frac{2\sigma_b E_s g_{31} hc}{LE_b \omega}\right) \sin\left(\frac{\omega L}{2c}\right) \sin \omega \left(t - \frac{d}{c}\right). \qquad (6.18)$$

The voltage generated by the PVDF sensor by averaging the stress acting on it is given by (6.18), taking into account the sensor's stress averaging effect. It shows that the voltage generated does not depend on the width of the sensor. Even if the width of the PVDF sensor is varied, the strain acting on the sensor (which causes stress to develop in the sensor) will be unaffected since it only depends upon the strain in the structure. From (6.17), which is another form of (6.18), it can be seen that the

voltage generated by the sensor depends upon the material properties of the sensor as well as the bar.

If the sensor was rotated by 90 degrees in the horizontal plane and bonded to the bar, it would be in the 32 mode of operation. To analyze the effect of sensor averaging in 32 mode, one just has to replace L in (6.18) with b, the breadth of the sensor and g_{31} with g_{32}. Thus, for 32 mode, one obtains

$$V_{32}(t) = \left(\frac{2\sigma_b E_s g_{32} hc}{b E_b \omega}\right) \sin\left(\frac{\omega b}{2c}\right) \sin\omega\left(t - \frac{d}{c}\right). \tag{6.19}$$

6.2 Numerical simulations for periodic stress wave input

The properties of the LDT1-028K PVDF sensor have been used for the purpose of running numerical simulations in MATLAB. The material of the bar has been assumed to be 316 L stainless steel, which is the material that was used for the solid bar described in Chapter 3. The properties that were substituted in (6.18) are listed below:

- h=28 µm
- g_{31}=216 × 10^{-3} $\dfrac{\text{V/m}}{\text{N/m}^2}$
- E_b=193 GPa
- E_s=3 GPa
- ρ_b=8000 kg/m^3

Using the material properties of the bar and (6.9), one obtains $c = 4911.72$ m/s.

6.2.1 Variation of sensor length

Let $\sigma_b = -100$ MPa (the value is negative because the stress is compressive in nature). FFTs from drop tests conducted on the steel bar earlier show that most of

101

the generated signal's power is contained in the low frequency range up to 2000 Hz. Hence, let us assume that the applied stress wave has a frequency $f = 2000$ Hz. This corresponds to an angular frequency value $\omega = 12566.37$ rad/s. Thus, the wavelength λ of the applied stress wave is $\lambda = c/f = 2.46$ m. Let $d = 5$ m as this will allow us to increase the length of the sensor up to 10 m.

Selection of the time instant

The time instant is to be selected such that the following conditions are followed:

(i) The applied sinusoidal stress wave reaches the middle of the sensor and is at its peak amplitude. This makes the sine term in (6.3) equal to unity.

(ii) The entire length of the sensor must be subjected to stress at this time instant.

Condition (ii) implies that even when the sensor length is increased up to 10 m, the stress wave must still cover the entire length of the sensor. The time taken by the stress wave to reach the middle of the sensor is given by d/c. In this section, the sensor length will be varied up to 10 m. Thus, the maximum distance between the middle of the sensor and the bottom of the sensor will be 5 m for the simulations. The period of the sinusoidal wave is given by $T = 1/2000$ s $= 0.5$ ms. Based on a trial and error approach, it was found that at $t = \dfrac{9}{4}T$, the sinusoidal wave will be at its peak magnitude of compressive stress and will have covered a distance of 5 m. Adding d/c to this will ensure that the stress wave at the middle of the sensor reaches its peak magnitude and the entire length of the sensor is subjected to stress. This time instant can be calculated as follows

$$t = \frac{9}{4}T + \frac{d}{c} = 2.14298 \text{ ms.} \tag{6.20}$$

At $t = 2.14298$ ms, the stress wave will have covered a distance of 10.526 m. Thus, at $t = 2.14298$ ms, even the maximum sensor length that has been considered (10 m) will be completely subjected to stress. Thus, at $t = 2.14298$ ms, both conditions (i) and (ii) are satisfied. Substituting all the above values in (6.18) and varying the parameter L (length of the sensor), one obtains the plot shown in Figure 6.2. The vertical lines in the plot help to compare the sensor length with the wavelength of the applied stress wave.
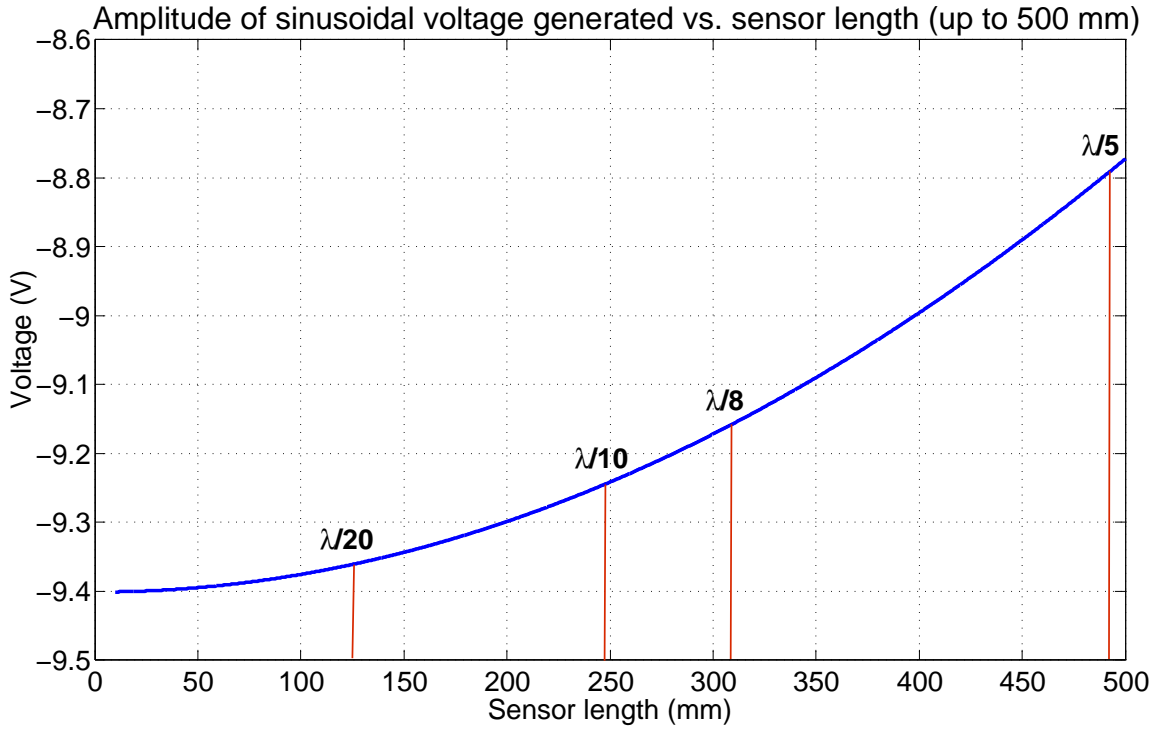
Figure 6.2: Amplitude of the voltage generated by the sensor as its length varies from 10 mm to 500 mm.

From Figure 6.2, one can see that the amplitude of the voltage generated by the sensor remains almost constant as the length of the sensor varies from 10 mm to 500 mm. This can be attributed to the fact that the wavelength of the applied stress wave is 2.46 m. Thus, the wavelength is quite large compared to the range of sensor length values that were shown in Figure 6.2. To see how the sensor averages the stress, one can look at the variation of generated voltage as its length is increased to five times its wavelength. This is shown in Figure 6.3.
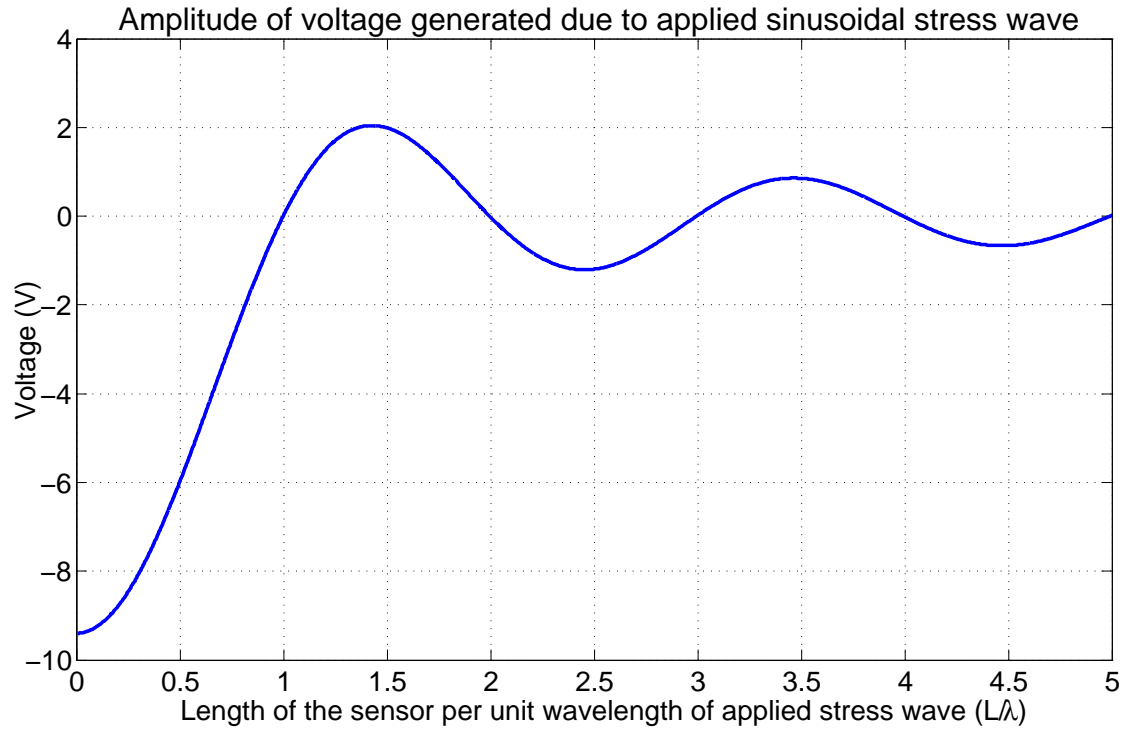

Figure 6.3: Amplitude of the voltage generated by the sensor as the sensor length is increased to 5 times the wavelength.

As expected, Figure 6.3 shows that the output of the sensor drops to 0 V when the length of the sensor is the same as the wavelength of the stress wave (or equal to a multiple of the wavelength). This is because the positive and negative parts of the wave cancel each other out. One can see that when the length of the sensor is substantially smaller than the wavelength of the stress wave, the sensor's averaging effect can be neglected since the generated voltage reaches a constant value which is very close to the value one would obtain in the case of an ideal sensor.

6.2.2 Variation of frequency of the applied stress wave

Rewriting (6.18) by substituting angular frequency with frequency, one obtains

$$V_{31} = \left(\frac{\sigma_b E_s g_{31} hc}{L E_b \pi f} \right) \sin \left(\frac{\pi f L}{c} \right) \sin 2\pi f \left(t - \frac{d}{c} \right), \tag{6.21}$$

where f = frequency of the applied stress wave in Hz.

In this section, the frequency of the applied stress wave is varied. The values of the rest of the parameters in (6.21) have been kept constant. The time instant at which the applied sinusoidal stress wave reaches the middle of the sensor and is at its peak magnitude is

$$t = \frac{13}{4}T + \frac{d}{c}. \tag{6.22}$$

The above value of t at the highest frequency turns out to be 1.02448 ms. At $t =$ 1.02448 ms, the stress wave will have covered a distance of 5.032 m. Thus, at $t =$ 1.02448 ms, even the maximum sensor length that has been considered (50 mm) will be completely subjected to stress. For each frequency, the value of time described by (6.22) is calculated and substituted in (6.21) to plot the graph shown in Figure 6.4. From Figure 6.4, one can see that the voltage generated by the sensor initially reduces in magnitude as the frequency of the applied stress wave increases. Eventually, as

105

the frequency of the stress wave is increased further, the amplitude of the voltage generated oscillates about 0 V and its magnitude keeps decreasing. It can be seen that only very high frequencies (>50 kHz for the 10 mm long sensor) cause a significant amount of reduction in the magnitude of the PVDF sensor's voltage.

Figure 6.4: Amplitude of the voltage generated by the sensor as the frequency of the applied stress wave is varied (up to 500 kHz) for different sensor lengths.

These frequencies are beyond the range that is usually encountered in structural applications. For other applications, sensor length must be reduced in order to preserve high frequencies. However, this will lead to a reduction of the sensor area, causing a reduction of the charge generated. This will degrade the signal-to-noise ratio (SNR). This problem can be circumvented by increasing the width of the sensor

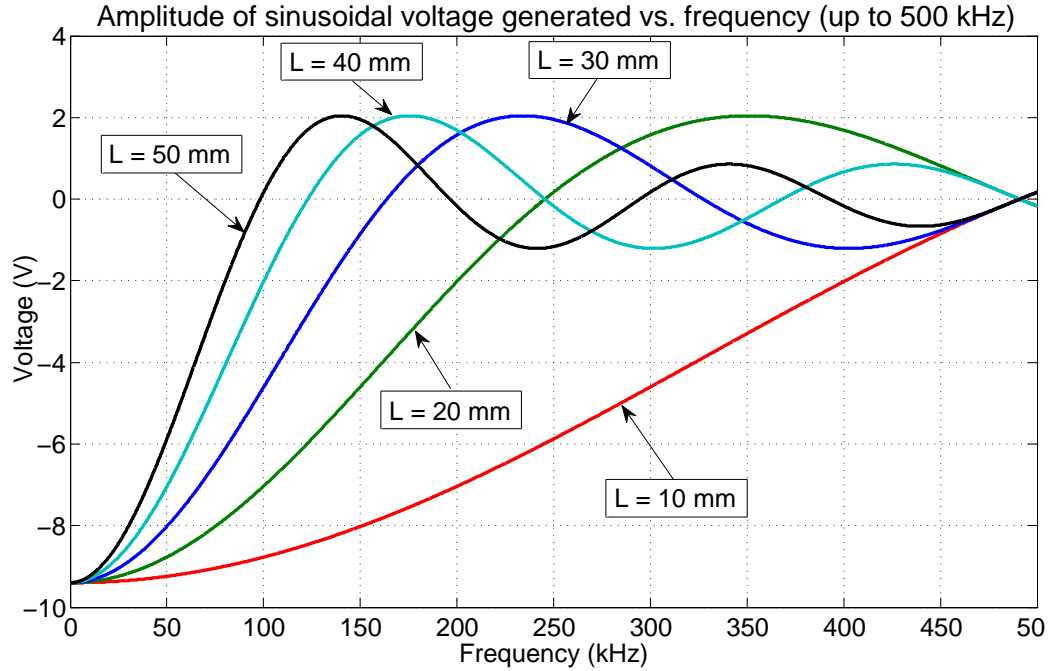and reducing its length, thus maintaining the same sensor area, or through patterning of the film and electrodes.
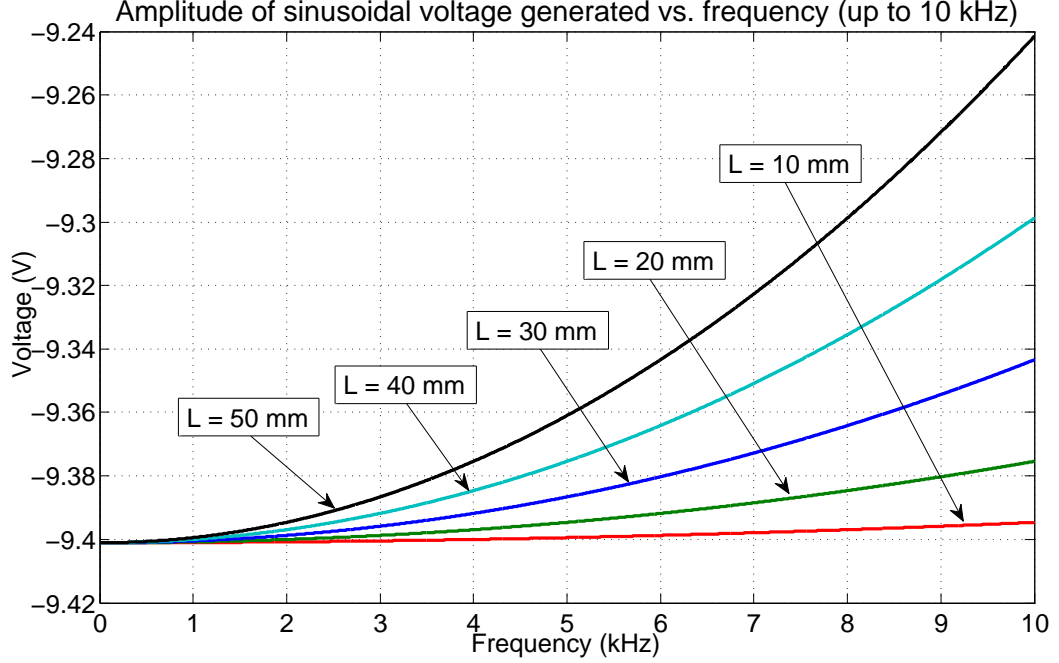
Figure 6.5: Amplitude of the voltage generated by the sensor as the frequency of the applied stress wave is increased up to 10 kHz.

Figure 6.5 shows the same plot as above, but for frequencies up to 10 kHz. Figure 6.5 shows that for frequencies up to 10 kHz, the reduction of the magnitude of generated voltage is very low.

Figure 6.6 shows variation of voltage generated by the sensor as the wavenumber is increased. The wavenumber denotes the spatial frequency of a wave and is defined as the reciprocal of the wavelength. It can also be defined as the ratio of the frequency of the applied stress wave to the speed of sound in the bar. From the figure, one can see that for each sensor length shown, the magnitude of voltage reaches zero for the value
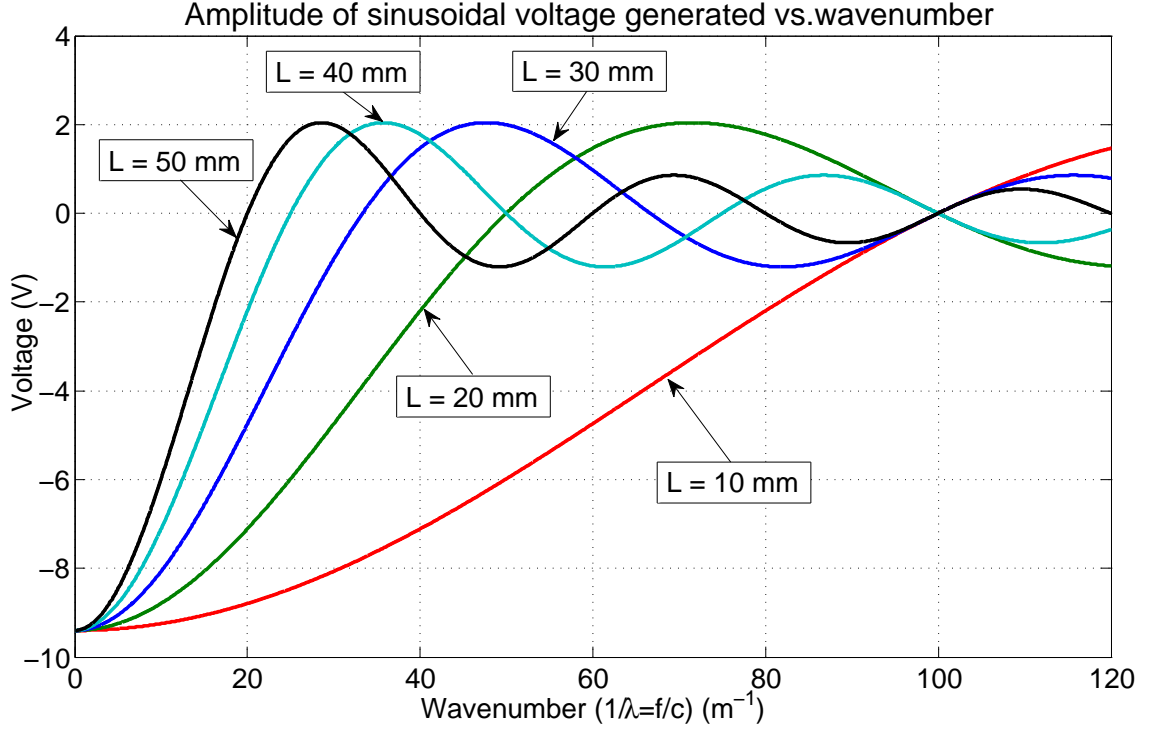
Figure 6.6: Amplitude of the voltage generated by the sensor as the wavenumber of the applied stress wave is varied.

of wavenumber at which the sensor length corresponds to one complete wave and for integral multiples of this value. Thus, Figure 6.6 conveys the same information as Figure 6.4, but makes it easier to understand the dependence of the sensor's stress averaging effect on the number of stress wave cycles acting on the sensor.

From (6.15), the ideal voltage, neglecting the sensor's stress averaging effect, can be written as

$$V_{ideal} = \frac{g_{31} h E_s \sigma_b}{E_b} \sin 2\pi f \left(t - \frac{d}{c} \right). \tag{6.23}$$

108

The difference or error e between the ideal voltage generated and the voltage generated under the effect of sensor averaging can be written as

$$e = V_{ideal} - V_{31}. \tag{6.24}$$

Thus, using (6.18), (6.23), and (6.24), one can write

$$e(t) = \frac{g_{31}hE_s\sigma_b}{E_b}\left(1 - \frac{c}{L\pi f}\sin\frac{L\pi f}{2c}\right)\sin 2\pi f\left(t - \frac{d}{c}\right). \tag{6.25}$$

$$\text{Percentage difference} = \frac{e(t)}{V_{ideal}} \times 100 = \left(1 - \frac{c}{L\pi f}\sin\frac{L\pi f}{2c}\right) \times 100. \tag{6.26}$$

Figure 6.7: Percentage difference in amplitude of voltage generated against frequency of the applied stress wave, for different sensor lengths.

A plot of the percentage difference in voltage generated against frequency of the applied stress wave, for different sensor lengths, has been shown in Figure 6.7. It shows that the percentage difference between the ideal voltage generated and the actual voltage generated is very low for frequencies up to 10 kHz.
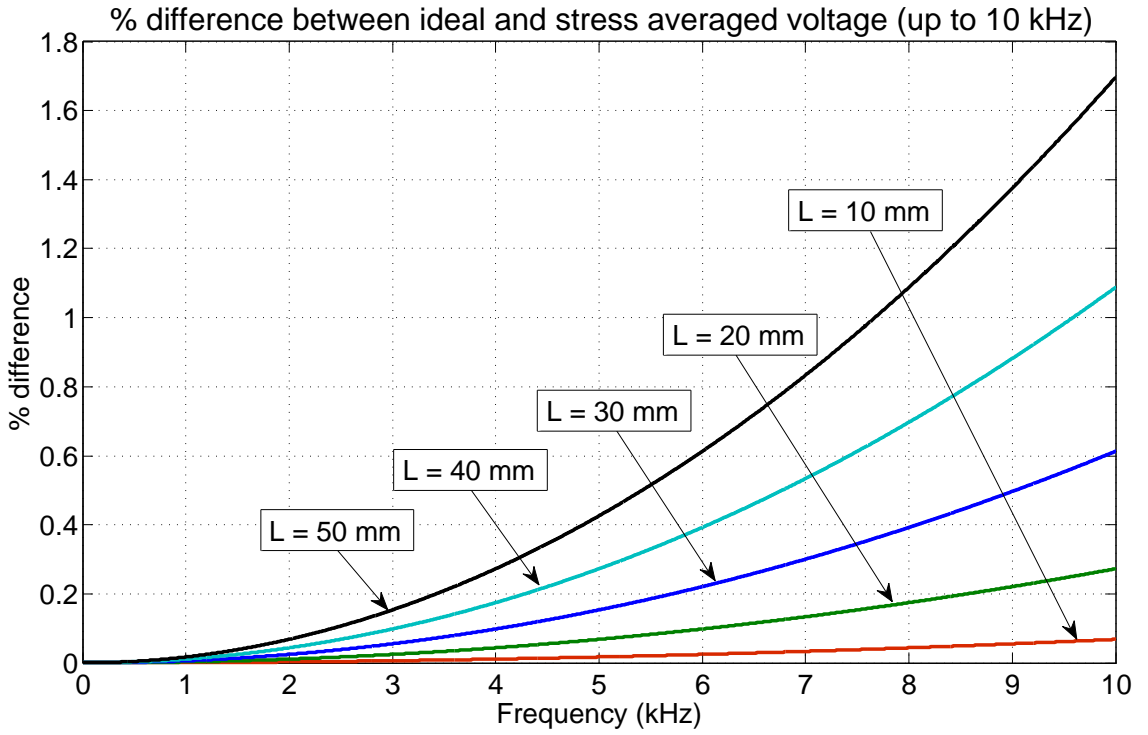
The variation of the voltage generated also indicates that the proportionality constant k, defined in Chapter 3 and Chapter 4 as a ratio of the voltage generated to the force applied to the bar, is frequency dependent. However, the power spectrum of the impact signals recorded in the experiments discussed in those chapters shows that most of the power is contained in the frequency range under 1 kHz. Figure 6.7 shows that when the applied frequency is less than 1 kHz, the reduction in magnitude of voltage is negligible. Hence, it can be concluded that k, defined for the solid bar and hollow beam impact experiments, is independent of the applied frequency.

6.3 PVDF sensor's response to impact-induced stress waves

This section discusses the effect of the PVDF sensor's stress averaging effect when the fixed bar described in Section 6.1, with the PVDF sensor attached, is impacted at the top by a moving block. All the assumptions that were listed in Section 6.1 are applicable in this section too. In addition, it is also assumed that the impacting block is absolutely rigid.

Let M be the mass of the block per unit area of the cross section of the bar. Let the initial velocity of the block at the instant of impact be v_0. Assuming $v(t)$ is the velocity of the block and $\sigma_b(t)$ is the compressive stress at the top of the bar, the following equation can be derived by balancing forces acting on the free end of the

bar [19]:

$$M\frac{\mathrm{d}v}{\mathrm{d}t} + \sigma_b = 0. \tag{6.27}$$

Substituting $v = \sigma_b/\sqrt{E_b\rho_b}$ in (6.27), one obtains

$$\frac{M}{\sqrt{E_b\rho_b}}\frac{\mathrm{d}\sigma_b}{\mathrm{d}t} + \sigma_b = 0, \tag{6.28}$$

which is a differential equation whose solution an be written as

$$\sigma_b(t) = \sigma_0 e^{-\frac{t\sqrt{E_b\rho_b}}{M}}. \tag{6.29}$$

Here, σ_0 is the compressive stress at the front of the wave, where $\sigma_0 = v_0\sqrt{E_b\rho_b}$.

Substituting (6.29) in (6.13), one obtains

$$
\begin{aligned}
\sigma_{savg}(t) &= \frac{E_s}{LE_b}\int_{d-L/2}^{d+L/2}\sigma_0 e^{-\left[\left(t-x\sqrt{\frac{\rho_b}{E_b}}\right)\frac{\sqrt{E_b\rho_b}}{M}\right]}\mathrm{d}x \\
&= \frac{E_s\sigma_0 e^{-\frac{t\sqrt{E_b\rho_b}}{M}}}{LE_b}\int_{d-L/2}^{d+L/2} e^{\frac{x\rho_b}{M}}\mathrm{d}x,
\end{aligned} \tag{6.30}
$$

which upon integration, gives

$$\sigma_{savg}(t) = \frac{E_s\sigma_0 M e^{\left(\frac{\rho_b d - t\sqrt{E_b\rho_b}}{M}\right)}}{LE_b\rho_b}\left(e^{\frac{L\rho_b}{2M}} - e^{-\frac{L\rho_b}{2M}}\right). \tag{6.31}$$

Using (6.15) and (6.31), one can write

$$V_{31}(t) = \frac{E_s\sigma_0 M g_{31} h e^{\left(\frac{\rho_b d - t\sqrt{E_b\rho_b}}{M}\right)}}{LE_b\rho_b}\left(e^{\frac{L\rho_b}{2M}} - e^{-\frac{L\rho_b}{2M}}\right). \tag{6.32}$$

Substituting $\sigma_0 = v_0\sqrt{E_b\rho_b}$ in (6.32) and rearranging the terms, one obtains

$$V_{31}(t) = \left[\frac{E_s v_0 M g_{31} h}{L\sqrt{E_b\rho_b}}\left(e^{\frac{L\rho_b}{2M}} - e^{-\frac{L\rho_b}{2M}}\right)\right]e^{\left(\frac{\rho_b d - t\sqrt{E_b\rho_b}}{M}\right)}. \tag{6.33}$$

The voltage generated by the PVDF sensor when a block of mass M impacts the bar at a velocity v_0 is given by (6.33), taking into account the sensor's stress averaging effect.

111

6.4 Numerical simulations for impact-induced stress wave input

Similar to Section 6.2, the properties of the LDT1-028K PVDF sensor have been used for the purpose of running numerical simulations in MATLAB and the material of the bar has been assumed to be 316 L stainless steel.

Let the peak impact stress $\sigma_0 = 100$ MPa.

Let $M = 73867$ kg/m^2 (based on the cross-sectional area of the bar and the mass of the impactor).

To ensure that the stress wave travels from the free end of the bar to the farther end of the sensor, thus subjecting the entire sensor to stress, let

$$t = \frac{\left(d + \frac{L}{2}\right)}{c}. \tag{6.34}$$

Selecting this time instant gives the maximum output voltage generated by the sensor at that particular value of sensor length. The value of d was set to 5 m for all the simulations, as this allows us to increase the length of the sensor up to 10 m.

6.4.1 Applied impact-induced stress

Figure 6.8 shows the variation of compressive stress along the bar after axial impact on the free end, using the values of M and σ_0 mentioned above. The sensor length is set to 500 mm. Impact occurs at time $t = 0$. The blue curve shows the position of the stress wave at the time instant given by (6.34). Figure 6.9 shows the variation of the compressive stress acting on the free end of the bar after it gets impacted by the block at $t = 0$.
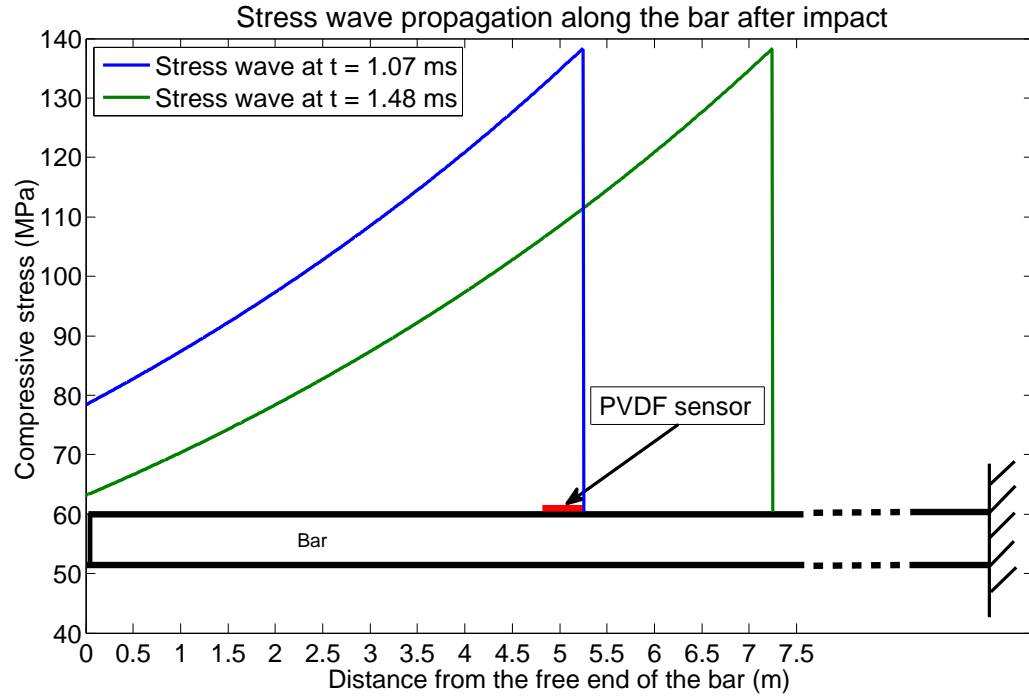
Figure 6.8: Variation of compressive stress along the bar after impact at the free end.
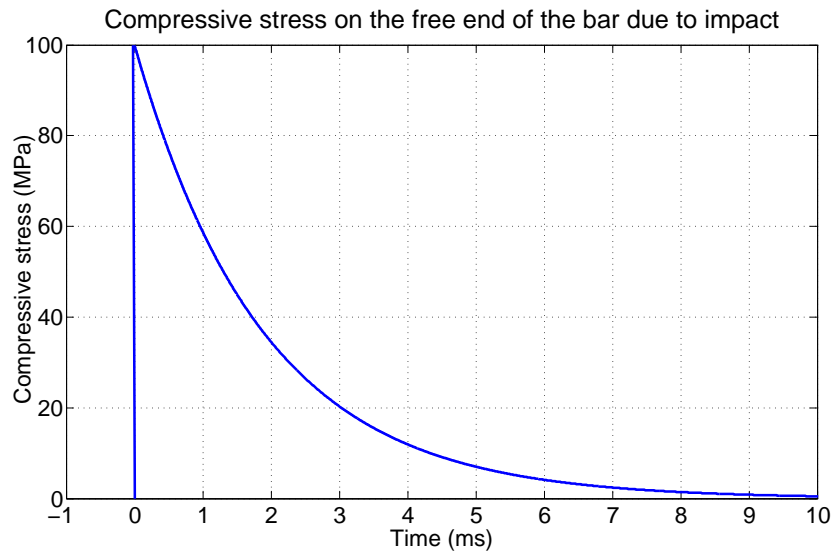
Figure 6.9: Compressive stress acting on the free end of the bar due to impact.

113

6.4.2   Variation of sensor length
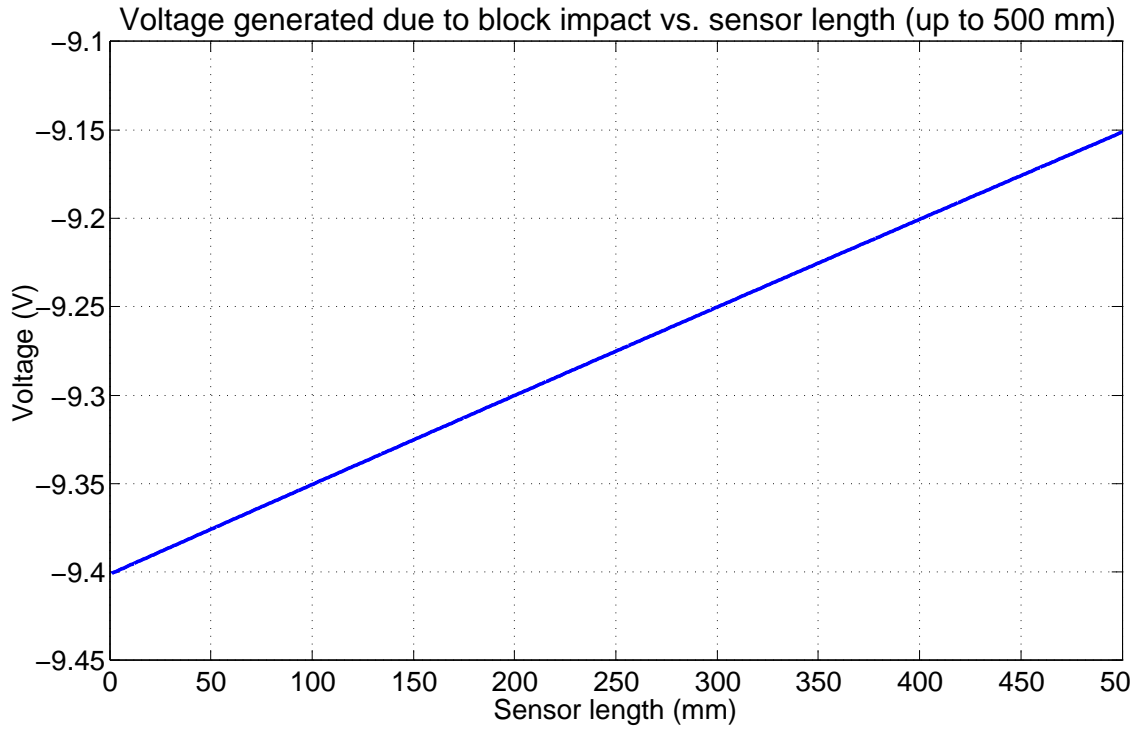
Figure 6.10: Voltage generated by the sensor as its length varies from 1 mm to 500 mm.

Figure 6.10 shows that the voltage generated by the sensor remains almost constant as the length of the sensor varies from 10 mm to 50 mm. To see the effect of reduced voltage due to averaging of stress, the length of the sensor has to be increased up to 10 m. This has been shown in Figure 6.11. From Figure 6.11, it is clear that there is a significant reduction in the voltage generated by the PVDF sensor after impact as the length of the sensor is increased from 1 mm to 10 m.
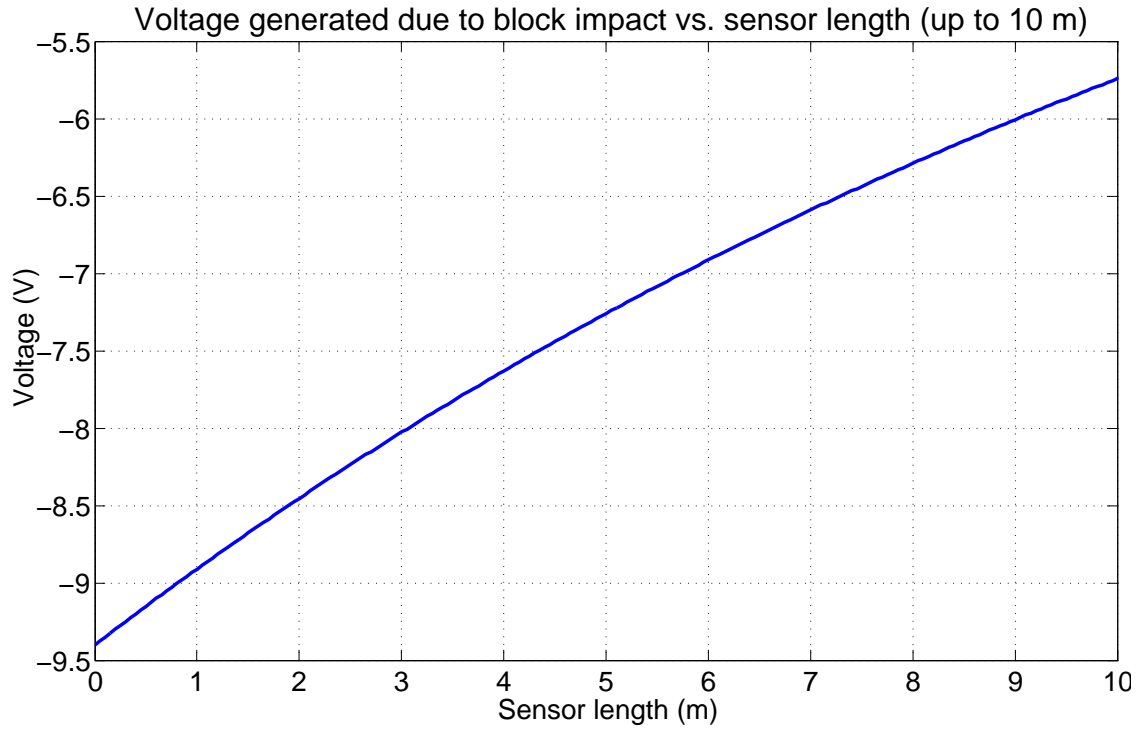
Figure 6.11: Voltage generated by the sensor as its length varies from 1 mm to 10 m.

Figure 6.12 shows the time histories of the voltages generated by sensors of different lengths. For each of the curves, time $t = 0$ corresponds to the time instant when the stress front reaches the bottom of the sensor. It can be seen that there is no significant difference between the time histories of the voltages for sensor length 0.03 m and 1 m.
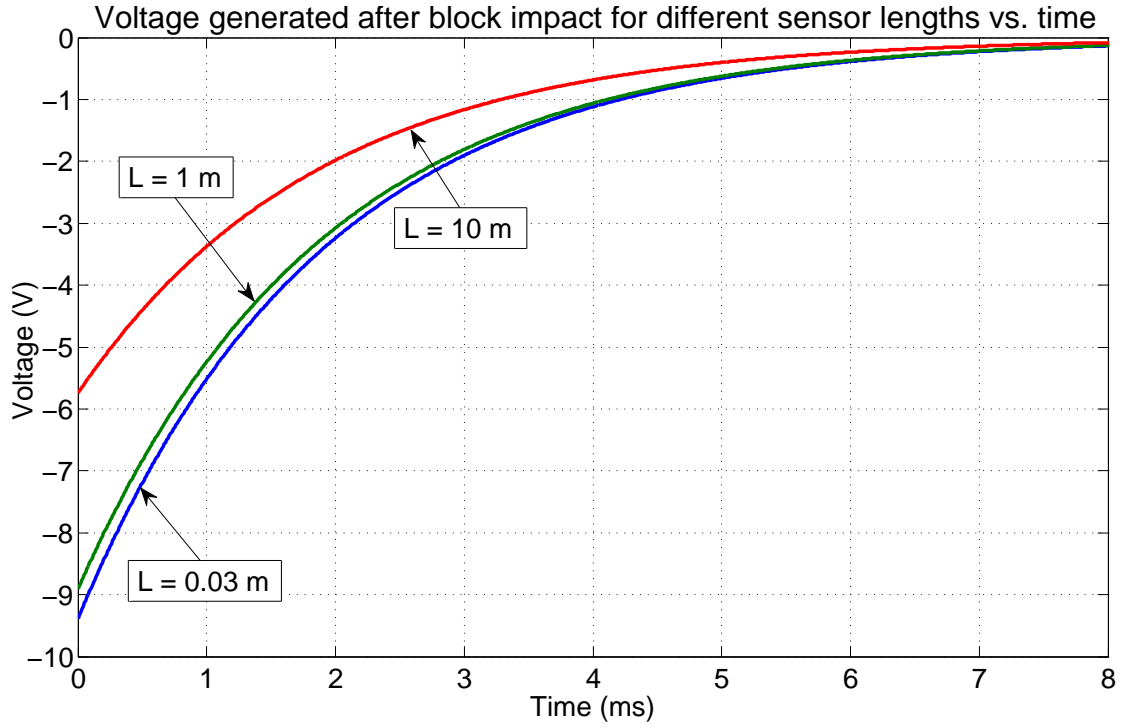
Figure 6.12: Time histories of voltage generated after block impact for sensors of different lengths.

6.4.3 Effect of changing the material of the bar

Changing the material of the bar leads to a change in the amount of strain developed in the bar due to impact. Thus, changing the material of the bar causes the voltage generated by the PVDF sensor to change, since the voltage generated by the sensor depends on the amount of strain acting on the bar. Hence, in order to observe the dependence of the sensor's stress averaging effect on the material of the bar, it is necessary to plot the percentage error or difference caused due to the sensor's stress averaging effect when different materials are used for the bar.

Let us consider the voltage generated by the sensor at time t defined by (6.34). Figure 6.8 shows the profile of the stress wave along the length of the bar. The ideal

sensor would be so infinitesimally small that the stress acting on it at time t would be σ_0. Thus, using (6.15), one can write the voltage generated by the ideal sensor at time t, namely, V_{ideal} as

$$V_{ideal}(t) = \frac{E_s g_{31} h}{E_b} \sigma_0. \tag{6.35}$$

Using (6.24), (6.32), and (6.35), the difference or error e between the ideal voltage generated and the voltage generated under the effect of sensor averaging for impact-induced stress can be written as

$$e(t) = \frac{E_s g_{31} h \sigma_0}{E_b} \left[1 - \frac{M}{L\rho_b} \left(1 - e^{-\frac{L\rho_b}{M}} \right) \right]. \tag{6.36}$$

$$\text{Percentage difference} = \frac{e(t)}{V_{ideal}} \times 100 = \left[1 - \frac{M}{L\rho_b} \left(1 - e^{-\frac{L\rho_b}{M}} \right) \right] \times 100. \tag{6.37}$$

From (6.37), one can see that the percentage difference depends upon the density of the bar's material, but is independent of its Young's modulus. Using 6.37, the percentage difference between the ideal voltage generated and the voltage generated under the effect of sensor averaging was plotted for four different materials as shown in Figure 6.13. From Figure 6.13 and Table 6.2, it can be concluded that the density of the material of the structure has a significant influence on the sensor's stress averaging effect. It can be seen that the material with the lowest density (polystyrene) shows the least amount of deviation from the ideal voltage, as the sensor length is increased, and the material with the highest density (copper) shows the maximum amount of deviation from the ideal voltage, as the sensor length is increased.
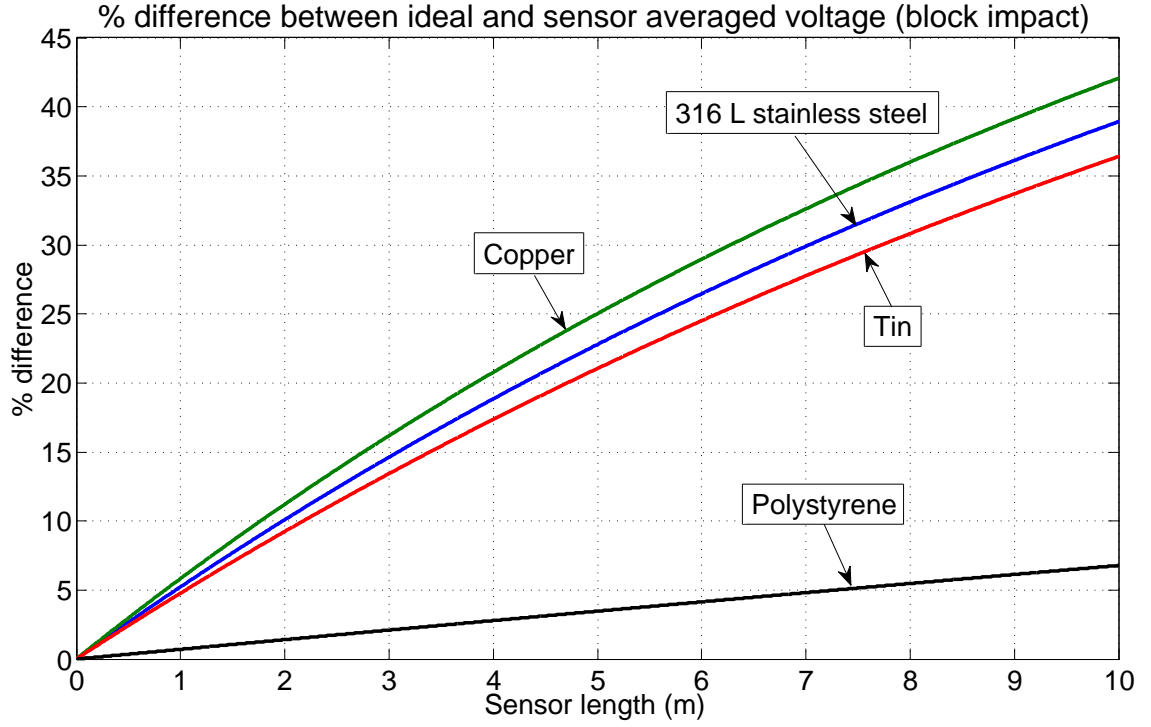
Figure 6.13: The % difference between the ideal voltage and the voltage generated under the effect of sensor averaging, as sensor length is varied, for four materials.

Table 6.2 shows a comparison of the material properties of 316 L stainless steel, copper, tin, and polystyrene, which were used in Figure 6.13.

Material used for the bar	E_b (GPa)	ρ_b (kg/m^3)	c (m/s)
316 L stainless steel	193	8000	4912
Copper	120	8960	3660
Tin	50	7280	2621
Polystyrene	2.28	1050	1474

Table 6.2: Comparison of the properties of the four materials used for the bar.

6.5 Conclusions

The equations modeling the PVDF sensor's stress averaging effect were derived in this chapter for periodic applied stress waves and impact-induced applied stress waves. Based on these equations and the numerical simulations, the following points emerge:

- In the case of periodic applied stress waves, it is shown that the voltage generated by the sensor is influenced by sensor length, the frequency of the applied stress wave, and the material properties of the structure (Young's modulus and density) because of the sensor's stress averaging effect.
- Based on the results of the numerical simulations it is concluded that very high frequencies, cause a significant reduction of the sensor's voltage, assuming typical values for sensor length. These frequencies are much higher than those typical encountered in structural sensing applications. Hence, for these applications, one can assume that the stress averaging effect depends only on the length of the sensor.
- If the preservation of high frequencies is important, the sensor length must be reduced, while ensuring that the S/N ratio does not degrade significantly. This can be achieved by adjusting the width of the sensor to keep the sensor area constant, or through patterning of the film and electrodes.
- From the numerical simulations for both periodic stress waves and impact-induced stress waves, one can conclude that for most practical values of sensor lengths, the effect of stress averaging on the voltage generated by the sensor

is negligible, assuming the structure has material properties similar to 316 L stainless steel.

- In the case of impact-induced stress waves, it is concluded that the density of the structure's material has a significant influence on the sensor's stress averaging effect. The higher the density of the structure, the more pronounced is the stress averaging effect. In addition, the stress averaging effect also depends upon the mass of the impacting block per unit cross-sectional area of the bar and the length of the sensor.

Chapter 7: CONCLUSION

This thesis has explored various aspects related to the sensing of transient stress waves in a structure using PVDF sensors.

7.1 Summary

Chapter 2 showed that simple interfacing circuits can be used to determine the voltage generated by PVDF sensors if appropriated transfer functions (or measurement functions) are derived and applied to the measured signals. These interfacing circuits may be required to reduce the voltage to a suitable range for the DAQ system and to isolate the sensors from the DAQ system, both as a safety mechanism to prevent damage to the DAQ due to high voltages as well as to provide a single, known measurement function regardless of the input impedance of the DAQ.

Chapter 3 discussed the impact experiments performed on a solid stainless steel bar. The average voltage generated by the PVDF sensors was observed to be proportional to the impact force, for each of the three drop tests. The proportionality constants, relating the PVDF output voltage and the impact force for the three drop tests, were closely spaced. Hence, it can be concluded that using the average voltage generated by the PVDF sensors and the average proportionality constant, the impact force history can be determined. The results presented in this chapter also validate

the experimental method developed for performing impact tests using PVDF sensors bonded to structures. A close match was observed between the LS-DYNA simulation and the experimental results, thereby validating the LS-DYNA model created for the impact tests on the solid bar.

Chapter 4 presented the results of impact tests on hollow steel beams, using the experimental method detailed in Chapter 3. Even though the hollow beams had a complex geometry, a single proportionality constant between the PVDF output voltage and the impact force calculated from the non-destructive impact tests (22-40 kN peak forces) was found to apply to high-energy destructive tests (peak forces $\approx$ 99 kN) as well. Thus, the experimental method presented in Chapter 3 and Chapter 4 demonstrates that PVDF sensors can be used to determine the impact force acting on a structure.

Chapter 5 showed that the speed of sound for longitudinal waves in a slender rod can be measured accurately using two PVDF sensors. It was shown that PVDF sensors respond very fast to the stress waves propagating through the structure, accurately measuring wave transit times on the order of a few microseconds. This implies that PVDF sensors can be used to detect the propagation of stress waves, traveling at a high speed, between two points in a structure. In addition, the results shown in this chapter emphasize the high sensitivity of the PVDF sensors since they are able to detect the small magnitude stress waves caused by impact force as low as 10 N on a stainless steel rod. The advantages of using the PVDF sensors in 31 or 32 modes (or in-plane modes) as opposed to 33 mode (or out-of-plane mode) were also highlighted.

In Chapter 6, equations relating the PVDF sensor's stress averaging effect to the voltage generated were derived for periodic applied stress waves and impact-induced stress waves. For the case of periodic applied stress waves, it was shown that the PVDF sensor's length, the frequency of the applied stress wave, and the material properties of the structure (Young's modulus and density) influenced the voltage generated by the sensor, because of the sensor's stress averaging effect. It was concluded that for structural sensing applications, the stress averaging effect only depends upon sensor length. For a stainless steel structure, the reduction of voltage caused by stress averaging was shown to be negligible for most practical values of sensor lengths in the case of both periodic as well as impact-induced applied stress. In the case of impact-induced stress waves, it was concluded that the stress averaging effect depends on the density of the structure's material, the mass of the impacting block per unit cross-sectional area of the bar, and the length of the sensor.

Thus, the research presented in this thesis shows that PVDF sensors can be used for determining the magnitude of an impact force or applied stress on a structure as well as detecting or monitoring the propagation of the stress waves in the structure.

7.2 Future work

In the case of destructive impact tests, having an accurate simulation model can provide valuable information about the behavior of the specimen during impact. This information can be used to decide parameters like drop height, mass of the drop head, and location of the sensor on the specimen. Hence, it will be useful to develop an LS-DYNA model that includes the geometric imperfections of the hollow beams, so as to be able to accurately simulate the impact tests.

It was observed the impact between the flat plate attached to the load cell and both the solid bar and the hollow beam was not perfectly parallel. Because of this, the impact force acting on the structures was dissimilar to an impulse, which was predicted by the LS-DYNA simulation of a perfect impact. Hence, an impact experiment could be performed using a spherical impact head to apply an impact force which would be a closer approximation to an impulse input.

For the analytical work on sensor averaging in Chapter 6, the effect of reflections of stress waves could be added to the model.

Bibliography

[1] Measurement Specialties, Inc., 1000 Lucas Way Hampton, VA 23666. *Piezo Film Sensors Technical Manual*, April 1999.

[2] T. Obara, N. K. Bourne, and Y. Mebar. The construction and calibration of an inexpensive PVDF stress gauge for fast pressure measurements. *Measurement Science and Technology*, 6:345–348, April 1995.

[3] W.H. Zhu, T.X. Yu, and Z.Y. Li. Laser-induced shock waves in pmma confined foils. *International Journal of Impact Engineering*, 24(67):641–657, 2000.

[4] P.K. Dutta and J. Kalafut. Evaluation of pvdf piezopolymer for use as a shock gauge. Technical report, DTIC Document, 1990.

[5] Y. Mori, K. Hidaka, and K. Nagayama. Simultaneous measurement method of both shock state and stress profile in polymers in 1 GPa stress. *Review of Scientific Instruments*, 71(6):2492–2496, 2000.

[6] L. Gaul and S. Hurlebaus. Determination of the impact force on a plate by piezoelectric film sensors. *Archive of Applied Mechanics*, 69(9):691–701, 1999.

[7] S.J. Kuhr and J.L. Blackshire. Quantification of impact damage in cmc thermal protection systems using thin-film piezoelectric sensors. In *The 14th International Symposium on: Smart Structures and Materials & Nondestructive Evaluation and Health Monitoring*, pages 65300Q–65300Q. International Society for Optics and Photonics, 2007.

[8] F. Bauer. Ferroelectric pvdf polymer for high pressure and shock compression sensors. In *Electrets, 2002. ISE 11. Proceedings. 11th International Symposium on*, pages 219–222. IEEE, 2002.

[9] F. Bauer. United States patent: 4611260 - Method and device for polarizing ferroelectric materials, September 1986.

[10] C. Ren, W. Dong, and F. Bai. Design and fabrication of piezoelectric sensor based on pvdf film for human pulse measurement. In *The 10th International Symposium of Measurement Technology and Intelligent Instruments*, volume X. International Journal of Precision Engineering and Manufacturing, June 2011.

[11] R.L. Chen and B.T. Wang. The use of polyvinylidene fluoride films as sensors for the experimental modal analysis of structures. *Smart Materials and Structures*, 13(4):791, 2004.

[12] S. Anuphap-udom, K. Ratanathammapan, and Kaewkongka T. Fabricated pvdf acoustic emission sensor for lubricated bearing monitoring. *J. Sci. Res. Chula. Univ*, 31(2):115–119, October 2006.

[13] G. Monté Muñoz. Design and development of an electronic interface circuit for piezoelectric sensors applied to impact detection. Master's thesis, Universitat Polytècnica de Catalunya, May 2011.

[14] Measurement Specialties, Inc., 1000 Lucas Way Hampton, VA 23666. *LDT1-028K Piezo Sensor w/ Lead Attachment*, May 2009.

[15] D. Shen. *Piezoelectric energy harvesting devices for low frequency vibration applications.* PhD thesis, Auburn University, 2009.

[16] J. Sirohi and I. Chopra. Fundamental understanding of piezoelectric strain sensors. *Journal of Intelligent Material Systems and Structures*, 11(4):246–257, 2000.

[17] Livermore Software Technology Corporation (LSTC), 7374 Las Positas Road, Livermore, CA 94551 (925) 449-2500. *LS-DYNA Keyword User's Manual Volume I*, 971 edition, May 2007.

[18] Damping - LS-DYNA support (n.d.). retrieved december 8, 2012, from http://www.dynasupport.com/howtos/general/damping.

[19] S. P. Timoshenko and J. N. Goodier. *Theory of Elasticity*, volume 1 of *Engineering societies monographs.* McGraw-Hill, New York, 3 rd edition, 1970.

[20] J. F. A. M. van Hoof. *One- and Two-Dimensional Wave Propagation in Solids.* WFW-report 94-055, Eindhoven University of Technology, The Netherlands, May 1994.